IMPROVEMENT OF CALORIMETER-BASED MUON IDENTIFICATION AND ITS APPLICATION TO $H \rightarrow ZZ^{(*)} \rightarrow 4\ell$ ANALYSIS IN THE ATLAS EXPERIMENT

by

Neslihan BECERİCİ SCHMIDT

B.S. in Physics, Yıldız Technical University, 2004

Submitted to the Institute for Graduate Studies in
Science and Engineering in partial fulfillment of
the requirements for the degree of
Master of Science

Graduate Program in Physics

Boğaziçi University

2009

IMPROVEMENT OF CALORIMETER-BASED MUON IDENTIFICATION AND ITS APPLICATION TO $H \rightarrow ZZ^{(*)} \rightarrow 4\ell$ ANALYSIS IN THE ATLAS EXPERIMENT

APPROVED BY:

Prof. Metin ARIK (Thesis Supervisor)	.....
Assoc. Prof. Serkant Ali ÇETİN (Thesis Co-supervisor)	.....
Assoc. Prof. Muhittin MUNGAN	.....
Assist. Prof. Tonguç RADOR	.....
Prof. Saleh SULTANSOY	.....

DATE OF APPROVAL: 23.01.2009

ACKNOWLEDGEMENTS

First of all, I would like to express my gratitude to Prof. Aleandro Nisati for having encouraged and supported me at a very difficult time in my life. I am also thankful to him for having introduced me to Prof. Sau Lan Wu and Luis Roberto Flores Castillo, to whom I owe a lot for giving this thesis project to me and providing help of every kind, at every step. I will always appreciate Prof. Sau Lan Wu for trusting me and accepting me to work with her group, where I met with lots of nice people, enjoyed their friendship and found the chance to learn a lot from them.

I am short of words to thank enough to Luis. While "super"vising me throughout my work at CERN, he always created time to teach and guide me and motivated me with his kind words. I also admire him for he never gave up counting me in at soccer games, although I am the worst soccer player. I could have never been able to prepare this thesis without him.

I am also very thankful
to Gustavo Ordonez for helping me with his fast responses when I had questions,
to Ruslan Asfandiyarov and Alfredo Castaneda who were very very nice office-mates,
to Prof. Saleh Sultansoy for his interest in my work,
to Prof. Metin Arık, Serkant Ali Çetin and Johanna Bronner for their support and invaluable comments that improved the content of this thesis
and to Maximilian Schmidt for his delicious tee services when I work, and for all the nice things he brings into my life.

All my life I will be grateful to Nesrin Becerici, who let me to develop by finding my own ideas and self, also when it was different than the majority and their expectations.

I dedicate this thesis to my dear supervisor Prof. Engin Arık and my dear friends Engin Abat and Özgen Berkol Doğan, with whom I started to work together in this field, but lost all of a sudden. They left behind lots of important scientific works done, lots of works unfinished, and lots of people who love them and will always miss them. Besides, Prof. Engin Arık left behind a country, that finally gives importance to High Energy Particle Physics and provides opportunities to scientists to work on this field, owing to her dedication on this way. Although it was big fun and honour to meet and work together with very friendly and valuable scientists during the time I prepared this thesis, it was difficult to continue without the pleasure of learning from them and being together with them.

ABSTRACT

IMPROVEMENT OF CALORIMETER-BASED MUON IDENTIFICATION AND ITS APPLICATION TO $H \rightarrow ZZ^{(*)} \rightarrow 4\ell$ ANALYSIS IN THE ATLAS EXPERIMENT

Outermost part of the ATLAS detector, the muon spectrometer, is dedicated for detection of muons and measurement of their properties. However, combining the measurements from other parts of the detector with muon spectrometer measurements improves the performance of reconstruction and identification of muons. A complementary method to these strategies is the identification of muons in the calorimeter, without using the muon spectrometer measurements. Energy deposition of muons in the calorimeter has distinct characteristics, which enables their identification by using the energy loss measurements. This method is especially useful for identification of the muons that are failed to be reconstructed due to their insufficiently low momenta to traverse the full muon spectrometer or even to reach it, or due to traversing low-acceptance regions of the muon spectrometer.

One of the calorimeter-based muon identification algorithms has been improved within this thesis work. The performance of the improved algorithm and the results of its application to $H \rightarrow ZZ^{(*)} \rightarrow 4\ell$ analysis are presented. Also, possible extensions for further improvements are discussed.

ÖZET

ATLAS DENEYİNDE KALORİMETRE TEMELLİ MÜON TEŞHİSİNİN GELİŞTİRİLMESİ VE $H \rightarrow ZZ^{(*)} \rightarrow 4\ell$ ANALİZİNE UYGULANMASI

ATLAS dedektörünün en dış katmanı olan müon spektrometresi müonların dedekte edilmesi ve özelliklerinin ölçülmesi için tasarlanmıştır. Dedektörün diğer kısımlarındaki ölçümlerin müon spektrometresinden elde edilen ölçümler ile birleştirilmesi müon ölçüm ve teşhis performansını arttırmaktadır. Bu stratejilere tamamlayıcı bir etkide bulunan başka bir yöntem de, müonların spektometredeki ölçümleri kullanılmaksızın kalorimetrede teşhis edilmesidir. Müonların kalorimetrede bıraktıkları enerjinin ayırtedilebilir karakteristiği, enerji kaybı ölçümlerinin müonları teşhis etmede kullanılmasını sağlar. Bu yöntemin özellikle kullanışlı olduğu durumlar, düşük momentumlarından dolayı müon spektrometresinin içinden geçemeyen ya da ona ulaşamayan, veya müon spektrometresinin akseptansının düşük olduğu yerlerde bulunan teşhis edilememiş müonların teşhis edilmesidir.

Bu tez çalışması kapsamında kalorimetre temelli müon teşhisi algoritmalarından biri geliştirilmiştir. Algoritmanın yeni performansı ve $H \rightarrow ZZ^{(*)} \rightarrow 4\ell$ kanalının analizine uygulanmasının sonuçları gösterilmiştir. Ayrıca, daha da iyi bir performans sağlayacak muhtemel ilaveler tartışılmıştır.

TABLE OF CONTENTS

LIST OF FIGURES

LIST OF TABLES

1. INTRODUCTION

Everything that occupies a volume in space is dividable into smaller pieces and these pieces into still smaller pieces, so that, this division process can be kept going on with appropriate experimental setups until one finally reaches the smallest pieces that don't have a substucture, in other words; the pointlike particles. However, we can neither be certain of what we reached is a pointlike particle, nor can tell if it really exists, but when we observe that a particle thought to be fundamental actually consists of other paritcles, we can certainly be sure which one is more fundamental. Besides, we can construct our theories by assuming that they are pointlike particles. This assumption will not be misleading, since every theory has a range where it is valid and is always an approximation to a more general case. Particle physics is one of the branches of physics that explores these fundamental constituents of matter and mathematically formulates and explains the laws that govern their behaviours.

It was sometimes theoretical predictions that helped experimentalists to observe new paticles and sometimes an unexpected new particle or phenomena observed in the experiments inspired theorists, but finally in the second half of the 20th century, a successful mathematical description of the fundamental particles and their interactions, the Standard Model (SM) of particle physics, has developed. The SM is a gauge invariant quantum field theory that explains the three of the four fundamental interactions - the electromagnetic, the strong and the weak interaction - between the particles fundamental in the SM. However, gravitational interactions could not be explained in the same theoretical framework because a quantum field theory of gravity does not exist.

The fundamental particles in the SM were all discovered by the end of 20th century, except the predicted Higgs particle, which is responsible for the electroweak symmetry breaking of the SM, that allows for the massive gauge bosons and fermions. Although theoretical arguments and previous experiments set some limits on it, the mass of the Higgs particle is a free parameter in the SM which has to be measured

in the experiments that will manage to observe it. Masses and other properties of some of the particles are measured with a high precision and some are awaiting for the new high energy experiments for higher precision measurements. However, the most important goal for the new experiments is the discovery and measurements of the Higgs particle, since its observation will truely establish the success of the SM. Also, it is a stong motivation to experimentally test the predictions made by new theories beyond the SM.

There is a long list of physics goals waiting for the operation of the new potential discovery machine at CERN[1] : the Large Hadron Collider (LHC). It is a proton-proton accelerator and collider with a centre-of-mass energy of 14 TeV and a design luminosity of $10^{34}\text{cm}^{-2}\text{s}^{-1}$. The experiments of the LHC will surely provide answers to many questions, since the collision energy is sufficiently high for creation of expected interesting phenomena and the number of events will be excessive due to LHC's high luminosity, and probably it will also will bring about new questions by the observation of unexpected new phenomena, since the LHC will enter an unexplored domain of energy at TeV scale. To observe and measure the particles emanating at the interaction points, there are detectors located at four different points of the LHC, where the proton-proton collisions are going to take place. The ATLAS[2] detector covers one of these interaction points and is designed to explore a long list of physical phenomena, with the main goal being the discovery of the long sought-after Higgs particle.

There are several production processes for the Higgs particle at the LHC, where the theoretically calculated cross section of each process depends on its unknown mass. However, the dominant production process over the entire mass range is the gluon fusion, due to expected large gluon luminosity. There are also several decay channels of the Higgs particle through which the observation of it may be possible, and among them one is very interesting also in all the mass range; $H \rightarrow ZZ^{(*)} \rightarrow 4\ell$ channel. It is named as 'golden-plated' channel due to its high cross section and very clean signature of four leptons in the final state, which also allows a very accurate determination of the

[1] Conseil Europeenne pour la Recherche Nucleaire
[2] A Toroidal LHC AparatuS

Higgs mass once it is observed. For the analysis of this discovery channel, final state leptons need to be efficiently reconstructed and identified in the dedicated experiments.

Detection of muons and measurement of their properties is important for the analysis of many processes, like for the $H \rightarrow ZZ \rightarrow 4\ell$ channel, since they are the final state observables. There are several strategies for muon reconstruction and identification that are implemented in the software framework of the ATLAS experiment. Since muons have highly penetrating nature, outermost part of the ATLAS detector, the muon spectrometer, is dedicated for muon detection and measurements. However, algorithms that are including measurements also from the inner detector and the calorimeter, give a better muon reconstruction efficiency and muon momentum resolution. The muons that are not possible to be identified by using muon spectrometer measurements, due to traversing low-acceptance spectrometer regions or their insufficiently low momenta to traverse the muon spectrometer, can be identified by their enegy loss measurements obtained in the calorimeter.

The main purpose of this thesis is, to explain the improvements done to one of the calorimeter-based muon identification algorithms in the ATLAS experiment. Chapter 5 is meant to give a detailed description of the algorithm, explain the improvements done to it and show the effects of the improvements to its performance. The results obtained by application of the improved algorithm to the analysis of $H \rightarrow ZZ^{(*)} \rightarrow 4\ell$ channel is shown. Also, possible improvements in the future are discussed. In the Sections from 5.4 to 5.7, studies done by the author of this thesis are presented. Other chapters are included to support the main part of the thesis. A brief introduction to Standard Model is given in Chapter 2, to explain the present status of the theory and the motivation for new high energy physics experiments. The Large Hadron Collider and the ATLAS detector are overviewed in Chapter 3, to give an insight into the ATLAS experiment. Muon reconstruction and identification strategies developed for the ATLAS experiment are described and their performance is shown in Chapter 4, to make it clear in which sense calorimeter-based identification method would be complementary to the strategies based on muon spectrometer measurments.

The work presented in this thesis is a very small scaled contribution to ATLAS experiment, however, it is a big pleasure and honour to make even the smallest contribution to such a giantic and exciting experiment that will search for the smallest.

2. STANDARD MODEL OF PARTICLE PHYSICS, A BRIEF HISTORY

Prior to the Standard Model the answer to "what matter is made out of?" was rather simpler, however, explanation to some deep questions arising from observations and theoretical predictions, i.e., explanation of the strong force between baryons or the negative energy solutions of relativistic wave equation, was remaining superficial within this description. Deeper probing into the matter particles and deeper understanding of interactions at a more fundamental level brought deeper answers together with new questions. In this chapter, how these advancements in our knowledge has developed to bring about the Standard Model is briefly told and some questions within the Standard Model are addressed.

2.1. New particles

In the first half of the 20th century, when the positron, positively charged twin of the electron, and the muon, heavier version of the electron, were observed for the first time in cosmic ray experiments [1, 2], it caused a big surprise because these particles do not exist in ordinary matter. The existence of the positron was already postulated as a consequence of the Dirac equation [3], however, nobody was expecting the muon. More detailed studies showed that, muon is from the same family (lepton, leight-weight) with electron and coming from disintegration of another particle; the pion [4], which was also observed in the cosmic ray experiments. Pion is a middle-weight particle (meson), and it was fitting to Yukawa's description [5] of the mediator particle of strong interaction between protons and neutrons in the nuclei of every atom, thus, it was also welcomed. However, continuous experiments with high energetic cosmic particles led to the discovery of many more new middle-weight particles that extended the meson family, and also many heavy-weight paticles that are included in the same family with proton and neutron, the baryon family. With the invention of modern particle accelerators in the middle of the 20th century, more controllable high energy experiments continued

in the laboratories, which resulted in a discovery of even more mesons and baryons, collectively called hadrons. These unexpected new particles naturally caused a big excitement for theorists as well as experimentalists, and a big investigation started to account for their existence and for the mechanisms involved in their productions and decays.

2.2. Periodic table of the new paticles

The newly found hadrons were categorized as mesons and baryons according to their masses and it was not known that they actually have a substructure until the quark model [6, 7]. The development of the quark model was a consequence of a very succesfull arrangement of mesons and baryons into geometrical patterns according to their properties like charge and strangeness[3] , reminding the Periodic Table of elements. This classification, named as the Eightfold Way [8], was independently proposed by Gell-Mann and Ne'eman and its big success led independently Gell-Mann and Zweig to propose that all hadrons are composed of more fundamental particles; namely, the quarks. After the quark model we know that, mesons consist of quark-antiquark pairs ($q\bar{q}$) and baryons consists of three quarks (qqq) or three antiquarks ($\bar{q}\bar{q}\bar{q}$). First all the hadrons were described as a combination of three different kinds of quarks. In the following experiments with ever increasing energies, new heavier hadrons were found and the quark family extended to inculde six quarks. After a heavier third lepton, the tau, found, electron, muon and tau together with their corresponding neutrinos extended the lepton family also to include six members.

2.3. The Standard Model

After many years of challenging theoretical and experimental efforts, in the second half of the 20th century, the Standard Model (SM) has developed as a greatly accepted theory to explain the fundamental constituents of nature and three types of fundamental interactions - the electromagnetic, the strong and the weak interactions - that are

[3]In search for an explanation of production and decay mechanisms of new particles, a new property was assigned to each hadron, to which Gell-Mann gave the name strangeness.

responsible for their special behaviours; whose consequences would be what we observe directly or indirectly in all the physical phenomena occurs in nature, if the gravitational interaction could also be explained in this framework. SM is based on Quantum Field Theory (QFT), which is a framework that successfully reconciles quantum mechanics and special theory of relativity, and postulates that elementary particles are pointlike objects. Among many theories consistent with QFT, the Standard Model, which is a gauge theory characterized by a symmetry structure (a Lie group SU(3) $\times$ SU(2) $\times$ U(1)) and assignment of matter particles (three families of quarks and leptons) to symmetry patterns, has successfuly been confirmed by experimental observations by now.

Table 2.1. Some of the properties of Elementary Particles in the Standard Model. The values are from an update of 15 January 2008 [9].

Elementary Particles					
	Particle Type	Name	Charge [e]	Spin	Mass
Fermions	Quarks	up (u)	$\frac{2}{3}$	$\frac{1}{2}$	$2.55^{+0.75}_{-1.05}$ MeV
		down (d)	$-\frac{1}{3}$	$\frac{1}{2}$	$5.04^{+0.96}_{-1.54}$ MeV
		charm (c)	$\frac{2}{3}$	$\frac{1}{2}$	$1.27^{+0.07}_{-0.11}$ GeV
		strange (s)	$-\frac{1}{3}$	$\frac{1}{2}$	104^{+26}_{-34} MeV
		top (t)	$\frac{2}{3}$	$\frac{1}{2}$	171.2 $\pm$2.1 GeV
		bottom (b)	$-\frac{1}{3}$	$\frac{1}{2}$	$4.20^{+0.17}_{-0.07}$ GeV
	Leptons	electron (e)	-1	$\frac{1}{2}$	$\approx$ 0.511 MeV
		e-neutrino (ν_e)	0	$\frac{1}{2}$	$<$ 2 eV
		muon (μ)	-1	$\frac{1}{2}$	$\approx$ 105.66 MeV
		μ-neutrino (ν_μ)	0	$\frac{1}{2}$	$<$ 0.19 MeV
		tau (τ)	-1	$\frac{1}{2}$	$\approx$ 1.777 GeV
		τ-neutrino (ν_τ)	0	$\frac{1}{2}$	$<$ 18.2 MeV
Bosons	Gauge bosons	γ (photon)	$< 5 \times 10^{-30}$	1	$< 1 \times 10^{-18}$ eV
		g (gluon)	0	1	0
		$W^\pm$	$\pm$1	1	80.398 $\pm$0.025 GeV
		Z^0	0	1	91.1876 $\pm$0.0021 GeV
	Higgs boson	H^0	0	0	$>$ 114.4 GeV

Table 2.1 shows a familiar presentation of the SM as a list of the elementary particles with some of their properties, like charge, spin and mass. They are classified as fermions and bosons according to their spin. Fermions are half-integer spin (spin-1/2) matter particles and consist of quarks and leptons, whereas, bosons are integer-spin (spin-1) particles mediating the interactions. There is also a corresponding antiparticle to each fermion in the table. There exists a further classification for fermions as three generations[4] according to their masses, where the first generation fermions are being u, d, e, ν_e, the second generation fermions being c, s, μ, ν_μ and the third generation fermions being t, b, τ, ν_τ. The fermions belong to one generation differ only by their mass from the corresponding ones in another generation, however, the stable matter is made up only from the first generation fermions. Second and third generation fermions and their bound states have very short lifetimes, thus, do not exist naturally. They can only be produced and observed in high energy experiments, like cosmic ray experiments or experiments with particle accelerators.

The SM comprises two related theories; the Quantum Chromodynamics (QCD) accounts for the strong interactions, and the Glashow-Weinberg-Salam (GWS) theory describing the electromagnetic and weak interactions in a unified way. In the SM, all the fundamental interactions derive from the requirement of a local gauge invariance, and described as an exchange of a mediator particle - a gauge boson - between two elementary particles.

The strong interaction, described by the QCD theory, is exchange of a mediator particle - the gluon - between the colored particles - quarks and gluons. All the quarks carry a quantum number called color, in the same sense that electromagnetically interacting particles carry charge, but unlike charge, color has three different kinds; red, blue and green. In order to satisfy color conservation in a strong interaction, gluons carry color-anticolor, therefore, they also go through strong interactions by coupling to each other. A single quark has not been observed in any experiment until now, which firstly caused suspicion for their existence, but was later explained by a hypothesis

[4]The number of fermion generations is not fixed by the SM. Previous experiments do not exclude the existence of extra SM generations and there are theoretical arguments favoring the existence of a heavy fourth SM generation (see Appendix A).

called *confinement*, which showed itself in the experimental observations. The origin of the confinement is explained as; the strong coupling constant becomes very large for large distances, and above a distance of about 1 fm the potential energy gets large enough to create a quark-antiquark pair out of the vacuum. Therefore, quarks can only be observed in their bound states - hadrons - due to the long range behavior of the strong interaction. When a quark of an hadron gets scattered, it undergoes a process called *hadronization* (Figure 2.1); the seperation of the quarks that are scattered cause a creation of a quark-antiquark pairs and forms a jet of hadrons, which is finally observed in the experiments. Just as a jet formed by a leading quark, a jet may also be formed by a leading gluon produced in a strong interaction.

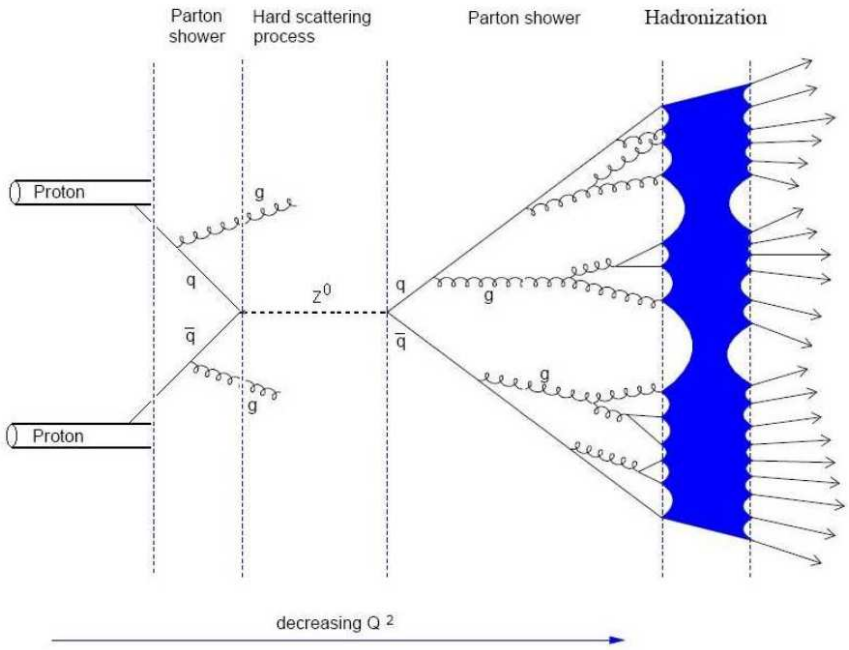

Figure 2.1. Hard scattering process of two quarks producing a Z boson and its decay into two quarks, which are forming hadronization [10].

The existence of quarks based on a theoretical prediction and because of the confinement isolated free quarks can not be observed, however, the consistency of the theory with the experimental observations shows their existence indirectly - under the mask of hadrons. After the development of the QCD theory and its agreement with the experimental evidence, we know that the mechanism involves in the production of hadrons is the strong interaction between the quarks. Moreover, what holds the protons

(and neutrons) together in the small volume of the nucleus despite the electric repulsion is strong interactions of six quarks, in the long-range behaviour formed by exchange of light mesons due to confinement. The longest range of the strong interaction is due to pion exchage since it is the lightest meson, that is the remnant of the Yukawa's pion-exchange model.

Electromagnetic interaction was known even in the 19th century, however, development of the quantum mechanics and the special theory of relativity in the 20th century, led to a more sophisticated formulation and interpretation of the interactions and resulted in the development of the Quantum Electrodynamics (QED) [11], which also provided a framework for the formulation of the other interactions. The electromagnetic interactions are mediated by the photon (γ) between the charged particles and the weak interactions by the intermediate vector bosons ($W^{\pm}$ and Z^0) between all the elementary particles. The theory that explains the weak interactions was put to its present form by Glashow, Weinberg and Salam and refered to as the GWS theory [12–14]. The GWS theory unifies weak and electromagnetic interactions, and treats them as different manifestations of a single electroweak interaction. The symmetry in the electroweak model requires the four interaction mediating bosons; γ, $W^{\pm}$ and Z, to be massless, however, this contradicted with description of the weak interactions with massive boson exchange. When a suitable mechanism for generation of massive boson mass was found, the electroweak theory had successfully predicted the observation of W and Z bosons. In addition, the model also requires the fermions to be massless. Masses of both the fermions and the bosons are introduced by spontaneous breakdown of the electroweak symmetry, without destroying the underlying gauge symmetry. The explanation for this broken symmetry in SM is provided by the Higgs mechanism [15–17], postulated by P. W. Higgs. In this mechanism, the gauge bosons and fermions interact with a Higgs field with coupling proportional to their masses and as a result they no longer appear to be massless. The theory predicts the existence of a massive scalar neutral particle, the Higgs boson (H), associated with the Higgs field, that has not been observed in any experiment yet.

2.4. SM Higgs searches and four lepton final state

The predicted Higgs boson is the only remaining particle to be discovered within the SM. The mass of the Higgs boson is not predictable from the theory, however, there are theory- and experiment- based constraints on it. Stability and consistency requirements of the theory predicts that its mass has to be below $\sim$ 1 TeV [18]. Experimentally, non-observation of the $e^+e^- \rightarrow HZ$ process at LEP experiments put a lower limit m_H >114.4 GeV at 95% confidence level [19], and precision measurements of electroweak observables at LEP and Tevatron set the upper limit for the Higgs mass of m_H <190 GeV at a confidence level of 95% [20]. The LHC will enable the analysis to explore the full range of allowed Higgs masses and the expectation for discovery is very high.

There are many different signatures for observation of the Higgs boson. Theoretical predictions for the production mechanisms lead to improved search strategies. In Figure 2.2, the cross sections for Higgs production channels at LHC are shown as a function of the Higgs mass. Main production channels (see Figure 2.4) can be listed as follows [21]:

- Gluon fusion - In this process, the Higgs couples to gluons through a heavy-quark loop.
- Vector boson fusion (VBF) - This production mechanism occurs as the scattering between two (anti)quarks with weak boson (W or Z) exchange and with the Higgs boson radiated off the weak-boson propagator.
- Associated production with top quark - In this process, the Higgs boson is radiated off one of the two top quarks in the $q\bar{q}$, gg s-channel or off the top propagator in the gg t-channel at LO.

Gluon fusion will be the dominant production channel for any mass value, due to large gluon luminosity at the LHC. Altough its cross section is $\sim$20% smaller than the gluon fusion one, VBF is also a promising channel. When a high luminosity is reached, associated production with top quark will also be important in the low-mass region.

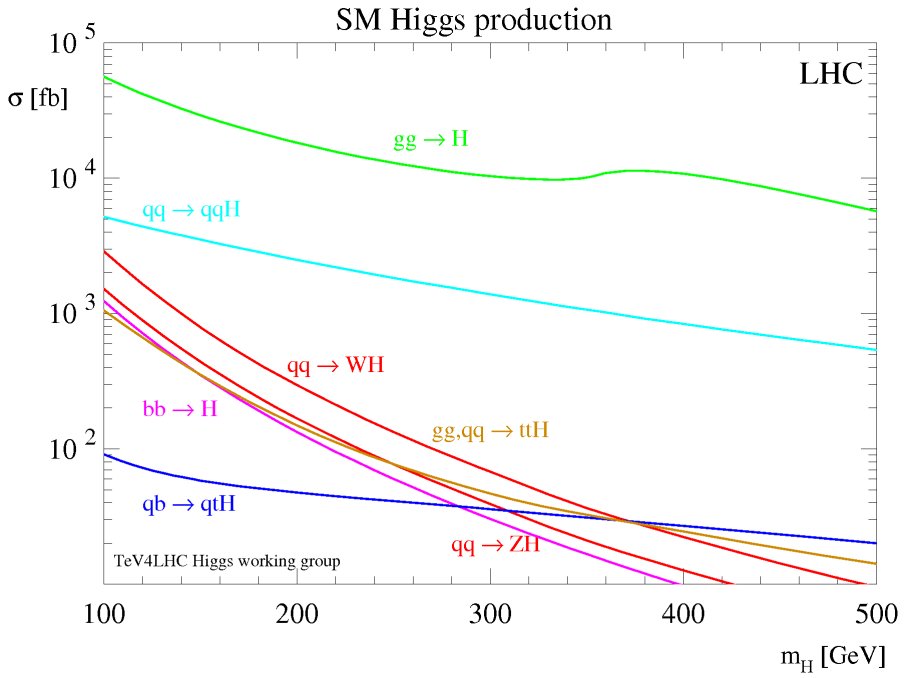

Figure 2.2. Higgs production cross sections at the LHC as a function of Higgs mass [9].

Branching ratios of the Higgs boson for different decay channels are shown in Figure 2.3 as a function of the Higgs mass. Higgs observation in the low mass region, where decays into heavy quarks or τ leptons have big branching ratios, will be challenging due to the large QCD background at LHC. For Higgs masses up to 130 GeV the most promising decays are into photons and τ leptons. The branching ratio for $H \rightarrow \gamma\gamma$ channel is very low, however it gives a clean final state, where reconstruction of the primary vertex is very important for its analysis. $H \rightarrow ZZ$ and $H \rightarrow WW$ are the most promising channels in the high mass region (m_H >150 GeV). ZZ channel becomes dominant when the Higgs mass is sufficient for production of two on-shell Z bosons. However, discovery potential of these channels is reducing for Higgs mass $m_H > 350$ GeV due to availability of the $t\bar{t}$ channel.

Four lepton final state of ZZ channel, $H \rightarrow ZZ \rightarrow 4\ell$, is very important over a wide mass range, due to its high production cross section and very clean final state consisting of leptons. It is also important for accurate determination of the Higgs mass. Lepton identification and reconstruction performance is of high importance for

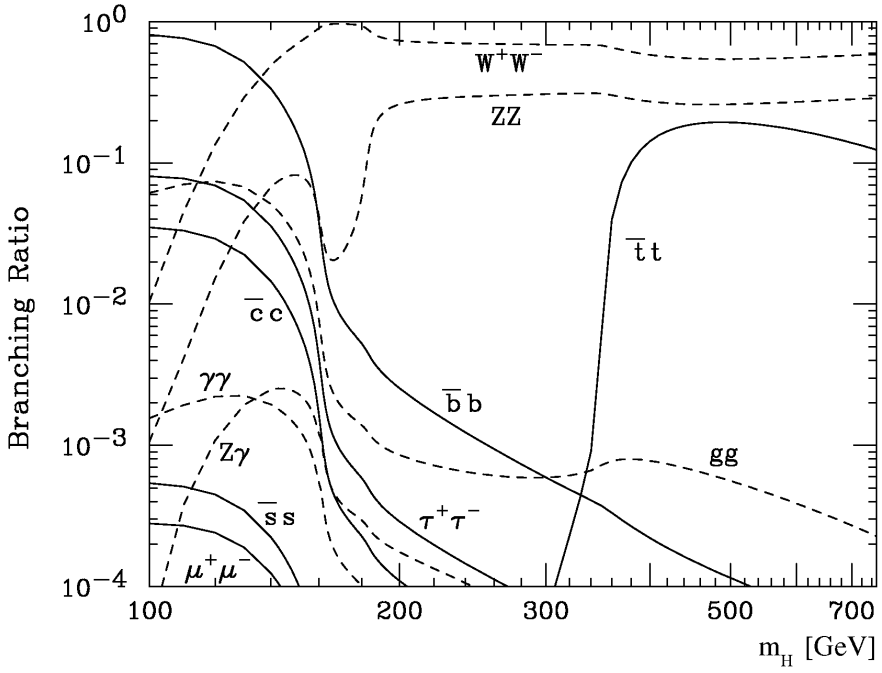

Figure 2.3. Higgs branching ratios at the LHC as a function of Higgs mass [9].

the analysis of this channel. Using the data from $Z \rightarrow 2\ell$ events may provide a measurement of the lepton performance, and will allow to keep the systematic effects arising from lepton momentum resolution and lepton identification efficiency under control. Analysis of this channel in the mass region 125 - 150 GeV is difficult because, due to phase space constraints one of the Z bosons is off-shell and couples to low-p_T leptons. The main backgrounds for this channel which gives the same final state consist of; $ZZ^*/\gamma^* \rightarrow 4\ell$, $Zb\bar{b} \rightarrow 4\ell$ and $t\bar{t} \rightarrow W^+bW^-\bar{b} \rightarrow 4\ell$ proccesses. ZZ^* gives the biggest contribution to background, which is irreducible due to its identical final state with the signal. $Zb\bar{b}$ and $t\bar{t}$ are reducible backgrounds, since their rejection in the analysis is possible due to the presence of b-jets in their final states. Examples of the Feynman diagrams for the irreducible and reducible background processes are given in Figure 2.5.

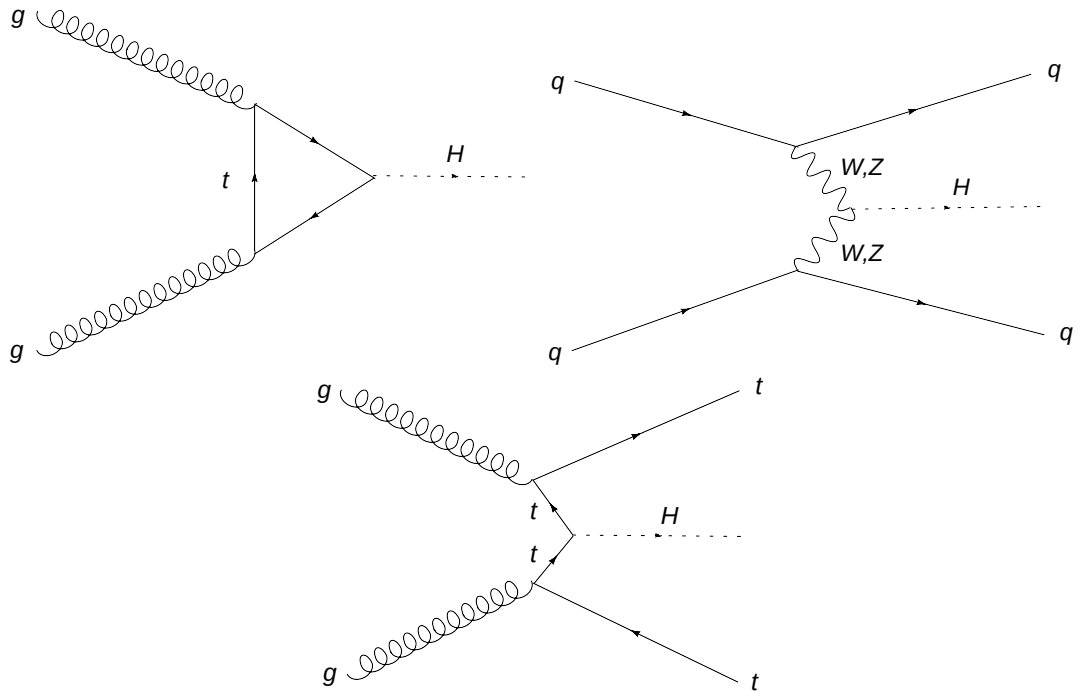

Figure 2.4. Examples of the Feynman diagrams for gluon fusion, vector boson fusion and associated production with t-quark processes.

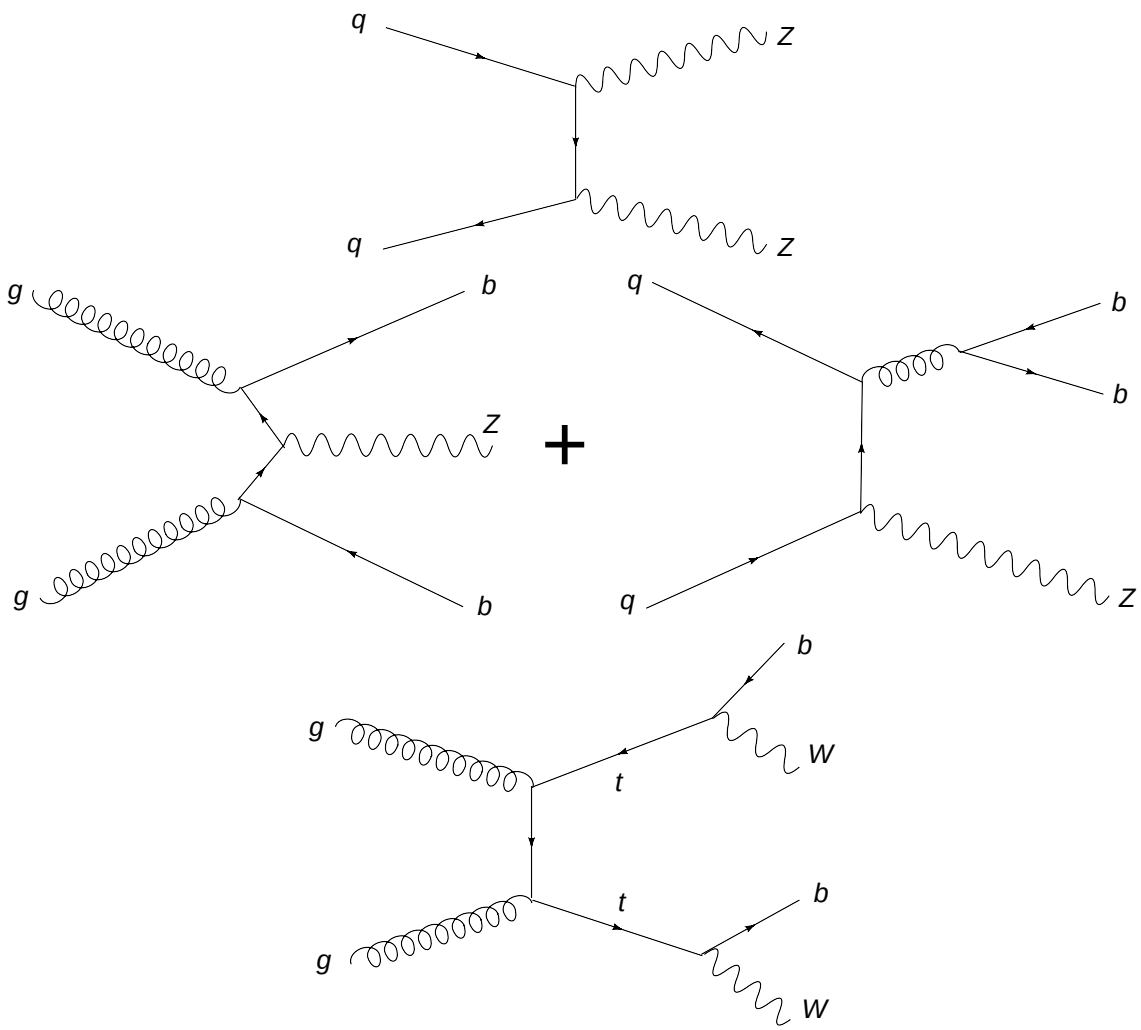

Figure 2.5. Examples of the Feynman diagrams for ZZ^*/γ^*, $Zb\bar{b}$ and $t\bar{t}$ processes.

3. THE ATLAS EXPERIMENT

The ATLAS detector covers one of the interaction points at the LHC, where the proton-proton collisions are going to take place. It will detect the consequences of these collisions for the analysis of the resultant phenomena, and eventually for a better understanding at the fundamental level. Groups of scientists from many countries are working for the ATLAS experiment by collaborating through CERN, the European laboratory for particle physics research. CERN was officially establised in 1954 and since then its mission has been to provide international collaboration in research of a pure scientific and fundamental character, without any concern with work for military requirements. Today, around 8000 scientists from 85 nationalities come to CERN for their research. Owing to its collaborational structure, from 1954 to now, it has been the laboratory of many important discoveries in particle physics and other branches of science.

The LHC, world's most powerful accelerator for particle physics research, is the new potential discovery machine at CERN. It is a two-ring-superconducting-hadron accelerator and collider installed in the existing 26.7 km tunnel that was constructed for the Large Electron-Positron Collider (LEP). It spans the border between Switzerland and France about 100 m underground. Being the highest luminosity and energy particle accelerator in the world, LHC has a high discovery potential for new physics. The approval of the LHC project was given by the CERN Council in December 1994. In 2000, LEP was closed to liberate the tunnel for the LHC. On 10th of September 2008, first proton beams succesfully circulated in both directions (without collision events) and the ATLAS detector recorded the particles from this testbeam to debug and setup the detector (see [22]). Following this testbeam, LHC was shutdown due to an incident in the tunnel [23]. In the winter time it will not operate for cost savings and improvements and in some parts of this period, ATLAS detector will use cosmic ray events to commission and tune the detector. After the planned shutdown, the startup of LHC and first collisions will take place in Summer 2009. It is going to operate with an initial low-luminosity (factor of ten smaller than the design luminosity) at the

beginning and the design luminosity is planned to be reached after one year of low-luminosity running. The ATLAS detector will start taking collision data and searching for discoveries when the LHC starts operating. Data taking is planned to continue for 15-20 years.

This chapter intends to give an overview of the LHC accelerator and the ATLAS detector, that are documented very detailed in [24–28].

3.1. The LHC

The LHC is a particle-particle accelerator and collider, therefore, has two rings with counter-rotating beams, unlike particle-antiparticle accelerators that can have both beams in a single ring. The particles will be accelerated in opposite directions in the two seperate (intersecting) rings, and will be brought to collisions at four different bunch-crossing points in the center of the detectors. LHC is designed to collide proton beams with a centre-of-mass energy of 14 TeV and a design luminosity of $10^{34}\text{cm}^{-2}\text{s}^{-1}$. It will also collide lead (Pb) ions at 5.5 TeV per nucleon pair, at a design luminosity of $10^{27}\text{cm}^{-2}\text{s}^{-1}$, for the study of heavy ion collisions.

Center-of-mass energy in the collisions is an important parameter for the colliders. To observe and study the physical effects that have not been observed yet, would only be possible if the energy of the collision is sufficiently high for their creation. Since, the higher the energy of a collision, the heavier the particle produced, LHC has a high discovery potential for new heavy particles with its highest center-of-mass energy ever reached in the accelerators. It also provides the possibility to study interactions at a very short range, since higher energies allow particles to get closer together before they are scattered.

Luminosity (L) is another important parameter to define the performance of a collider and is completely determined by the properties of collidig beams. For LHC,

the luminosity can be expressed in terms of the beam parameters by equation 3.1 [27],

$$L = F\frac{f\sum_i N_1^i N_2^i}{4\pi\sigma_x^*\sigma_y^*} \tag{3.1}$$

where f is the beam-revolution frequency, F is a factor which accounts for the non-zero crossing angle, N_1^i, N_2^i are the numbers of protons in the colliding bunches and σ_x^*, σ_y^* are the transverse bunch widths at the interaction point. According to this equation, one can see that, bunches should be high populated and collide at a high frequency with a small collision area to achieve a high luminosity in a collider. The event rate R of a given physical process is determined by luminosity L together with the cross section σ_{event} of that process:

$$R = \frac{dN_{event}}{dt} = L \cdot \sigma_{event} \tag{3.2}$$

To calculate the expected number of events for the specific event under study, the event rate R has to be integrated over time:

$$N_{event} = \int \sigma_{event} \cdot L(t)dt = \sigma_{event} \int L(t)dt = \sigma_{event} \cdot \mathbf{L} \tag{3.3}$$

The measurement of the integrated luminosity $\mathbf{L}$ has to be as precise as possible because it is used to convert the observed number of events to the cross section of the physical process. Since the lumnosity is related to the event rate of a physical process, high luminosity is necessary to make maximum observations in the available time. Moreover, the LHC experiments search for physical processes which happen very rarely and mostly dominated by background processes that give the same signature but produced by other effects which have much larger cross sections. Higher luminosity provides larger statistics and makes it possible to distinguish the signal from background events.

Inside the LHC, bunches of up to 10^{11} protons, each with an energy of 7 TeV, will collide 40 million times per second. With an inelastic proton-proton cross section of 60 mb, the number of inelastic scatterings per bunch crossing will be on average 19. However, most of these events will not come from hard-scattering which leads to

interesting events, but will consist of inelastic scatterings with low momentum transfer. These events, other than the one of primary interest, are called pile-up events. Due to the low cross section of interesting events, high luminosity is very important for the LHC.

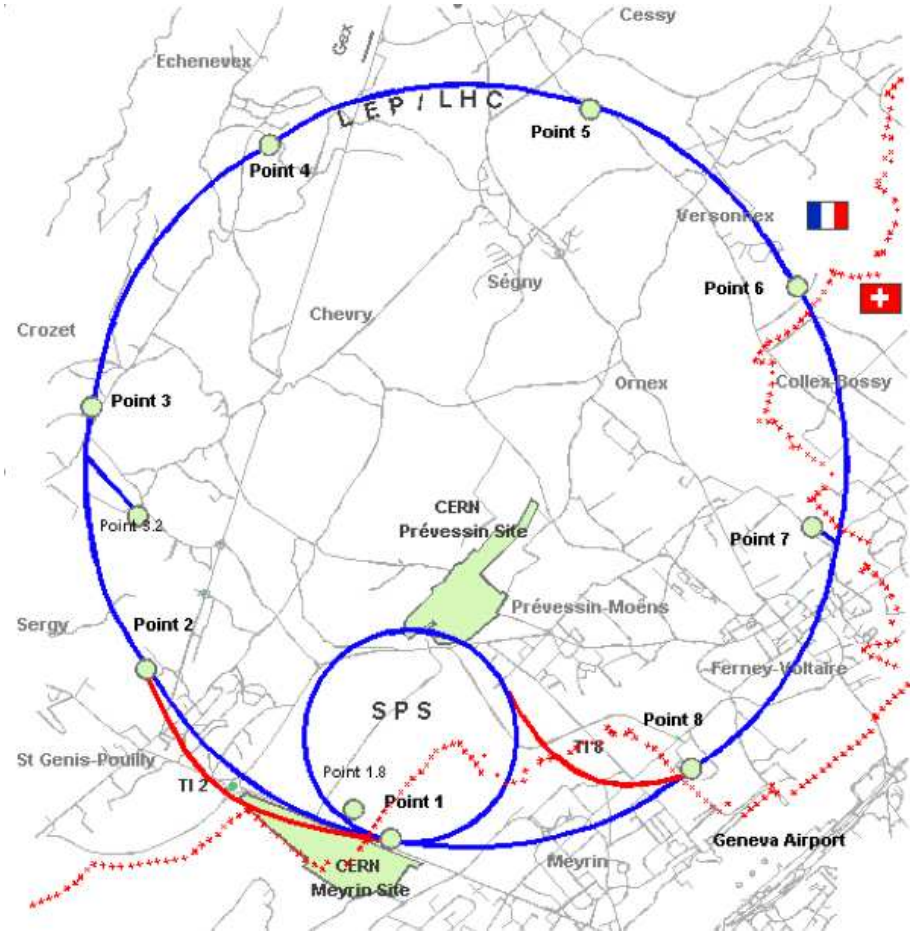

Figure 3.1. Schematic view of the LHC and SPS accelerators.

Before protons are injected into the LHC, they will be accelerated in a set of smaller accelerators and gain energy by these successive accelerations. Finally, Super Proton Synchrotron (SPS) will accelerate and inject them into the LHC at 450 GeV in both directions, where they will be accelerated to their final energy of 7 TeV. Figure 3.2 shows the basic layout of the LHC. It has eight straight sections, each followed by a section consists of dipole magnets that bends the path of the particles to keep them on a circular trajectory. To achieve this, superconducting dipole magnets, which cover ∼20 km of the ring, kept at a temperature of 1.9 K, with a maximum field strength of

8.33 T are used. Four straight sections have an interaction point for the beams, where detectors are installed and the collisions take place in the center of the detectors. The beams are focused using quadrupole magnets in the straight sections of the ring, to boost the luminosity at the interaction points. The remaining four straight sections do not have beam crossings. Two straight sections contain collimation systems that clean the beam halo, one straight section contains the beam dump and another staright section contains two RF systems (one independent system for each beam), for the initial acceleration and to compensate for the energy loss through synchrotron radiation.

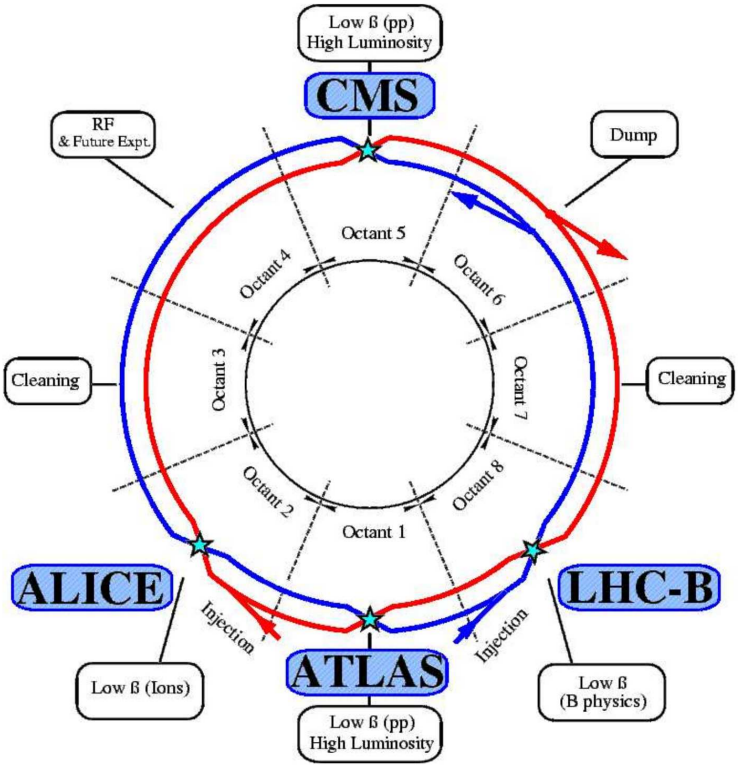

Figure 3.2. Schematic layout of the LHC [25].

The two high luminosity detectors, ATLAS [28] and CMS [29], are located at diametrically opposite straight sections on the LHC ring. Both of them, aiming at a peak luminosity of L = 10^{34} cm^{-2} s^{-1} for proton operation, are large multi-purpose detectors optimized for discovery of new highly energetic particles. There are also two low luminosity experiments: LHCb [30], aiming at a peak luminosity of L = 10^{32} cm^{-2} s^{-1}, is dedicated to precision measurements of CP violation and rare decays of B-hadrons, and TOTEM [31], aiming at a peak luminosity of L = 2×10^{29} cm^{-2} s^{-1},

is located at the same interaction point with CMS and will detect the protons from elastic scattering at small angles. In addition to the proton beams, the LHC will also be operated with lead ion beams. With the nominal magnetic field of 8.33 T in the dipole magnets, these ions will have a beam energy of 2.76 TeV/nucleon and a nominal luminosity of 10^{27} cm^{-2} s^{-1}. The LHC has one dedicated ion experiment, ALICE [32], which will mainly focus on the strong interaction sector of Standard Model and physics of the quark-gluon plasma. However, CMS and ATLAS detectors also plan to study ion collisions.

Table 3.1. Some basic parameters of the LHC relevant for the peak luminosity [24].

		Injection	**Collision**
Parameter	**Unit**	**Value**	
Beam Data			
Proton energy	[GeV]	450	7000
Number of protons per bunch		1.15×10^{11}	
Number of bunches per beam		2808	
Bunch spacing	[ns]	24.95	
Frequency of bunches	[MHz]	40.08	
Peak Luminosity Related Data			
RMS bunch length	[cm]	11.24	7.55
RMS beam size at ATLAS and CMS	[μm]	375.2	16.7
Peak luminosity in ATLAS and CMS	[cm^{-2} s^{-1}]	1.0×10^{34}	
Interaction data			
Inelastic cross section	[mb]	60.0	
Total cross section	[mb]	100.0	
Events per bunch crossing		19.02	
Main Magnet			
Number of dipole magnets		1232	
Dipole magnet temperature	[K]	1.9	
Dipole field strength	[T]	0.535	8.33

3.2. ATLAS detector overview

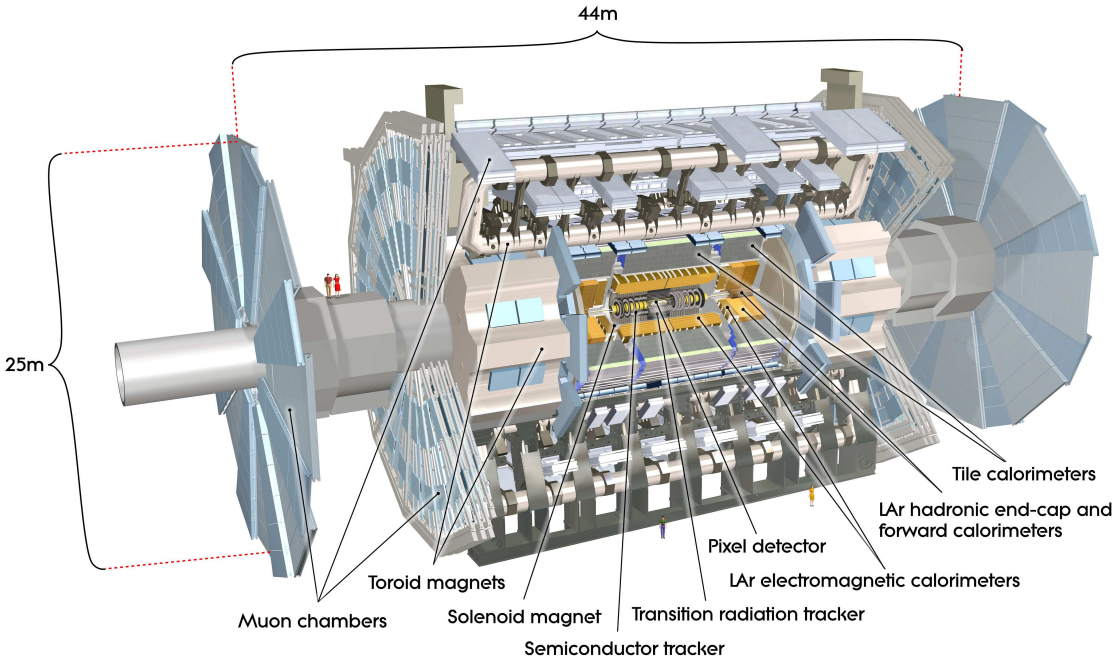

Figure 3.3. Cut-away view of the ATLAS detector [28].

The ATLAS detector, shown in Figure 3.3, is housed at the southern interaction point of the LHC ring, close to the CERN main site. It has a layered design with nearly complete 4π coverage around the interaction point. It has approximately cylindrical symmetry and is described with a coordinate system that has its origin at the nominal interaction point. The beam direction defines the z-axis and the x-y plane is transverse to the beam direction. The positive x-axis is defined as pointing from the interaction point to the centre of the LHC ring and the positive y-axis is defined as pointing upwards. Besides the standard Cartesian coordinate system, especially for physics analyses, a coordinate system with (r, ϕ, θ) is defined, where r is the transverse radius measured from the beam-pipe, ϕ is the azimuthal angle measured from the x-axis around the beam-pipe and θ is the polar angle measured from the beam-pipe. Pseudorapidity, a commonly used parameter in particle physics and also in the ATLAS experiment, is defined as the equation 3.4,

$$\eta = -ln\left(tan\left(\frac{\theta}{2}\right)\right) \tag{3.4}$$

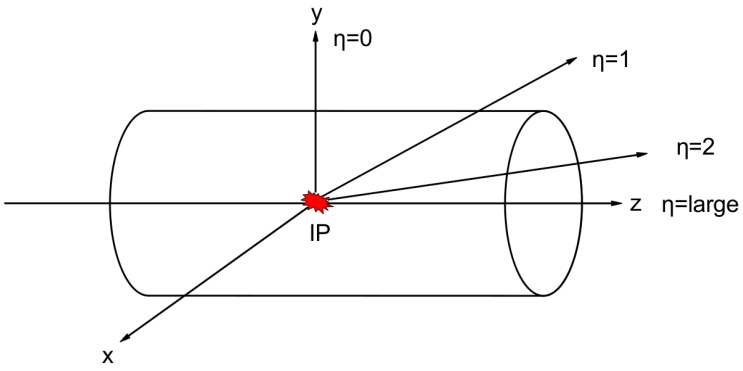

Figure 3.4. Illustration of pseudorapidity.

where, θ is the azimutal angle measured from the beam pipe. Pseudorapidity is an approximation of the rapidity[5] in the relativistic limit, which is usually defined in particle physics as the equation 3.5,

$$y = \frac{1}{2} ln \frac{E + p_L}{E - p_L} \tag{3.5}$$

where, E is the energy of the particle and p_L is the longitudinal component of the momentum of the particle. In the case of massive objects such as jets, the rapidity y is used. Both rapidity and pseudorapidity are small for the particles in the central regions and larger for the ones in the forward regions, thus, useful parameters in high energy physics for describing particles in a detector.

In the ATLAS experiment a highly relativistic particle is often described in terms of three parameters: transverse momentum (p_T), preudorapidity (η) and azimuthal angle (ϕ). The transverse momentum p_T, the transverse energy E_T and the missing transverse energy E_T^{miss} are defined in the x-y plane. And another often used variable is the distance ΔR in the pseudorapidity-azimuthal angle space, which is defined as $\Delta R = \sqrt{\Delta\eta^2 + \Delta\phi^2}$.

ATLAS is a general-purpose proton-proton detector designed to exploit the full

[5]Rapidity, $ln[\gamma(1+\beta)]$, is the hyperbolic angle of the Lorentz transformation in the hyperbolic rotation representation.

discovery potential of the LHC. The major goal for ATLAS is the search for the SM Higgs boson. There is a range of production and decay mechanisms, depending on the mass of the Higgs boson. Thus, the detector is optimized for the sensitivity to the largest possible Higgs mass range. Some of the other important goals are the searches for heavy W and Z-like objects, for the Higgs boson beyond the Standard Model, for supersymmetric particles, for compositness of the fundamental fermions, for the investigation of CP violation in b-decays and so on [26]. Also, more precise measurments of Standard Model parameters will be possible due to high luminosity and rich physics potential of the LHC. And, it is important to note that, at the TeV energy scale, which had not been explored before, it is also possible to observe unexpected new phenomena. To observe and analyse all the expected and unexpected phenomena, the detector must be designed and optimized to provide essential signatures of the events. The necessary informations to analyse an event consist of; identification of the observables such as, electron, photon, muon, tau and hadronic jets, measurement of their important parameters such as, η, ϕ, p_T and E_T and E_T^{miss}, reconstruction of vertices and other event information [27]. To support the physics goals and experimental conditions at the LHC, a number of requirements have been set for the design of the detector including:

- High-granularity detectors to cope with the high particle fluxes.
- Fast and radiation-hard electronics and sensor elements.
- Large acceptance in both pseudorapidity and azimuthal angle.
- Good charged-particle momentum resolution and track reconstruction efficiency.
- Vertex detectors close to the interaction region for efficient vertex reconstruction.
- Very good electromagnetic calorimetry for electron and photon identification and measurements, complemented by full-coverage hadronic calorimetry for accurate jet and missing transverse energy measurements.
- Good muon identification and muon-momentum resolution over a wide range of momenta.
- Highly efficient triggering on low transverse-momentum objects.

As common for collider experiments in high-energy physics, the ATLAS detector consist of different components with specific goals. These components provide the

needed information about the particles that traverse the detector for analysing the physical processes emerge from the collison of particles. A central tracking detector, closest component to the interaction point and contained in a solenoid magnet, provides measuremets of the position and momentum of the charged particles. A calorimeter system that surrounds it, provides measurements of the energies of charged and neutral particles. A toroidal magnet system comes after and provides the magnetic field for the muon system to measure the momentum of muons independently. In the following sections these sub-detectors will be described to some extent.

3.2.1. Inner detector

The inner detector (ID) [33] is the first component of ATLAS around the beam pipe, with its innermost layer placed only a few centimeters away from the interaction point. It is a tracking detector, responsible of reconstructing the paths of the charged particles, called track, and measuring their momentum. The ID is contained in a central solenoid magnet [34] that generates a magnetic field of 2 T, which bends the paths of the charged particles traversing the ID. This magnetic field allows the measurement of mometum of particles by measuring the curvature radius of their trajectories in the transverse plane, and the direction of the curve reveals the sign of the charge. The ID is also responsible for measuring the position of the vertices, which is a space-point where two or more particles are created. The primary vertex is defined as the vertex with the highest sum of transverse momenta of the tracks originating from it, whereas, the secondary vertex is the vertex of particles that come from a long-lived particle decaying in the detector volume. Measuring the positions of vertices may help to identify long-lived particles, such as τ-leptons and b-hadrons, by the distance of the secondary vertex to the primary vertex.

The ID has three independent sub-detectors: Pixel detector, SemiConductor Tracker (SCT) and Transition Radiation Tracker (TRT). Each one arranged in several layers and consists of a central barrel region and two end-cap regions at the ends of the barrel, as seen in Figure 3.5.

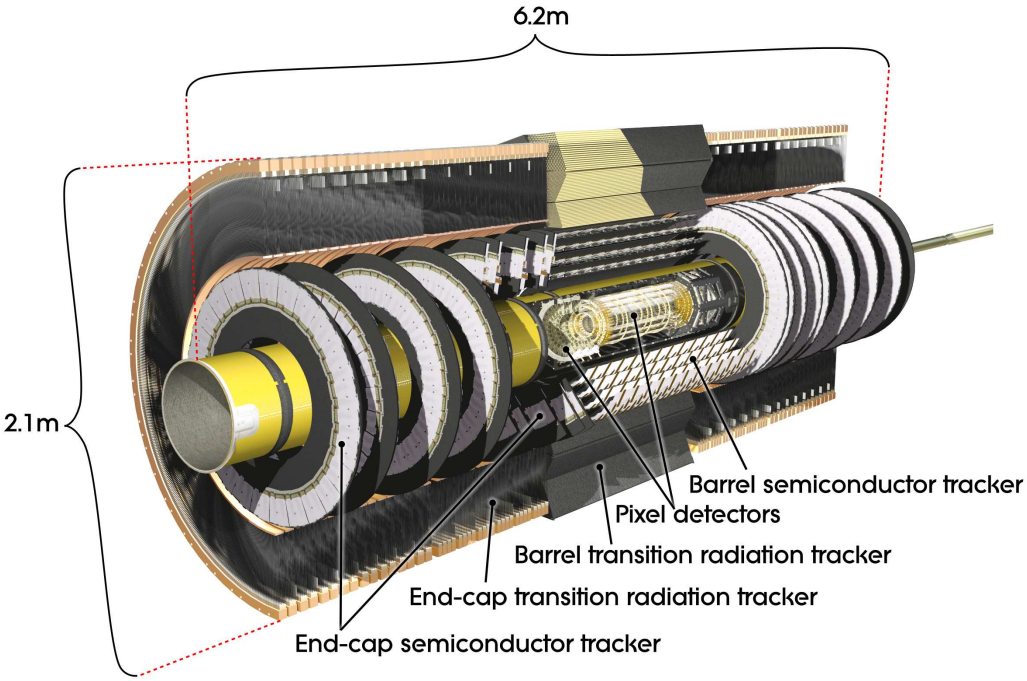

Figure 3.5. Cut-away view of the ATLAS Inner Detector [28].

Given the very large track density expected at the LHC, high-granularity detectors are needed for precise tracking information. Therefore, pixel detector followed by SCT, two high-precision tracking detectors, are placed at the inner radii providing discrete space points and cover the region $|\eta| < 2.5$. They are placed on concentric cylinders around the beam axis at smaller η (barrel region), so that they are parallel to the beam pipe, whereas, at larger η (end-cap region), they are placed on disks perpendicular to the beam pipe. This choise allows particles with different η to travers as many layers as possible. The silicon pixel detector is located in the innermost region of the ID, covering the vertex region. It is a very high-granularity detector and will provide excellent tracking and vertex resolution. It is formed by three pixel layers segmented in r-ϕ and z (r), which gives three high-precision space-points per track, both in the barrel and end-cap. The pixel dimensions are $50 \times 400\ \mu m^2$. For a single pixel, the spatial resolution is on average 10 μm in r-ϕ plane and 115 μm in z direction in the barrel and in r direction for the end-cap. Pixel detector is the closest sub-detector to the beam pipe, therefore, it is designed to be able to cope with a high particle density and extreme radiation environment. The silicon microstrip detector (SCT), surrounds the pixel detector, composed of eight strip layers, and gives four space-points per track.

The basic element is a $6.36 \times 6.40\ cm^2$ single-sided p-in-n silicon detector. The spatial resolution is on average 17 μm in r-ϕ plane and 580 μm in z direction in the barrel and r direction in the end-cap.

At the outer radii, a large number of track position measurments ($\sim$36 hits per track) is done by the TRT, over the coverage of $|\eta| < 2.0$. It significantly contributes to momentum measurement by the measurmenets of the track position in a large number of straws. It also provides electron identification through transition radiation measurements over a wide range of energies (0.5 GeV - 150 GeV). TRT consists of 4 mm diameter straw drift-tubes, filled with xenon-based gas mixture. In the barrel region the straws are (embedded in fiber radiator material) parallel to the beam axis and are 144 cm long, in the end-cap region the 37 cm long straws (embedded in foil radiator material) arranged radially in wheels. This geometry allows for approximately constant number of straws crossed by tracks with $p_T > 0.5$ GeV over the full pseudorapidity coverage. The TRT only provides r-ϕ information with a single-point resolution of 130 μm per straw. The straw tubes are gaseous proportional counters fitted with a gold-plated tungsten wire (the sense wire). The aluminum coated straw wall is held at a negative high voltage acts as a cathode. When a charged particle pass through the straw, it cause ionizations in the gas and the electrons drift towards the anode wire and forming an avalanche close to the wire. The straw tube functions as an ionization chamber in the proportional regime, since the charge collected on the wire is proportional to the ionizing particle energy loss. The position measurements of tracks are done by accurate detection of the time that electrons take to drift to the anode wire. Electron identification is achieved by detection of transition radiation photons in the xenon-based gas mixture of straw tubes. Transition radiation is produced when highly relativistic charged particle crosses an inhomogeneous medium, in particular the boundary between two materials with different dielectric constants, and radiate low energy photons. The number of emitted photons increases with the Lorentz γ factor of the particle, which is different for particles with the same momentum but different mass, hence offers the possibility of particle identification at highly relativistic energies. In TRT straw tubes, transition radiation photons are created in a radiator material between the straws and these photons are absorbed in the xenon-based gas in-

side the straw tubes. The detection of transition radiation photons leads to a stronger signal than the signal of a pure ionizing particle and the readout electronics is capable of distinguishing these signals.

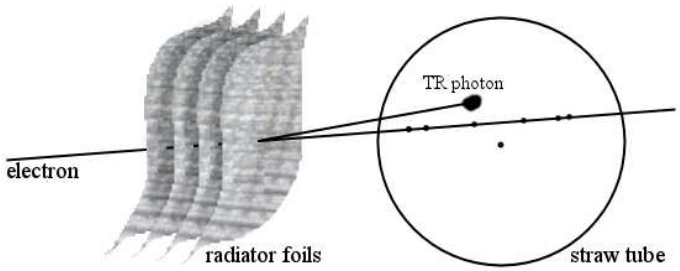

Figure 3.6. Drawing showing a transition radiation photon is emitted at low angle when a high momentum electron crosses the boundary of materials with different dielectric constants. [35].

Two thresholds are applied to the signals from the straws; a low threshold ($\sim$ 250 eV) to detect usual energy loss hits in the gas, and a high threshold ($\sim$ 5 keV) for the transition radiation hits. The high threshold is optimized to distinguish between electron and pion hits, since electrons typically produce more high threshold hits than pions.

Figures 3.7 shows the elements traversed by a charged track of 10 GeV p_T with $\eta =$ 0.3 in the ID. The track traverses successively the beryllium beam-pipe, the 3 cylindrical silicon-pixel layers, the 4 cylindrical double layers of barrel SCT, and approximatey 36 axial straws of barrel TRT. Figure 3.8 shows the elements traversed by two charged tracks of 10 GeV p_T with $\eta = 1.4$ and 2.2 in the ID. The track at $\eta = 1.4$ traverses successively the beryllium beam-pipe, the 3 cylindrical silicon-pixel layers, 4 of the disks with double layers of end-cap SCT, and approximately 40 straws of end-cap TRT. In contrast, the track at $\eta = 2.2$ traverses successively the beryllium beam-pipe, only the first of the cylindrical silicon-pixel layers, two end-cap pixel disks and the last four disks of the end-cap SCT. The coverage of the end-cap TRT does not extend beyond $|\eta| = 2$ [28].

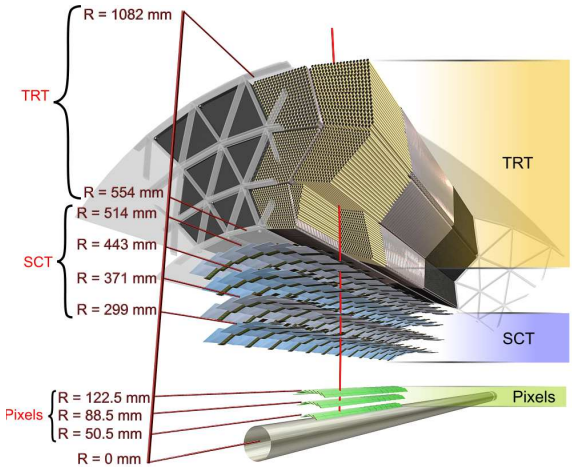

Figure 3.7. Drawing showing the elements traversed by a charged track of 10 GeV p_T with $\eta = 0.3$ in the ID [28].

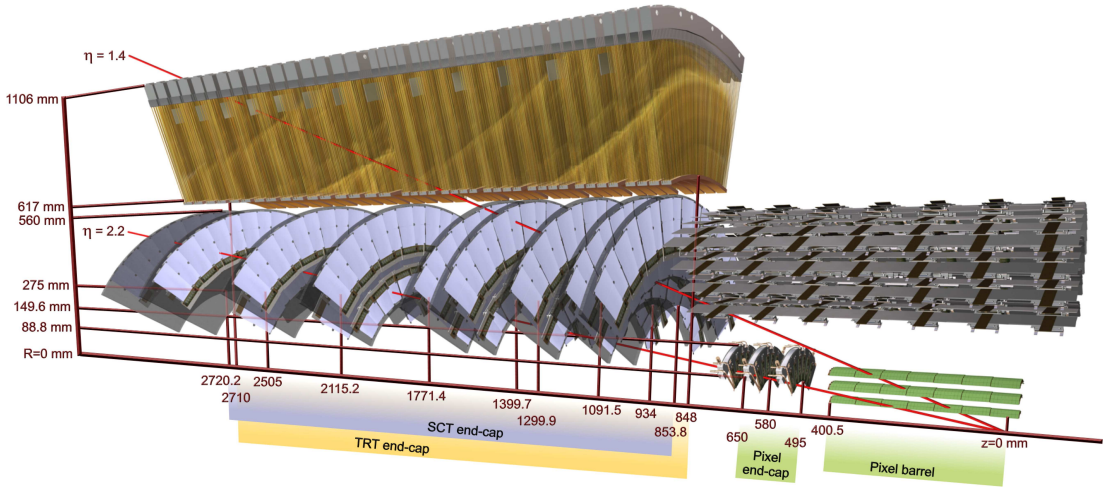

Figure 3.8. Drawing showing the elements traversed by two charged tracks of 10 GeV p_T with $\eta = 1.4$ and 2.2 in the ID [28].

3.2.2. Calorimeter

The calorimeter measures the energy of charged and neutral particles by absorbing it. It also contributes to the particle identification.

The calorimeter system [36–38] of the ATLAS detector consists of three subsystems with different functions, where the whole system is divided into a barrel part and two end-cap parts. Figure 3.9 shows a sectional drawing of the calorimeter system and

its subsystems. The subsystem close to the beam line is the Electromagnetic Calorimeter (EMCal), which is optimised for measurement of the energy of electromagnetically interacting particles, mainly photons and electrons. The other one wrapping around the EMCal is the Hadronic Calorimeter (HCal), which is responsible for measuring the energy of charged and neutral hadrons. The final calorimeter subsection is a combined one in the two forward regions placed inside the end-caps, called the Forward Calorimeter (FCal), measuring all particle types with small angles to the beam axis. Its main fuction is to quantify the missing energy.

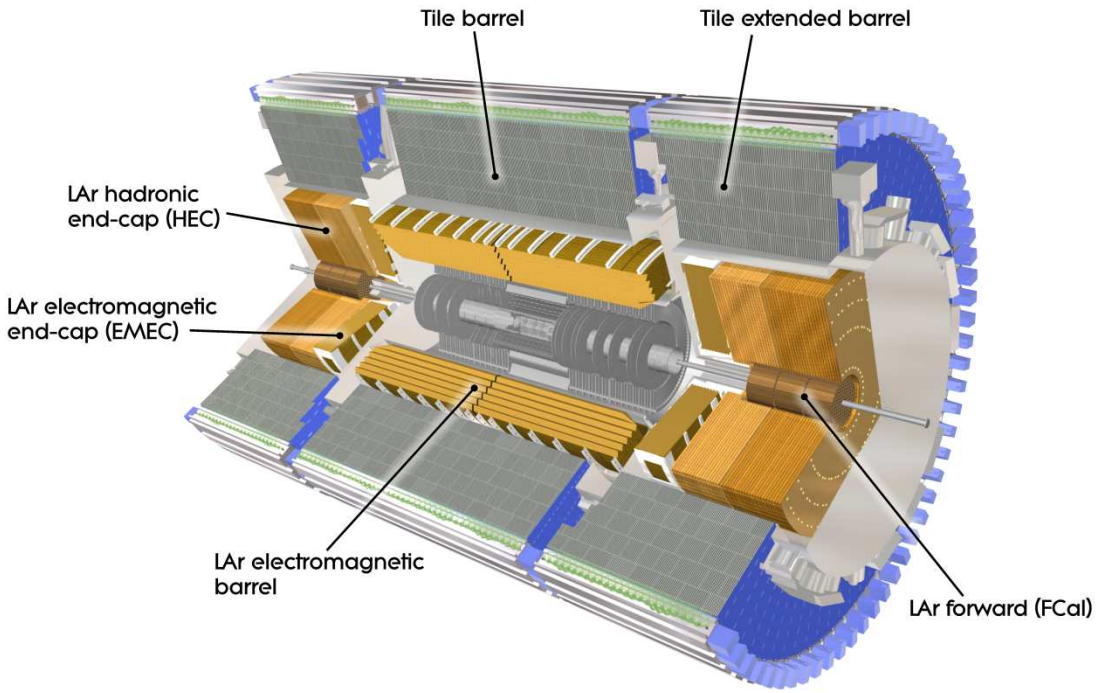

Figure 3.9. Cut-away view of the ATLAS Calorimeter System [28].

The calorimeters consist of metal plates (absorbers) and sensing elements (active material). Interactions in the absorbers transform the incident energy into a shower of particles that are detected by the sensing elements. When the sensing element is liquid argon (LAr), the showers in the argon liberate electrons that are collected and recorded, whereas, for the sensors that are tiles of scintillating plastic, the showers cause excitation of atoms of the scintillating medium and the plastic emit light which is detected and recorded.

The electromagnetic calorimeter is divided into a barrel ($|\eta| < 1.475$) and two end-cap ($1.375 < |\eta| < 3.2$) parts. It is a sampling calorimeter with liquid argon as active material and a lead absorber. It has accordion-shaped electrodes and absorber plates over its full coverage. The accordion geometry avoids cracks in the azimuthal direction, hence provides a full ϕ coverage and also allows to have several active layers in debth. The readout electrodes [39] are located in the gaps between the absorbers and cosist of three conductive copper layers. The two outer layers are at the high voltage potential and the inner one is udes for reading out the signal. Furthermore, in the region of $|\eta| < 1.8$, a presampler detector is positioned infront of the electromagnetic calorimeters, which provides a measurement of the energy lost by particles until they reach the electromagnetic calorimeters. The presampler consists of an active LAr layer.

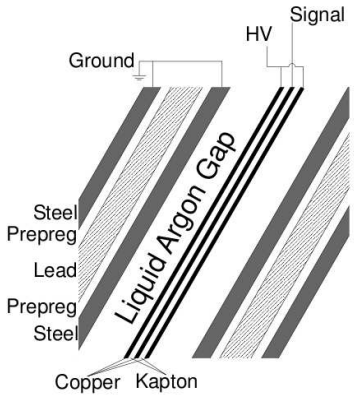

Figure 3.10. Structure of the liquid argon calorimeter electrodes [40].

The hadronic calorimeter is divided into two parts; the tile calorimeter (TileCal) and the LAr hadronic end-cap (HEC) calorimeter.

The tile calorimeter is placed outside the EM calorimeter. Its barrel covers the region with $|\eta| < 1.0$, and its two extended barrels on both sides covers the range $0.8 < |\eta| < 1.7$. It is a sampling calorimeter using steel as the absorber and scintillating tiles as the active material. As illustrated in Figure 3.11, wavelength-shifting fibers placed in contact with the tile edges to collect the scintillation light produced in the scintillators and convert it to a longer wavelength. Each fiber is connected to a photomultiplier tube (PMT) for the detection of the photons created by scintillation.

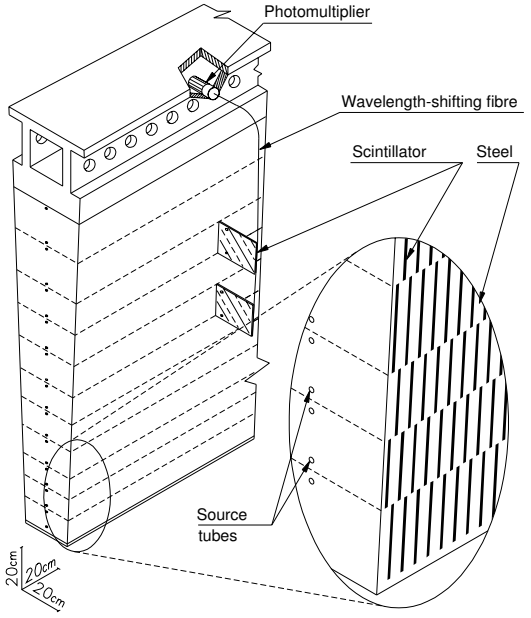

Figure 3.11. Schematic showing how the mechanical assembly and the optical readout of the tile calorimeter are integrated together. [28].

The hadronic end-cap calorimeter (HEC) is a LAr sampling calorimeter use copper as the absorber material and have a planar geometry. It covers the range $1.5 < \eta < 3.2$, slightly overlaps with the TileCal by extending to $|\eta| = 1.5$ and also overlapping with the forward calorimeter by extending out to $|\eta| = 3.2$. It consists of two independent wheels in each end-cap (with plates as electrodes instead of accordion shape), located directly behind the end-cap electromagnetic calorimeter. The wheels are built from copper plates which are interleaved with LAr gaps providing the active medium for this calorimeter. An important aspect of the HEC is its ability to detect muons and to measure any radiative energy loss.

The forward calorimeter (FCal) covers the forward region with $3.1 < |\eta| < 4.9$ and is located in the the end-caps. It consists of three modules in each end-cap. The first module (FCal1) has copper absorbers which is optimised for electromagnetic measurements, while the other two (FCal2 and FCal3) has tungsten absorbers that measure predominantly the energy of hadrons. The arrangement of FCal1 electrodes can be seen in Figure 3.12. The structure of the FCal is a metal (absorber material) matrix with tubes which contain concentrically positioned rods. The LAr is the active

medium which fills the gap between the rod and the tube. A big challenge for this calorimeter is the expected high amount of radiation it has to cope with. Since the FCal front face is at a distance of about 4.7 m from the interaction point and it is located at high η, it is exposed to high particle fluxes, which influenced its design.

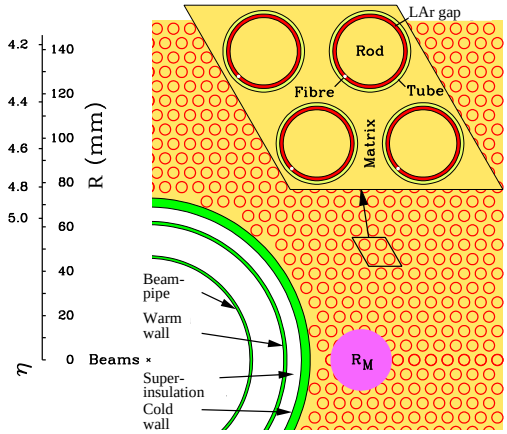

Figure 3.12. Electrode structure of FCal1 with the matrix of copper plates and the copper tubes and rods with the LAr gap for the electrodes. [28].

Calorimeter depth is an important design consideration. Calorimeters must provide good containment for electromagnetic and hadronic showers and must also limit other particles than muons to go into the muon system. The depth in terms of interaction length in front of and in the electromagnetic and hadronic calorimeters are shown in figure 3.13.

3.2.3. Muon spectrometer

The calorimeter system is surrounded by the muon system [41] (figure 3.14), whose role is identification and reconstruction of muon tracks and measurement of their momentum. In p-p collisions, the muons in the final states of various events will have a wide range of momentum. Since muons give a very clean signal for many physics processes under study, to reconstruct them with a high efficiency and resolution was a major design goal for the ATLAS detector. Muons with momenta ranging from a few GeV ($\approx$ 3GeV, due to energy loss in the calorimeter) up to a few TeV ($\approx$3TeV) may be measured by the muon spectrometer (MS) alone. The stand-alone performance goal

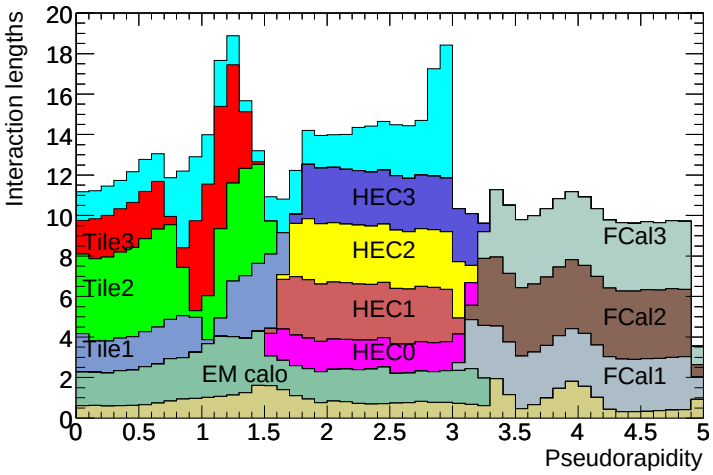

Figure 3.13. Cumulative amount of material, in units of interaction length, as a function of $|\eta|$, in front of and in the electromagnetic calorimeters, in each hadronic compartment, and the total amount at the end of the active calorimetry. Also shown for completeness is the total amount of material in front of the first active layer of the muon spectrometer (up to $|\eta| < 3.0$) [28].

for MS is to measure the transverse momentum with a resolution of approximately 10% for muons with an energy of 1 TeV. It is important to mention that, momentum resolution can be further improved by combining a stand-alone MS track with an inner detector track, which will be discussed in Chapter 3.

The muon system is the outermost and biggest subdetector of ATLAS, determines the overall size of it. It consists of a large air-core toroidal magnet system [34] with a strong bending power and several different chambers for precision measurement and triggering.

The air-core toroid magnet system [42, 43], with a long barrel and two end-caps, generates a magnetic field of about 0.5 T and 1 T for the muon detectors respectively in the barrel region and end-cap regions, and makes momentum measurement indepentent of the inner detector possible. The magnets provide a field which is mostly orthogonal to the muon trajectories.

The precision momentum measurement is performed by the Monitored Drift Tube (MDT) chambers which cover the range $|\eta| < 2.7$ (except the innermost end-cap layer

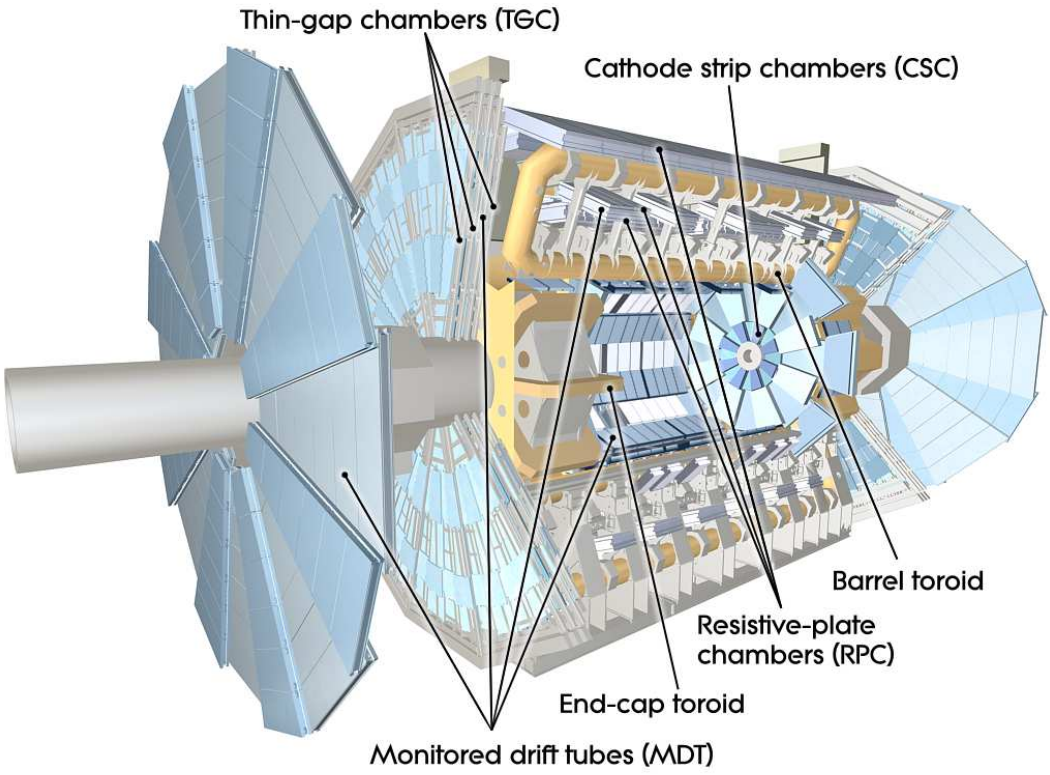

Figure 3.14. Cut-away view of the ATLAS Muon System [28].

with the range $|\eta| < 2.0$). These chambers consist of drift tubes and have a resolution of about 35 μm per chamber in the bending plane. In the innermost tracking layer ($2.0 < |\eta| < 2.7$) Cathode-Strip Chambers (CSC) are used because they are able to cope with the higher counting rates in the end-cap region. These are multiwire proportional chambers with cathode planes. The resolution of this cahmber is 40 μm in the bending plane. The purpose of the precision-tracking chambers is to determine the coordinates of the tracks in the bending plane. The precision-tracking chambers consist of three layers providing the three space-points necessary to be able to reconstruct the trajectory of the muons.

For triggering purposes, Resistive Plate Chambers (RPC) in the barrel region ($|\eta| < 1.05$) and Thin Gap Chambers (TGC) in the end-cap region ($1.05 < |\eta| < 2.4$) over the full ϕ-range are used. RPC is a gaseous parallel electrode-plate detector, whereas TGC consist of multi-wire proportional chambers and they provide high rate capability and time resolution. These fast trigger chambers are capable of delivering track information within a few tens of nanoseconds after the passage of a particle. They have a fast

response but low spatial resolution of several milimeters. The capability to trigger on muon tracks was an essential design criteria of the muon system.

The muon spectrometer has a gap in the center ($|\eta| \approx 0$), which is left open for the services to the solenid magnet, the calorimeters and the inner detector. Also, there are gaps in the regions where the detector support structures (feet) are located. The consequences of the acceptance gaps on tracking efficiency and momentum resolution are discussed in Chapter 3.

3.3. Trigger and data acquisition system

The interactions in the ATLAS detector will create an enormous amount of data. Bunches of up to 10^{11} protons meeting 40 million times per second (40 MHz) at the interaction point will yield a data rate of 64 Tbyte/s. Persistent real-time storage at this rate is not possible with today's technology and with a reasonable budget. Fortunately, it is also not necessary to store all the data produced by the ATLAS detector, since not every event that will emerge from the p-p interactions are interesting for physicists.

The storage technology available at CERN can record data at a rate of 320 Mbyte/s, meaning the maximum rate for storage is about 200 Hz. A sophisticated trigger and data acquisition system (TDAQ) [44] based on three levels of selection process has been developed to choose the rare interesting events and reduce the number of events to be stored from bunch-crossing rate of 40 MHz to a rate of about 200 Hz.

Each trigger level refines the decisions made at the previous level and applies additional event selection criteria. The Level-1 (L1) trigger system is hardware based, which interfaces directly to the detector and runs at the proton-proton bunch crossing rate of 40 MHz. It uses a reduced granularity information from a subset of detectors for making a decision to process an event in less than 2.5 μs and reduces the data rate from 40 MHz down to 100 kHz. The L1 trigger is the only part of the TDAQ that works synchronously with the detector and uses very fast and simple algorithms, where the rest of the TDAQ is implemented in software. The subsequent two levels,

collectively known as the high-level trigger, are the Level-2 (L2) trigger and the event filter (EF). These two high level triggers access more detector information and provide the reduction to a final data-taking rate of up to 200 Hz to be moved to the permanent storage.

3.4. Offline software

3.4.1. ATLAS software framework

The software developed for the ATLAS experiment must be able to deal with the challenging conditions related to the complexity of the experiment. At the same time, it should allow many scientists all around the world working for the experiment to be able to easily run the software, modify the parts of it and analyse the data with it.

Athena [45], software framework of the ATLAS experiment, has been developed to meet these needs. It allows an integrated communication between various software applications within the framework. It also provides a common software developing, by enabling a re-use of already written code-segments and by allowing a user to develop own algorithms and plug into the framework. Athena has adopted an object-oriented development methodology, based primarily on the C++ programming language. Python scripting is used for the configuration of complex C++ programs, i.e., setting the run time parameters of an algorithm via Python job option files.

The main purposes of the ATLAS software is to generate, simulate, digitize and reconstruct events from the proton-proton collisions in the LHC. Monte Carlo (MC) generators are the tools for modelling the complex physics processes that lead to the production of hundreds of particles per event at LHC energies. Generators produce the proton-proton collision and calculate the position and momentum four-vectors of all particles which are produced in the collision. The four-vector information is called MC truth information. The detector response to generated events needs to be simulated to make a realistic estimation of feasibility for future analysis, to compare data with theoretical predictions, or to understand the detector performance in detail. Geant4 [46]

simulation toolkit simulates the detector response to MC events, i.e., the impact of the magnetic field and the interactions of the produced particles with the detector material. After the data objects representing MC truth information are simulated, produced hits can be processed by the digitization algorithm and transformed into Raw Data Objects (RDOs). Digitized data is in the same format with the RAW data, which will be output by the EF (the final stage of the TDAQ) for reconstruction. The reconstruction is based on the digitized information and uses various algorithms, e.g. for pattern recognition, track fitting, vertex determination and energy measurements. The role of reconstruction is to derive the particle parameters necessary for physics analysis from the stored raw data. Information from all detectors is combined so that the momentum reconstruction is optimal for the full momentum and rapidity range, and particles are identified efficiently. The output of the reconstruction is event summary data (ESD) file, which includes a detailed description of an event, and analysis object data (AOD) file, which is derived from ESD and only contains information of physics analysis interest. After production of AOD files and collection of interesting events for analysis, physics analysis tools and various analysis techniques can be used to study physics processes.

3.4.2. LHC distributed computing

Expected huge amount of data ($\approx$ 15 Petabytes/year) that will be produced by the LHC experiments requires new technologies and methods for thousands of scientists around the world to be able to access and analyse it. The LHC Computing Grid Project (LCG) [47] is the new approach to provide a distributed computing infrastructure for the data storage and analysis.

The data distribution follows a hierarchical model, the so-called Tier structure. The raw data emerging from the data acquisition systems will be recorded on tape and initially processed at the Tier-0 centre at CERN. From there, it will be distributed to a series of Tier-1 centres consisting of large computer centres with sufficient storage capacity. The Tier-1 centres will perform the analysis tasks requiring access to large subsets of the raw, processed, and simulated data, and will make the data available to

Tier-2 centres. Tier-2 centres consist of computer clusters, which can store small part of the data and provide adequate computing power for user specific physics analysis and MC simulation. Individual scientists will access these facilities through Tier-3 computing resources, which can consist of local computer clusters in a University Department or individual PCs.

4. MUON IDENTIFICATION AND RECONSTRUCTION IN THE ATLAS DETECTOR

Muon reconstruction and identification is of high importance for the ATLAS experiment due to the production of muons with a wide range of momentum (from a few GeV/c up to a few TeV/c) in the final states of various physics processes that will emerge from p-p collisions at the LHC. The ATLAS detector is efficient for detection of muons and for measurement of their properties such as position, direction and momentum. In order to perform this, software has been devoloped coherently to the hardware design of the detector. This chapter, partly based on the related sections in [28], [48], gives an overview of the muon reconstruction and identification software strategies developed for the ATLAS experiment. The following sections briefly describe the algorithms and summarize the performance studies based on simulated data.

4.1. Muon reconstruction and identification algorithms

Several strategies have been developed for identification and reconstruction of muons. They can be categorized as stand-alone reconstruction, combined reconstruction and segment tag. Stand-alone muon reconstruction is a direct approach, merely based on the muon spectrometer (MS) data; the algorithms employed for this strategy reconstruct muons by finding tracks in the MS and extrapolating them to the beam spot. Combined muon algorithms start with stand-alone muon tracks (i.e., obtained from the MS only) and add inner detector (ID) information. Finally, the segment tag methods combine ID tracks with MS segments. Besides these strategies, calorimeter-based muon identification algorithms have also been developed to tag muons; these algorithms tag the preselected ID tracks by using the energy loss information in the calorimeters.

The current ATLAS baseline reconstruction includes two algorithms for each strategy, which are grouped into two families (Staco [49] and Muid [50]); each family

includes one algorithm for each strategy. The efficiency of finding muons may increase, if the muons found by the algorithms based on the different strategies or the muons from different families are merged. However, one must take care of the case when the same muon is identified by two or more algorithms.

4.1.1. Stand-alone algorithms

The stand-alone algorithms first build track segments in each of the three muon stations and then link these segments to form tracks. These tracks are extrapolated to the beam spot to account for multiple scattering and energy loss in the calorimeter. The pseudorapidity coverage of the stand-alone algorithms is, $|\eta| < 2.7$, defined by the MS acceptance. It is slightly greater compared to the ID coverage $|\eta| < 2.5$, however, this little coverage gain in the forward regions does not bring a noteworthy advantage. Muons with high momentum typically traverse all the MS stations. However, there are regions with support structures or passages for services, where one, two or all three stations do not provide measurements. The muon momentum resolution and reconstruction efficiency degrade at those regions. Furthermore, very low momentum muons (a few GeV/c) may be difficult to reconstruct stand-alone because they do not reach the outer stations. Therefore, other strategies are developed to improve muon identification and reconstruction where the stand-alone procedure is inefficient.

4.1.2. Combined algorithms

The ID detects muons and other charged particles with pseudorapidity coverage of $|\eta| < 2.5$ and provides an important confirmation of muons found by the MS over that η range. Also, by means of 2 Tesla magnetic field, it is able to provide an independent precise momentum measurement of muons (and other charged particles). Over the pseudorapidity range of $|\eta| < 2.5$, for p_T roughly between 30 and 200 GeV/c, the momentum measurements from the ID and MS may be combined to give a better momentum resolution than either system alone. Combined muon reconstruction algorithms find the muons by matching the MS tracks with the ID tracks and then combine the measurements from the two systems. During this matching, they calculate a match

chi-square (χ^2_{match}), which provides an important measure of the quality of matching. The χ^2_{match} is defined as the difference between outer and inner track-parameter vectors weighted by their combined covariance matrix:

$$\chi^2_{match} = (\mathbf{T_{MS}} - \mathbf{T_{ID}})^{\mathrm{T}} (\mathbf{C_{ID}} + \mathbf{C_{MS}})^{-\mathbf{1}} (\mathbf{T_{MS}} - \mathbf{T_{ID}}) \tag{4.1}$$

Here $\mathbf{T}$ denotes a vector of five track parameters, expressed at the point of closest approach to the beam line, and $\mathbf{C}$ is its covariance matrix.

In order to achieve a high performance for combined muon reconstruction, it is important that the ID and the MS are calibrated and aligned internally and with respect to each other.

4.1.3. Segment tag algorithms

The segment tagging algorithms, extrapolate the ID tracks with sufficient momentum to the first station of the MS and search for nearby segments. There are two algorithms (MuTag [49] and MuGirl [51]) developed for this purpose and they apply different methods; however, in either case, if a segment is sufficiently close to the predicted track position, then the ID track is tagged as a muon. These algorithms simply use the ID track to evaluate the muon kinematics.

Muons with momenta below typically 6 GeV are difficult to reconstruct with either stand-alone or combined reconstruction because they do not always reach the middle and outer muon stations. Therefore, segment tag algorithms provide an important improvement to the stand-alone muon reconstruction for low-p_T muons. Their contribution is also important in regions (especially $1.1 < |\eta| < 1.3$) where some of the muon stations are missing and reconstruction efficiency degrades accordingly.

4.2. Performance

The performace of the muon reconstruction and identification algorithms that implement the three strategies described in the previous section is discussed here. Results are based on full simulation and reconstruction, and have been obtained using the algorithms of the Staco-family. Fractional momentum resolution and reconstruction efficiency are used as performance measures; fractional momentum resolution, $\Delta p_T/p_T$, is defined as in equation 4.2 and reconstruction efficiency, $R.E$, is defined in equation 4.3, where true particle type and true transverse momenta are those in the Monte Carlo truth record. $1/p_T$ is used instead of p_T in the calculation of momentum resolution, since muons momenta are measured from the curvature of the their trajectories, which is related with $1/p_T$.

$$\frac{\Delta p_T}{p_T} = \frac{1/p_{T\text{reco}} - 1/p_{T\text{true}}}{1/p_{T\text{true}}} = \frac{p_{T\text{true}} - p_{T\text{reco}}}{p_{T\text{reco}}} \tag{4.2}$$

$$R.E = \frac{\#\text{ of reconstructed muons matched with a true muon}}{\#\text{ of true muons}} \tag{4.3}$$

Figures 4.1 and 4.2 show the expected fractional momentum resolution on single muons respectively as a function of $|\eta|$ and ϕ, the latter is only in the region $0.3 < |\eta| < 0.65$, for stand-alone and combined muon tracks with $p_T = 100$ GeV/c. In Figures 4.3 and 4.4, the efficiency for reconstructing single muons is shown, respectively as a function of $|\eta|$ for muons with $p_T = 100$ GeV/c and as a function of p_T, where the results are shown for stand-alone reconstruction, for combined reconstruction and for the combination of these with the segment tags. It can be clearly seen from the figures that the muon momentum resolution and the reconstruction efficiency degrade in certain regions. This degradation is due to several reasons arising from hardware-related inefficiencies, which can be listed as the following:

- In the region with $|\eta| < 0.1$ there are very few muon stations due to the large gap for services. Therefore the reconstruction efficiency drops to very low values in this region (see Figure 4.3).
- In the region with $1.1 < |\eta| < 1.7$ there is a large degradation of the stand-alone momentum resolution due to several effects; in the region $1.1 < |\eta| < 1.3$, the middle muon stations are missing in the barrel/end-cap transition region, hence, the measurement is limited to an angle-angle measurement between inner and outer stations, at larger values of $|\eta|$, the magnetic field in the transition region between the barrel and end-cap toroids has low bending power and there is a large amount of material in the coils of the end-cap toroid in limited regions in $|\phi|$. Due to the large degradation of the stand-alone momentum resolution, the contribution of the combined reconstruction is more important in this η region (see Figure 4.1). Moreover, stand-alone reconstruction efficiency is significantly reduced in the $1.1 < |\eta| < 1.3$ region due to the absence of the middle muon stations. The segment tag procedure provides an important improvement to the muon reconstruction in this region (see Figure 4.3).
- In the region with $|\eta| = 0.2$, 0.3 and 0.7, there are support structures of the barrel toroid magnet coils. The degradation of stand-alone momentum resolution in these $|\eta|$ regions can be seen in Figure 4.1.
- The feet that support the experiment are located close to $\phi = 240\,^\circ$ and $300\,^\circ$. The resolution degrades in these regions, due to the additional material introduced by the feet which support the barrel part of the detector (see Figure 4.2).

The number of stations muons pass through in the MS as a function of $|\eta|$ and ϕ is shown in Figure 4.5. It can be seen from this figure that the number of stations is less than the nominal three in the restricted $|\eta|$ - ϕ regions that are mentioned above.

In Figure 4.6 the calculation of stand-alone momentum resolution as a function of ϕ for muons with $p_T = 100$ GeV/c is shown. This calculation is based on a parametrisation using the spatial resolution of the muon chambers, the material distribution and the magnetic-field configuration in the MS [41]. The results based on simulation shown in Figures 4.1, 4.2 are consistent with the result of this analytical model.

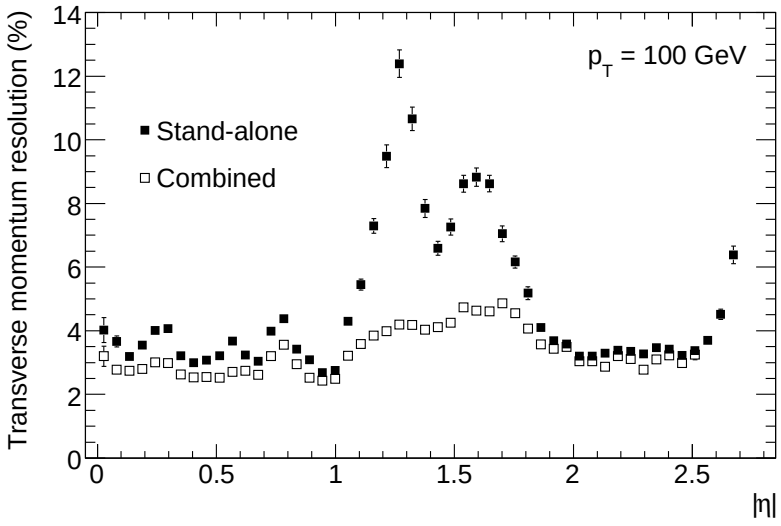

Figure 4.1. For muons with p_T =100 GeV/c, expected fractional momentum resolution as a function of $|\eta|$ for stand-alone and combined reconstruction [28].

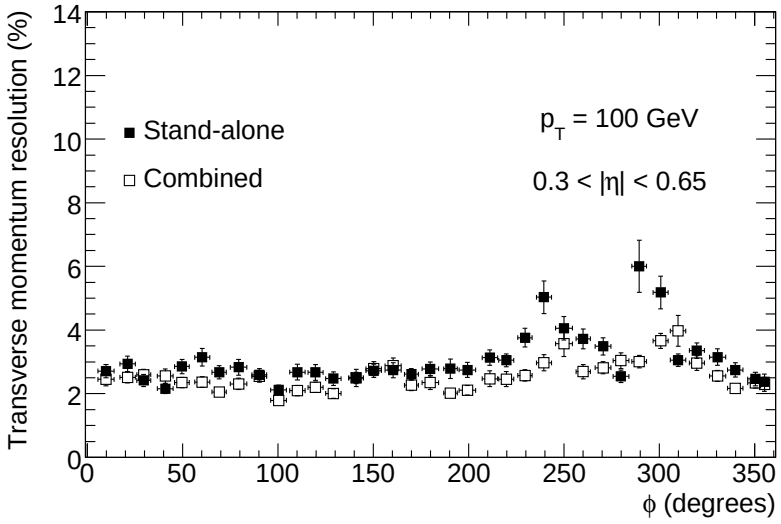

Figure 4.2. For muons with p_T = 100 GeV/c, expected fractional momentum resolution as a function of ϕ for stand-alone and combined reconstruction [28].

Finally, Figure 4.7 shows the four-muon invariant mass distributions from stand-alone and combined reconstruction for $H \rightarrow 4\mu$ decays in the case of a Higgs boson mass of 130 GeV. The stand-alone resolution is 3.3 GeV, whereas the combined resolution is 2.1 GeV. The worse stand-alone resolution is mainly due to muons measured in the inefficient regions of the muon spectrometer that are mentioned above.

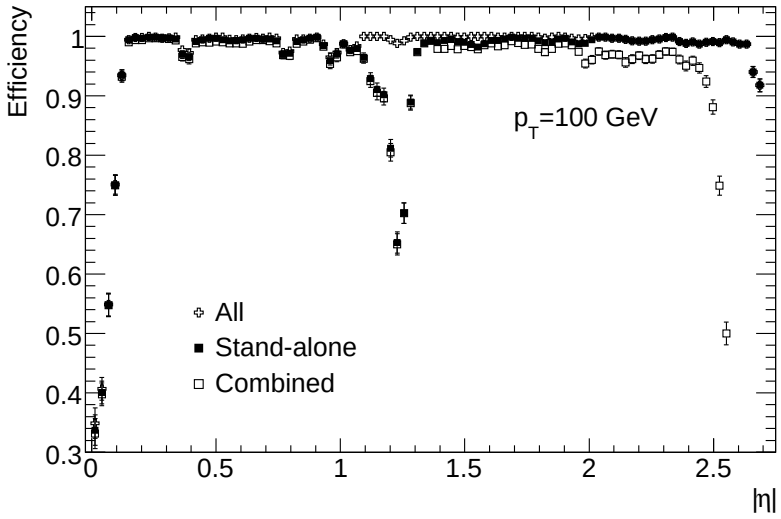

Figure 4.3. Efficiency for reconstructing muons with $p_T = 100$ GeV/c as a function of $|\eta|$. The results are shown for stand-alone reconstruction, combined reconstruction and for the combination of these with the segment tags [28].

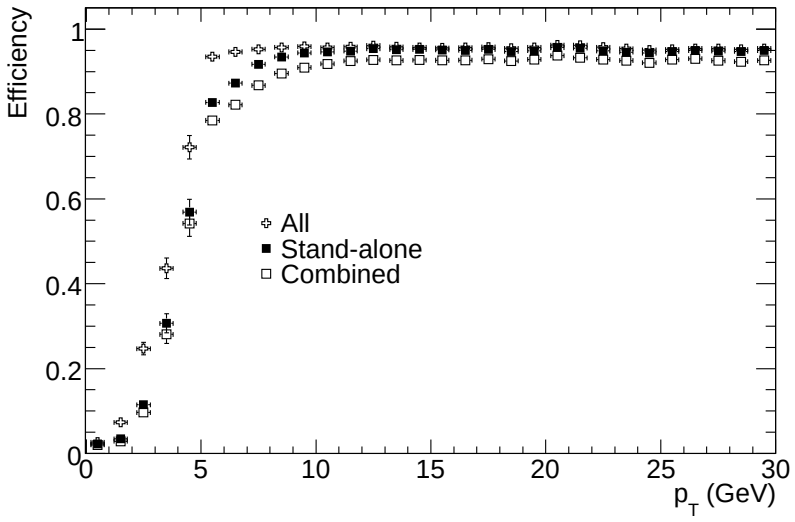

Figure 4.4. Efficiency for reconstructing muons as a function of p_T. The results are shown for stand-alone reconstruction, combined reconstruction and for the combination of these with the segment tags [28].

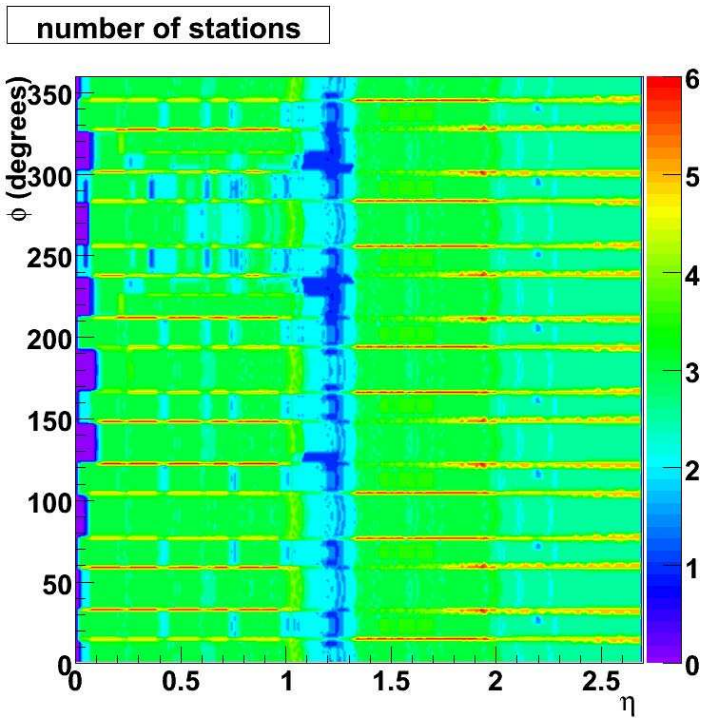

Figure 4.5. Number of detector stations traversed by muons passing through the Muon Spectrometer as a function of $|\eta|$ and ϕ [48].

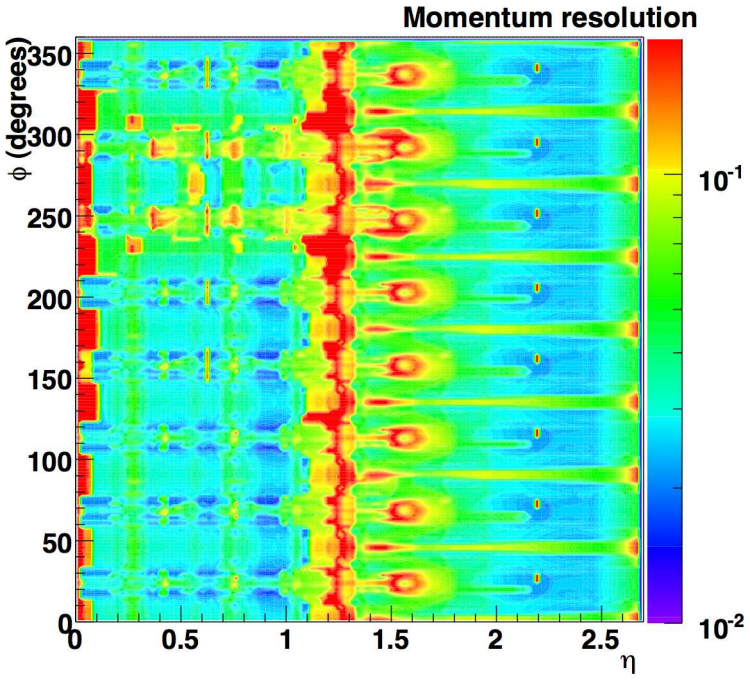

Figure 4.6. For muons with $p_T = 100$ GeV/c, expected fractional stand-alone momentum resolution as a function of ϕ and $|\eta|$ [28].

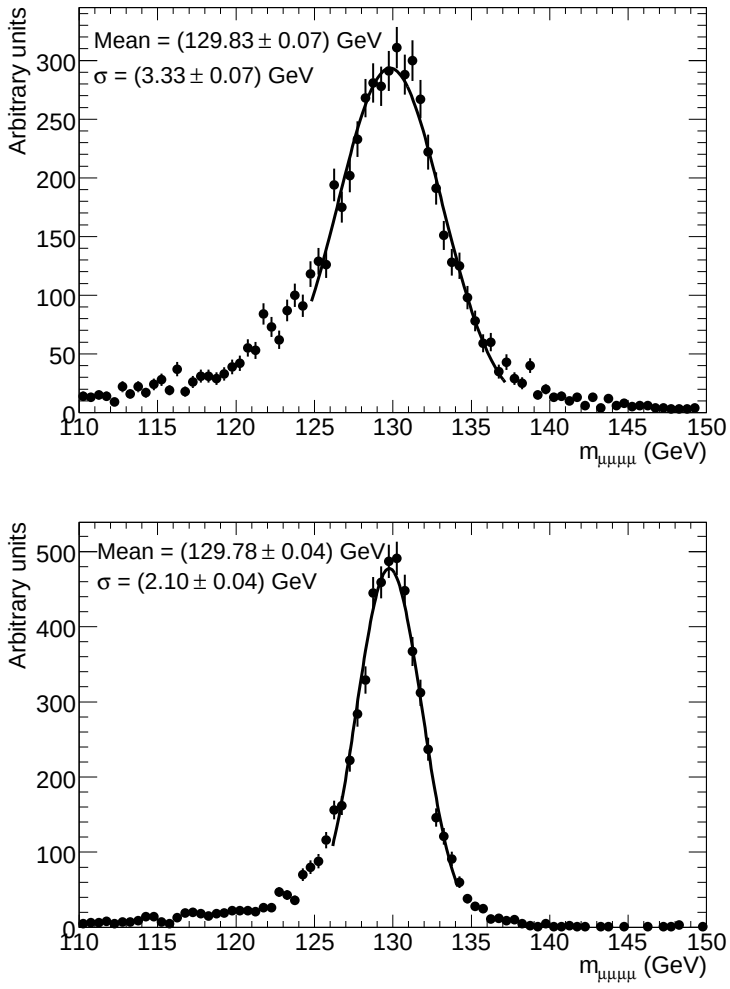

Figure 4.7. For $H \to 4\mu$ decays with $m_H = 130$ GeV, reconstructed mass of the four muons using stand-alone reconstruction (top plot) and combined reconstruction (bottom plot) [28].

5. CALORIMETER-BASED MUON IDENTIFICATION

Muons with momenta ranging from approximately 3 GeV/c to 3 TeV/c will be identified and reconstructed with an optimum efficiency by using stand-alone MS tracks, combined MS and ID tracks and tagged ID tracks matched with MS segments [28]. Usage of these different strategies optimizes the geometrical acceptance and improves the momentum resolution and reconstruction efficiency. Segment tagging algorithms contribute substantially to the identification of low-p_T muons (see Figure 4.4) and they manage to recover the muons in the low-acceptance regions of MS, especially in $1.1 < |\eta| < 1.3$ region (see Figure 4.3), where middle muon stations are missing. However, in $\eta \approx 0$ region, where there are very few muon stations due to the large gap for services, the reconstruction efficiency is still very low due to the fact that all the three strategies make use of MS hits for muon identification. Calorimeter-based muon identification, which is a way of identifying muons independent of MS information, can recover the muons in these low-acceptance regions of the MS, especially in the $\eta \approx 0$ region. Moreover, muons with very low transverse momentum (p_T = 2-5 GeV/c) that may not reach some or all of the MS stations can also be identified by the energy loss measurements in the calorimeter system.

As muons pass through the ATLAS detector, they traverse over 100 radiation lengths [6] (X_0) of material before they reach the MS (see Figure 5.1) [52]. During this passage, they lose part of their energy in the calorimeters through electromagnetic processes. When relativistic muons go through matter they lose energy mostly through ionization and radiative processes; e^+e^- pair-production and bremsstrahlung. Ionization energy loss dominates for muons of momenta $\lesssim$ 100 GeV, and for muons with higher momenta (critical energy occurs at several hundred GeV), radiative processes become more important (see Figure 5.2).

[6] High-energy electrons predominantly lose energy in matter by bremsstrahlung, and high-energy photons by e^+e^- pair production. The characteristic amount of matter traversed for these related interactions is called the radiation length X_0, usually measured in $g\ cm^2$. It is both (a) the mean distance over which a high-energy electron loses all but 1/e of its energy by bremsstrahlung, and (b) 7/9 of the mean free path for pair production by a high-energy photon[9].

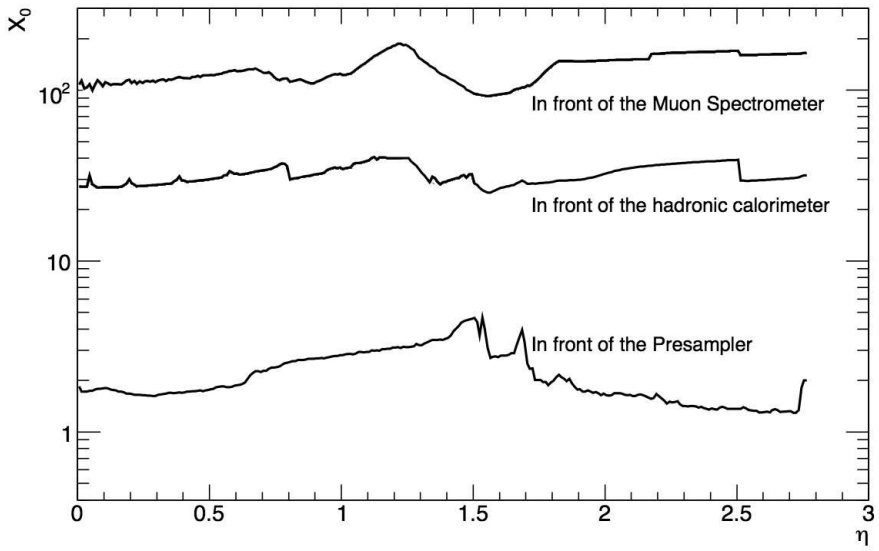

Figure 5.1. Material distribution before the muon spectrometer in ATLAS as a function of η. The material is expressed in radiation lengths (X_0) [52].

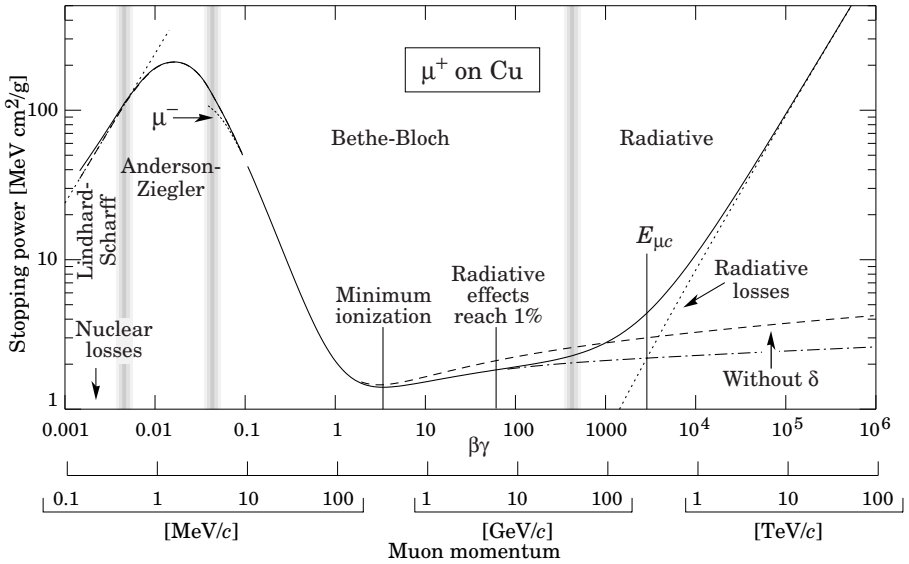

Figure 5.2. Stopping power (-dE/dx) for positive muons in copper as a function of $\beta\gamma$ = p/M c over nine orders of magnitude in momentum. Solid curves indicate the total stopping power [9].

Calorimeter-based muon identification algorithms make use of the energy loss of muons, calculated from parameterizations and/or measurements in the calorimeters, for identification due to the characteristic minimum ionizing signature of muons.

In the following sections, the alogrithms developed for muon identification in the calorimeters will be briefly addressed. One of them will be described in detail and improvements to it carried out within the scope of this thesis will be explained. Its performance will be illustrated on different single muon and physics MC samples before and after the improvements, and studies concerning the application of the algorithm to the $H \rightarrow ZZ^{(*)} \rightarrow 4\ell$ channel will be shown. Finally, possible extensions that would be interesting to implement in the algorithm will be discussed.

5.1. Algorithms

Calorimeter-based muon identification algorithms developed for the ATLAS Experiment can be categorized in two types; calorimeter-seed and track-seed, depending on how they initiate the search for muons.

Calorimeter-seed algorithms start the muon search by looking at the measured energy in the calorimeter. Their seeds are the calorimeter cells with energy depositions inside some energy range with a lower threshold. The cluster from cells is then built by adding cells around the seed cell whose energy is above a second lower threshold. This cluster is used to identify muons. At the end of the clustering, the η and ϕ directions of the reconstructed cluster can be used to match an ID track. The algorithms of this type are used for commissioning or triggering purposes. Calorimeter-seed algorithms are not discussed any further in this work; however, detailed description of the algorithms of this type and their performance can be found in [48, 53, 54].

Track-seed algorithms use the preselected ID tracks as seeds. They extrapolate them through the calorimeter layers, collect the deposited energies and identify those matching the energy deposition pattern of a muon. They are based on the idea of using the distinct energy deposition characteristics of muons. They don't use any information from the MS. There are two algorithms of this type; $CaloMuonLikelihoodTool$ and $CaloMuonTag$, currently part of the standard reconstruction (they will be referred to as $CaloLR$ and $CaloMT$, respectively, in the rest of the thesis). Both algorithms are

implemented in the same package, called $CaloTrkMuId$, in Athena.

The $CaloMT$ algorithm gives different tags to the muon candidates by using hadronic calorimeter deposits. It extrapolates the ID tracks through the calorimeter samplings and collects the energy in the cell closest to the extrapolated track for each traversed sampling. It rejects the tracks if any of the collected energies are above veto values defined for each sampling, where these veto values can be set different for low-p_T and high-p_T tracks for optimization. Once calorimeter cells along the muon trajectory have been identified, the algorithm determines the lower threshold energy cut that should be used for the tagging as a function of η:

$$E_{\text{th}} = \frac{E_0^{\text{barrel}}}{\sin^2\theta} \tag{5.1}$$

$$E_{\text{th}} = \frac{E_0^{\text{end-cap}}}{(1-\sin\theta)^2} \tag{5.2}$$

Equation 5.1 is for tracks with $|\eta| < 1.7$ and equation 5.2 is for the ones with $|\eta| > 1.7$. The values of E_{th} from these two equations roughly follow the shape of the measured energy distributions, which increases with the path length of the muon in the cell. If the energy deposited in the last sampling, or one of the two previous samplings depending on the η of the track, is above the threshold cut, E_{th}, the track is tagged as a muon. A different tag is given depending on the sampling in which the above check is successful [48].

The $CaloLR$ algorithm builds a likelihood ratio to discriminate muons from pions. The likelihood discriminant is built out of several energy ratio variables characterizing the pattern of muon energy depositions in the calorimeters. This algorithm will be decribed in detail in the following sections.

5.2. Track preselection for $CaloLR$ and $CaloMT$

Both track-seed algorithms use the ID tracks as seed after a common track preselection procedure. Track preselection reduces the time needed by the algorithms to

run on events with a large number of tracks. Moreover, it is needed mainly to reduce the number of misidentified tracks by the algorithms, where these fakes mostly come from tracks with low-p_T or muons that are not isolated.
The following preselection cuts are applied on the tracks:

- $p_T > 2$ GeV/c and $E_T^{\text{iso}} < 10$ GeV for tracks pointing to the barrel.
- $p_T > 3$ GeV/c and $E_T^{\text{iso}} < 8$ GeV for tracks pointing to the end-cap.
- $E_T^{\text{iso}} < p_T$ and $P_T^{\text{iso}} < p_T$ for tracks with $p_T < 10$ GeV/c.

A different cut is applied on the transverse isolation energy, E_T^{iso}, of the tracks inside a cone of $\Delta R = 0.45$ depending on their η, where $\Delta R = \sqrt{\Delta\eta^2 + \Delta\phi^2}$ is the distance in pseudorapidity-azimuthal angle space. Transverse isolation energy is defined as the sum of the transverse energy deposited in the calorimeter inside a cone of a given radius ΔR_{out} (outer radius) around the muon, minus the energy deposition of the muon in a cone of radius ΔR_{in} (inner radius); Figure 5.3 illustrates the cones around the muon trajectory. Muons assumed to deposit their energy inside the cone with radius ΔR_{in}, where the size of this inner radius can be optimized to collect most of the energy lost by the muon but as little energy as possible from other particles. For the track-seed algorithms an inner radius of 0.05 is used as default. The energy deposited in the annulus between the cones with radii ΔR_{in} and ΔR_{out}, is called the calorimeter-based isolation energy. Similar to the calorimeter-based isolation energy, track-based isolation energy, P_T^{iso}, is defined as the sum of the transverse momenta of inner detector tracks in a cone of a given radius ΔR_{out} around the muon, minus the transverse momenta of muon tracks in a cone of radius ΔR_{in}. Track- and Calo- based isolation criteria are not strictly independent, but they do use independent measurements of activity around a given track; as a result, their joint use can better reject non-isolated tracks than either criterion on its own. Calorimeter-based isolation criterion aims to reject non-isolated muons which cause a large number of fakes of the algorithms. Muons are called to be non-isolated when they enter the calorimeters not alone but together with other particles that deposit energy in the cells around their tracks. This contamination makes the muon energy loss measurements unreliable. Muons coming from semileptonic b and c quark decays lie within jets and thus are non-isolated, wehereas muons coming

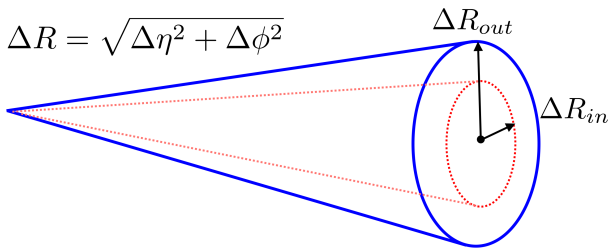

Figure 5.3. A representation of cones around a muon candidate.

from W and Z boson decays are isolated. A calorimeter measurement of the energy loss only makes sense if the muon is isolated, hence, the transverse isolation energy (E_T^{iso}) criterion is used for choosing isolated muon candidates. In addition, as most fakes are coming from low-p_T tracks, for tracks with $p_T < 10$ GeV/c calorimeter-based and track-based isolation criteria are used to reject non-isolated low-p_T muons.

Figure 5.4 shows an example of a study on the calorimeter-based isolation criterion for muons on a fully simulated $t\bar{t} \rightarrow W^+bW^-\bar{b} \rightarrow 4\ell$ sample, where the W bosons were forced to decay into a muon and a neutrino. Distributions of the isolation energy for muons originating from quarks and W bosons are shown for the electromagnetic (top plot) and hadronic (bottom plot) calorimeters. In this example the isolation energy inner and outer radii are 0.075 (0.15) and 0.15 (0.30) for the electromagnetic (hadronic) calorimeters, respectively [48].

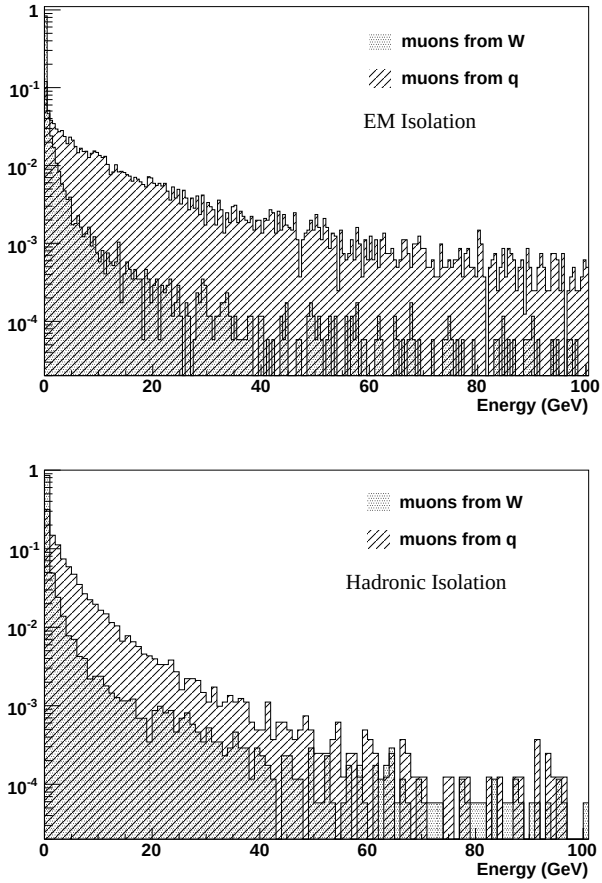

Figure 5.4. Distribution of the isolation energy in the electromagnetic ($0.075 < \Delta R < 0.15$) (top plot) and hadronic calorimeters ($0.15 < \Delta R < 0.30$) (bottom plot) for muons from a $t\bar{t}$ sample without pile-up [48].

5.3. Calorimeter-based Likelihood Ratio algorithm: *CaloLR*

The *CaloLR* muon tagging algorithm is based on the idea of using the distinct properties of muon energy depositions in the calorimeters, as compared to those of other paticles. In order to tag muons, the algorithm constructs a likelihood ratio which peaks at 1 for muons and 0 for pions and other particles. Distributions of several variables based on the energy depositions in the calorimeter samples are used to construct the likelihood ratio. Since it is advantageous to reduce the dependence on calorimeter calibration constants, instead of energies left in the calorimeter samples, ratios of these energies are used as variables. Besides, it brings the additional advantage of defining all the distributions in the interval (0,1).

Normalized distributions of these energy ratio variables are obtained with fully simulated single muon and single pion samples [7] and used as the probability density function (PDF) for that variable. After investigating many of the energy ratio variables, the ones with optimum discrimination power are selected.
Some of these variables, like;

E_{eemb1}/E_{EM+Had} **:** Energy in the first sampling of electromagnetic barrel as a fraction of the total cluster energy.

E_{eeme1}/E_{EM} **:** Energy in the first sampling of electromagnetic endcap as a fraction of the total electromagnetic energy on the cluster.

E_{ehec0}/E_{EM+Had} **:** Energy in the presampling of hadronic endcap as a fraction of the total energy on the cluster.

$E_{etileb2}/E_{Had}$ **:** Energy in the second sampling of tile barrel as a fraction of the total hadronic energy on the cluster.

are the energy fractions deposited in samplings of the electromagnetic and hadronic calorimeters. And other variables like;

E_{EM}/E_{EM+Had} **:** Energy in the electromagnetic samplings as a fraction of the total cluster energy.

E_{EM+Had}/E_{trk} **:** Total cluster energy as a fraction of the (true) energy of the matching track.

E_{mxHad}/E_{Had} **:** Largest hadronic sampling as a fraction of the total hadronic energy on the cluster.

E_{mxSamp}/E_{EM+Had} **:** Largest energy sampling as a fraction of total cluster energy.

capture the global features of the set of depositions in the cluster.

[7] Single muon and single pion samples were obtained using the ATLAS full simulation (in release 11.0.4), generated at the expected interaction point and shot in all directions in the ATLAS detector, wtih energies ranging from 4-500 GeV

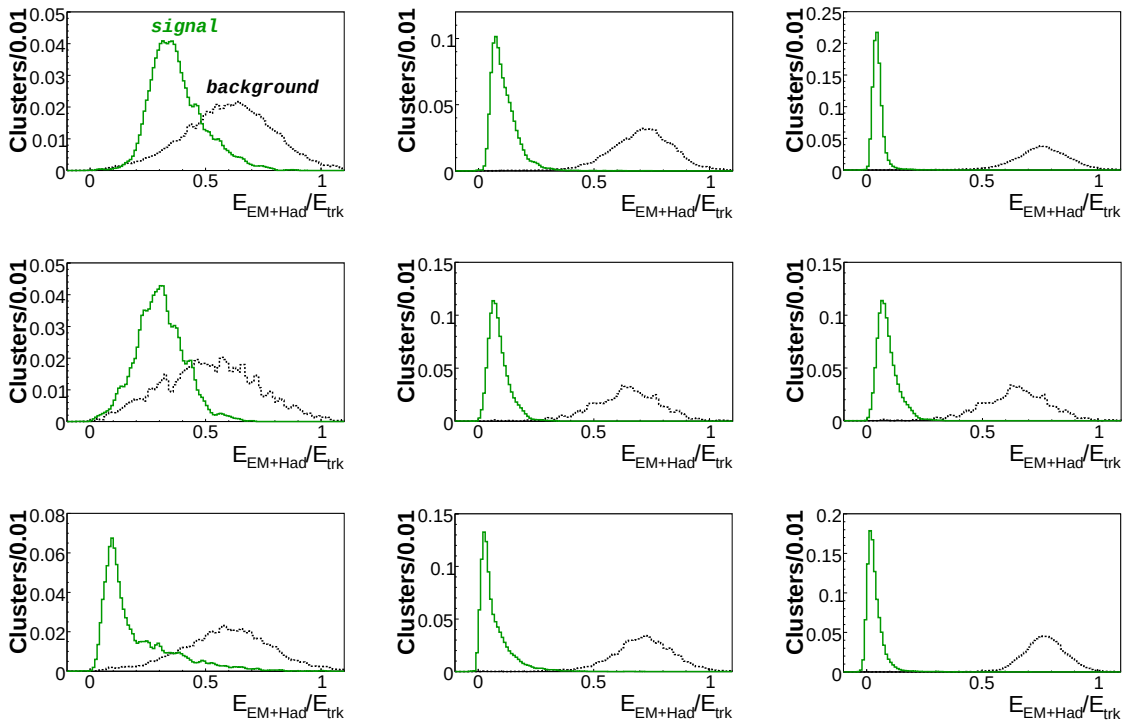

Figure 5.5. Distributions of E_{EM+Had}/E_{trk} variable for muons (solid green line) and for pions (dashed black line) in the nine regions considered. Low, Medium, High Energy Bin (left to right) & Barrel, Crack, Endcap η Bin (top to bottom)

The discrimination power of these variables varies with energy and pseudorapidity of the particles considered. To take this dependence into consideration, three bins in energy: low (E_{truth} <11 GeV), medium (10 GeV< E_{truth} <51 GeV), high (E_{truth} >50 GeV) and three bins in pseudorapidity: barrel ($0 < \eta < 1.4$), crack ($1.4 <= \eta <= 1.6$), endcap ($1.6 < \eta < 2.5$) are defined and a different set of variables is investigated and selected for each of these nine regions. Figure 5.5 shows the distributions (in dashed black for pions and in solid green for muons) for E_{EM+Had}/E_{trk} variable in each region. It can be clearly seen from this figure that discrimination power decreases for the low energy bins. As a result, other variables than E_{EM+Had}/E_{trk} are used for low energy bin due to this decrease. Figures 5.6, 5.7 and 5.8 show the distributions of other variables selected for low energy barrel, crack and endcap regions respectively.

For each muon candidate, the algorithm computes the energy ratio variables selected for that energy-pseudorapidity region, gets the probability of being a muon

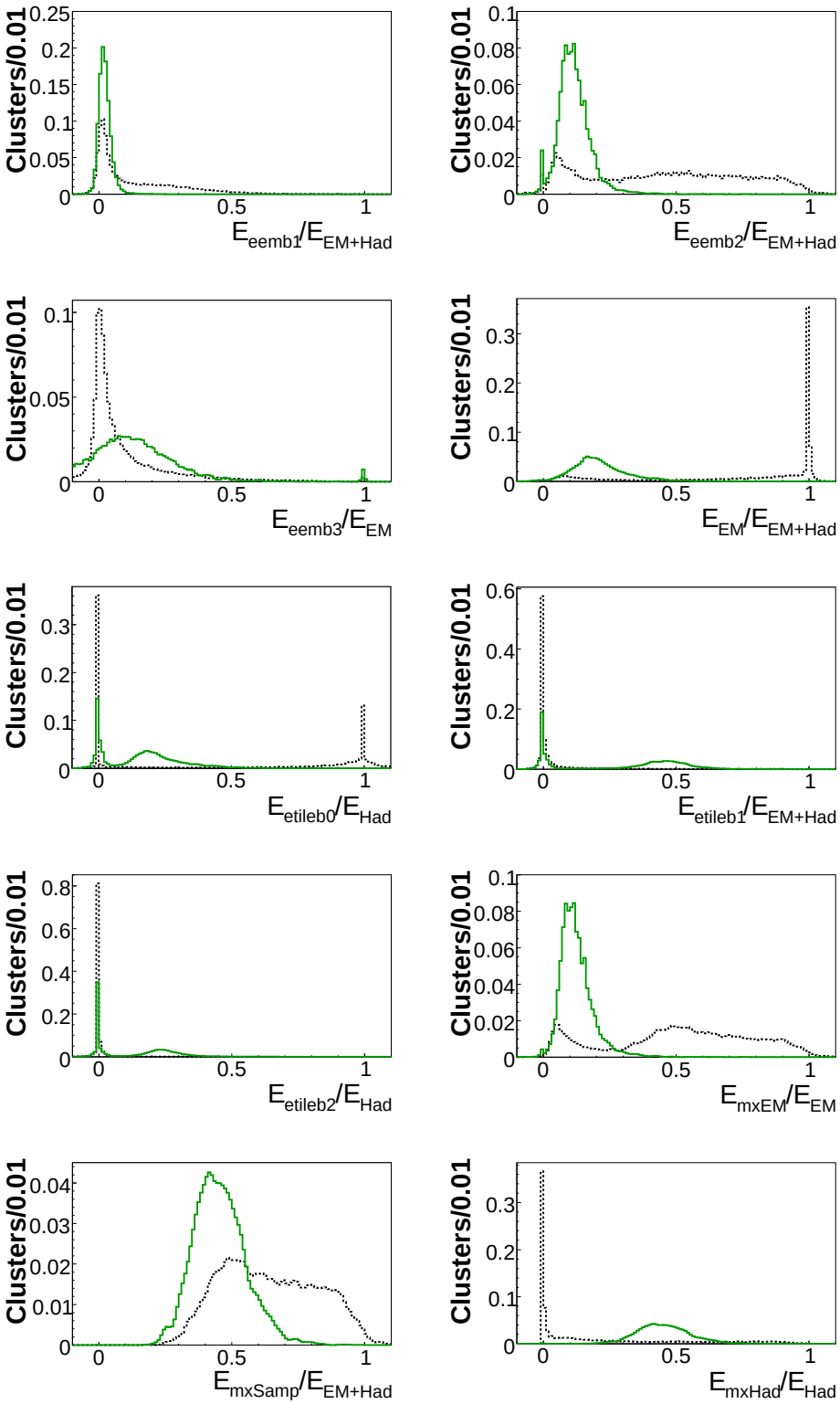

Figure 5.6. Distributions of other variables used for low energy and barrel region. Dashed black line: single pions; solid green line: single muons.

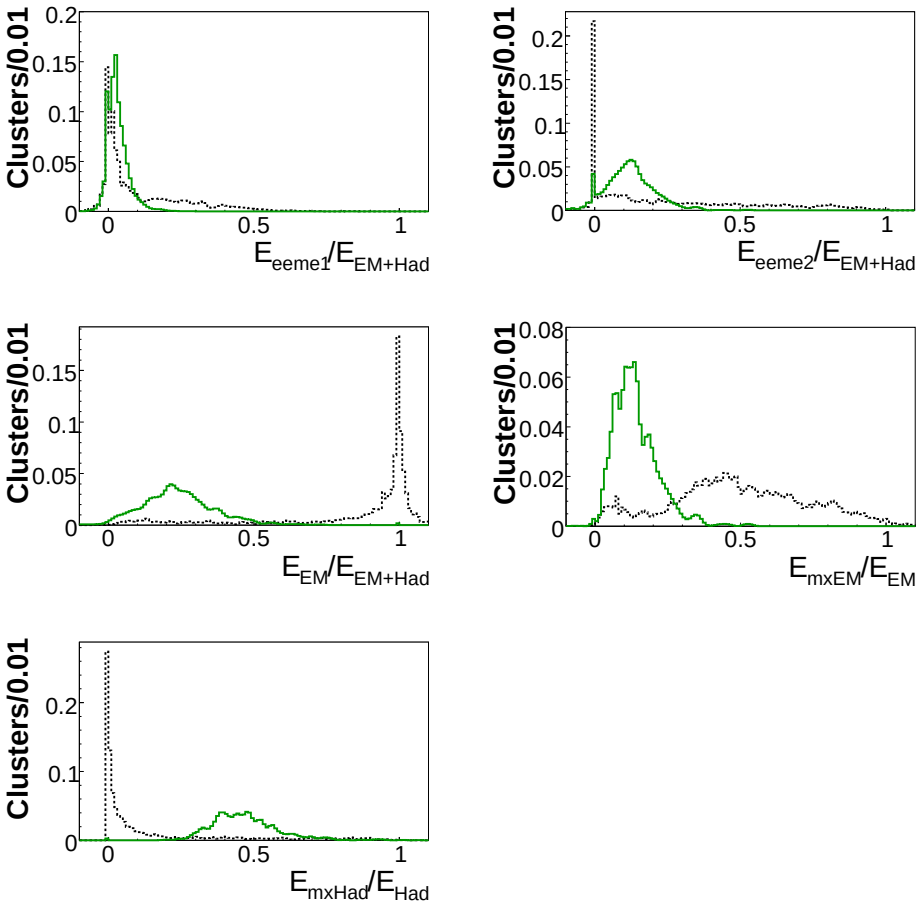

Figure 5.7. Distributions of other variables used for low energy and crack region. Dashed black line: single pions; solid green line: single muons.

and a pion from the corresponding PDF distributions and calculates a likelihood ratio defined as

$$\mathcal{L}(x_1, ..., x_N) = \prod_{i=1}^{N} \frac{P_i^{\mu}(x_i)}{P_i^{\mu}(x_i) + P_i^{\pi}(x_i)} \tag{5.3}$$

Where P_i^{μ} and P_i^{π}, $i = 1, ..., N$ are the PDF for energy ratio i for muons and pions, respectively, and x_i is the energy ratio i for the muon candidate under consideration. By construction the likelihood ratio peaks at 1 for muons and at 0 for pions and other particles. A likelihood ratio cut of 0.5 is being used as a default; however, different cuts can be chosen depending on the physics process under study.

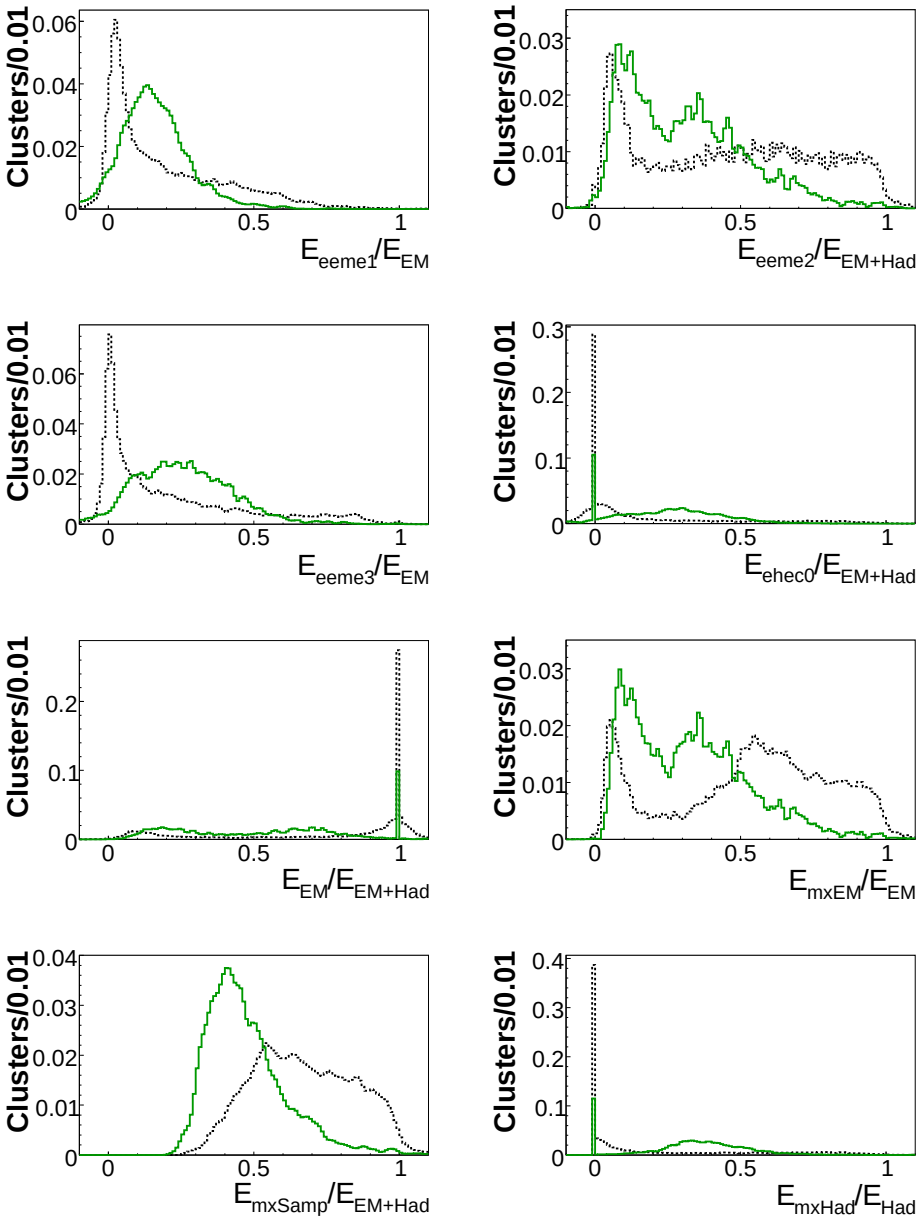

Figure 5.8. Distributions of other variables used for low energy and endcap region. Dashed black line: single pions; solid green line: single muons.

5.4. Improvements for *CaloLR* algorithm

The *CaloLR* algorithm was first developed as a stand-alone program and shown to be an effective method for tagging muons by using the calorimeter information, however, it showed a lower performance than expected after it was ported into Athena, in release 13. Some changes to *CaloLR* have improved its performance from release

13 to 14. The performance improvement was mainly due to the treatment of zero content bins in the PDF distributions that are used to build the likelihood ratio. In the case of an empty bin in either a signal or a background distribution, the Athena implementation of the algorithm used to assign a default value 1 to the probability variable, instead of 0. This led to the problem of tagging muons as pions and vice versa. After modifying this behavior, the performance of the algorithm improved significantly. Figure 5.9 shows the likelihood ratio distribution (top histograms) and the efficiency (bottom histograms) of the algorithm on a simulated sigle muon sample with fixed momentum of 100 GeV/c, before (left plots) and after (right plots) the modification. It can be seen from the plots that, before, there were many true muons with LR less than 0.5 and which resulted in a poor efficiency, and after the fix muons are tagged correctly and the efficiency improved considerably. Furthermore, empty bin content in both signal and background distributions resulted in a likelihood ratio of 0.5 which was not discriminative, and decreased the efficiency of the algorithm as well.

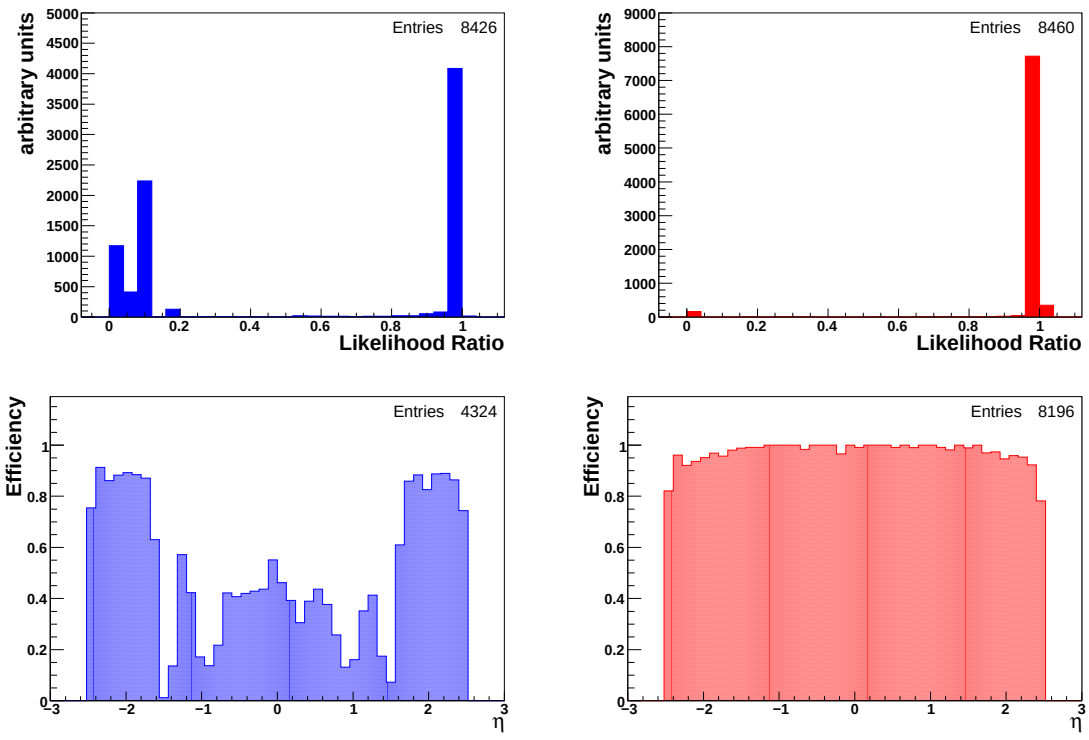

Figure 5.9. Likelihood ratio (top histograms) and efficiency (bottom histograms) for a sigle muon sample with fixed momentum of 100 GeV/c, before (left plots) and after (right plots) the modification of the PDF distributions.

The inefficiency of having empty content bins, which was also present in the stand-alone version of the algorithm, was fixed by smoothing the discrete distributions by using a moving average smoothing algorithm described in [55]. Some examples of its effect on the relevant PDF distributions can be seen in Figures 5.10 and 5.11 for pions and muons, respectively.

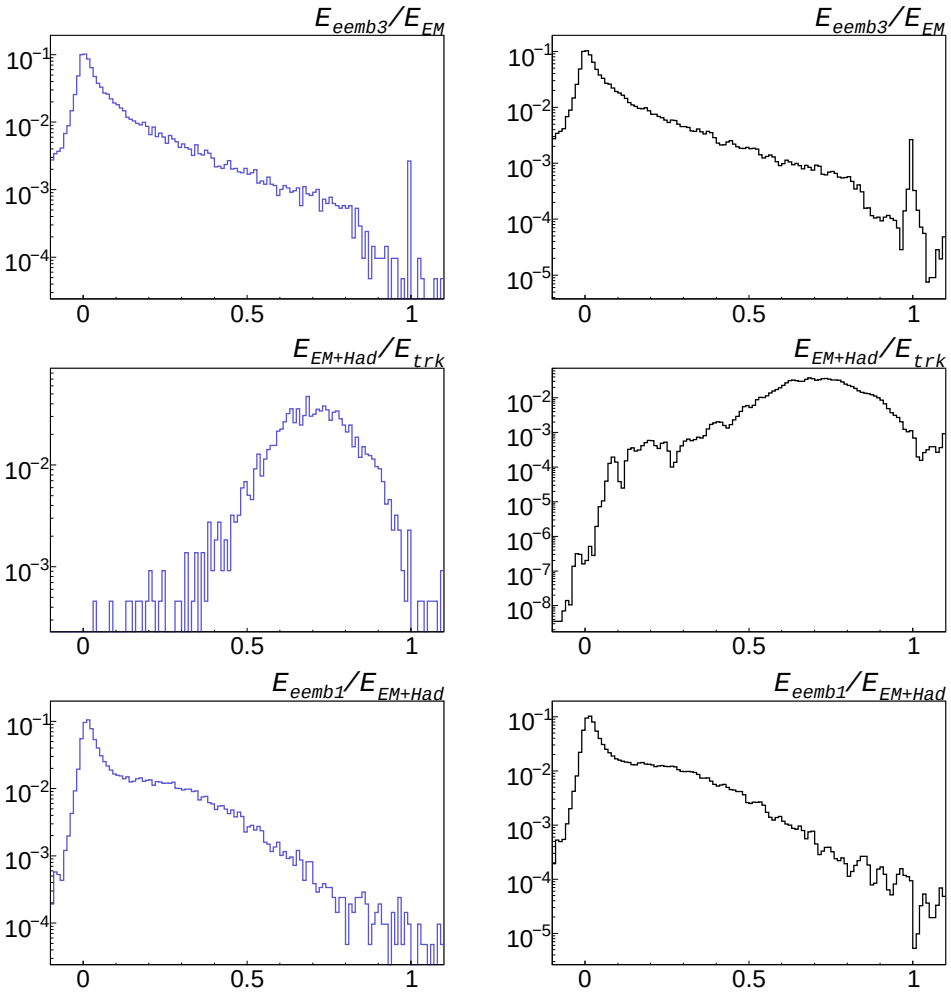

Figure 5.10. Background PDF distributions for several variables before (left) and after (right) the Smooth method is applied.

After the changes mentioned above the algorithm not only recovered the performance of the stand-alone version (i.e., before its being ported into the Athena framework), but is also attained a smaller fake rate. For further improvements, track preselection cuts are optimized and new preselection criteria are defined (Table 5.1). Since the new track preselection cuts are looser than the previous set of cuts, the efficiency of both algorithms has improved. The fake rate is decreased due to placing a cut on the

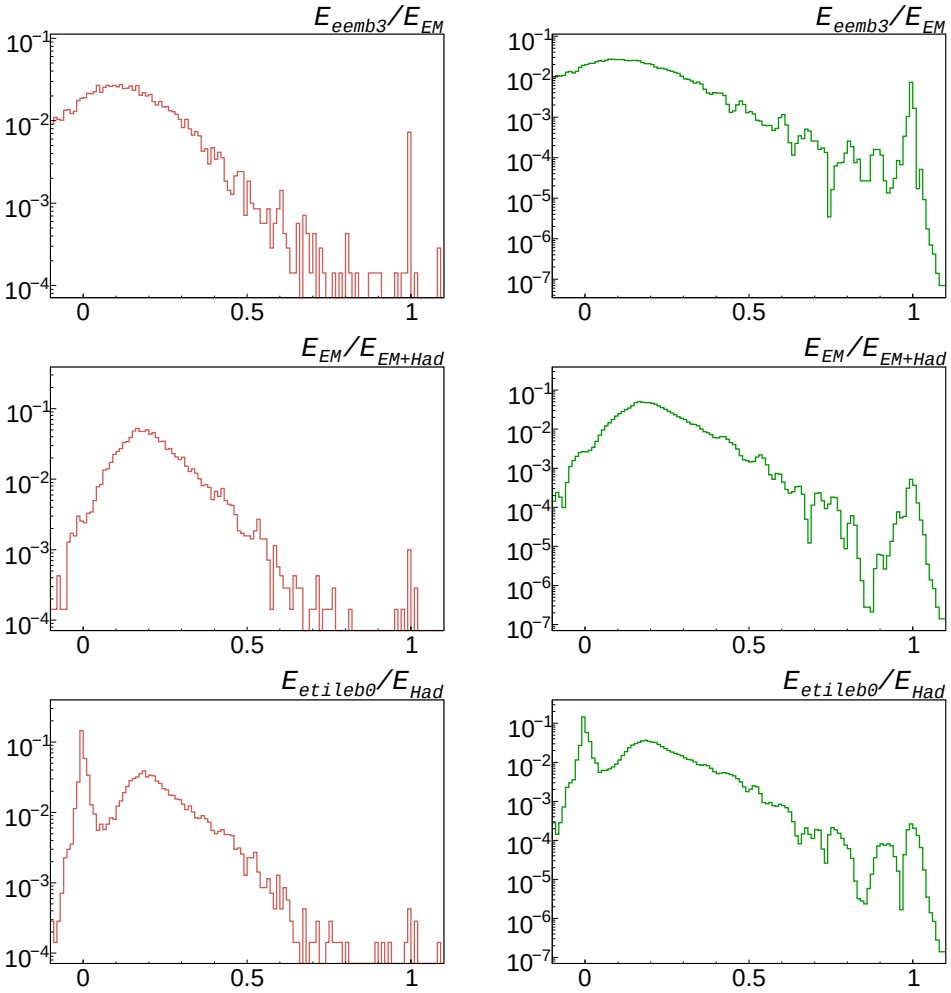

Figure 5.11. Signal PDF distributions for several variables before (left) and after (right) the Smooth method is applied.

transverse impact parameter (d_0) and its significance (d_0/σ_{d_0}). The impact parameter, d_0, is defined as the distance of closest approach on the transverse plane of the particle to the primary vertex. These parameters help for further rejection of non-isolated muons, like the ones coming from semileptonic decays of b quarks, which are mostly originating from displaced vertices (see Figure 5.12).

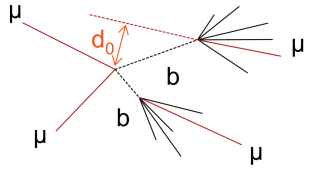

Figure 5.12. Illustration of the transverse impact parameter (d_0) for $Zb\bar{b} \rightarrow 4\mu$ process.

Table 5.1. Track preselection cuts for *CaloLR* and *CaloMT* algorithms.

New Track Preselection Cuts			
	Barrel	Crack	EndCap
p_T	> 2 GeV/c	-	> 2 GeV/c
E_T^{iso}	< 15 GeV	< 8 GeV	< 12 GeV
$\log_{10}(E_T^{\text{iso}}/p_T)$	< 0.4	< 0.1	< 0.2
$\log_{10}(P_T^{\text{iso}}/p_T)$	< 0.7		
Max d_0	< 0.12		
Max d_0/σ_{d_0}	< 7		
Old Track Preselction Cuts			
	Barrel	Crack	EndCap
p_T	> 2 GeV/c	-	> 3 GeV/c
E_T^{iso}	< 10 GeV	-	< 8 GeV
$\log_{10}(E_T^{\text{iso}}/p_T)$	< 0		
$\log_{10}(P_T^{\text{iso}}/p_T)$	< 0		

5.5. Performance

Performance of the improved *CaloLR* algorithm is evaluated (in release 14) on single muons and several physics processes. The results are shown compared to the *CaloMT* algorithm. *CaloLR* performs very good after the improvements to it and in addition, new track preselection cuts influenced the performance of both *CaloLR* and *CaloMT*. Here, the performance is shown after the both improvements; improved *CaloLR* and improved track preselection cuts. Two main quantities are used to show

the performance of the algorithms: the efficiency and the fake rate. Since the performance is tested on the simulated Monte Carlo data samples, quantities like; true particle type, η, p_T of the tracks are known. Efficiency is obtained by dividing the number of muons correctly identified by the algorithm to the number of true MC muons. Fake rate is defined as the number of tracks per event incorrectly identified as muons.

5.5.1. Single muons

Firstly, the performance of the algorithms is studied on several single-muon samples with fixed-momenta of 5, 10, 100, 1000 GeV/c (in Appendix B, Data Samples 1a, 1b, 1c and 1d, respectively) that are fully simulated and reconstructed within Athena, release 12.0.6. The plots on the left (right) side in Figure 5.13 show the efficiency vs. η (p_T) of $CaloLR$ in comparison to $CaloMT$. In Figures 5.14, 5.15, 5.16 and 5.17 top (bottom) left plots show the η (p_T) of all the true muon tracks in the data sample and top (bottom) right plots show the η (p_T) of $CaloLR$ muon tracks, for the same single muon samples. Since the algorithms use the ID tracks as muon candidates, $|\eta|$ extends until 2.5. As can be seen from the Figure 5.13, for 5 GeV/c muons the efficiency of both algorithms falls rapidly to zero after $\eta = 1.6$, due to the cut on the p_T of tracks. To put it in another way, transverse component of momenta for tracks with 5 GeV/c momentum is less than 2 GeV/c if they are in the endcap region ($\eta > 1.6$), thus they are rejected during the track preselection. On can see in Figures 5.14 and 5.15 that the tracks in the endcap regions (with $p_T < 2$ GeV/c) are rejected. This accounts for 0.55 (0.47) efficiency of $CaloLR$ ($CaloMT$) for 5 GeV/c muons and 0.76 (0.76) efficiency for 10 GeV/c muons in the full η range. However, for tracks in the barrel region the efficiency is sufficiently high. The efficiency of $CaloLR$ ($CaloMT$) algorithm reaches 0.96 (0.92) for 100 GeV/c muons and 0.93 (0.80) for 1000 GeV/c muons in the full η range, since all the tracks have p_T greater than 2 GeV/c. Performance on single muons mainly shows how much track preselection cuts take away from the efficiency, since single muons are isolated. This study shows that, $CaloLR$ is performing well on single muons with a wide range of momentum, even on very low mometum single muons.

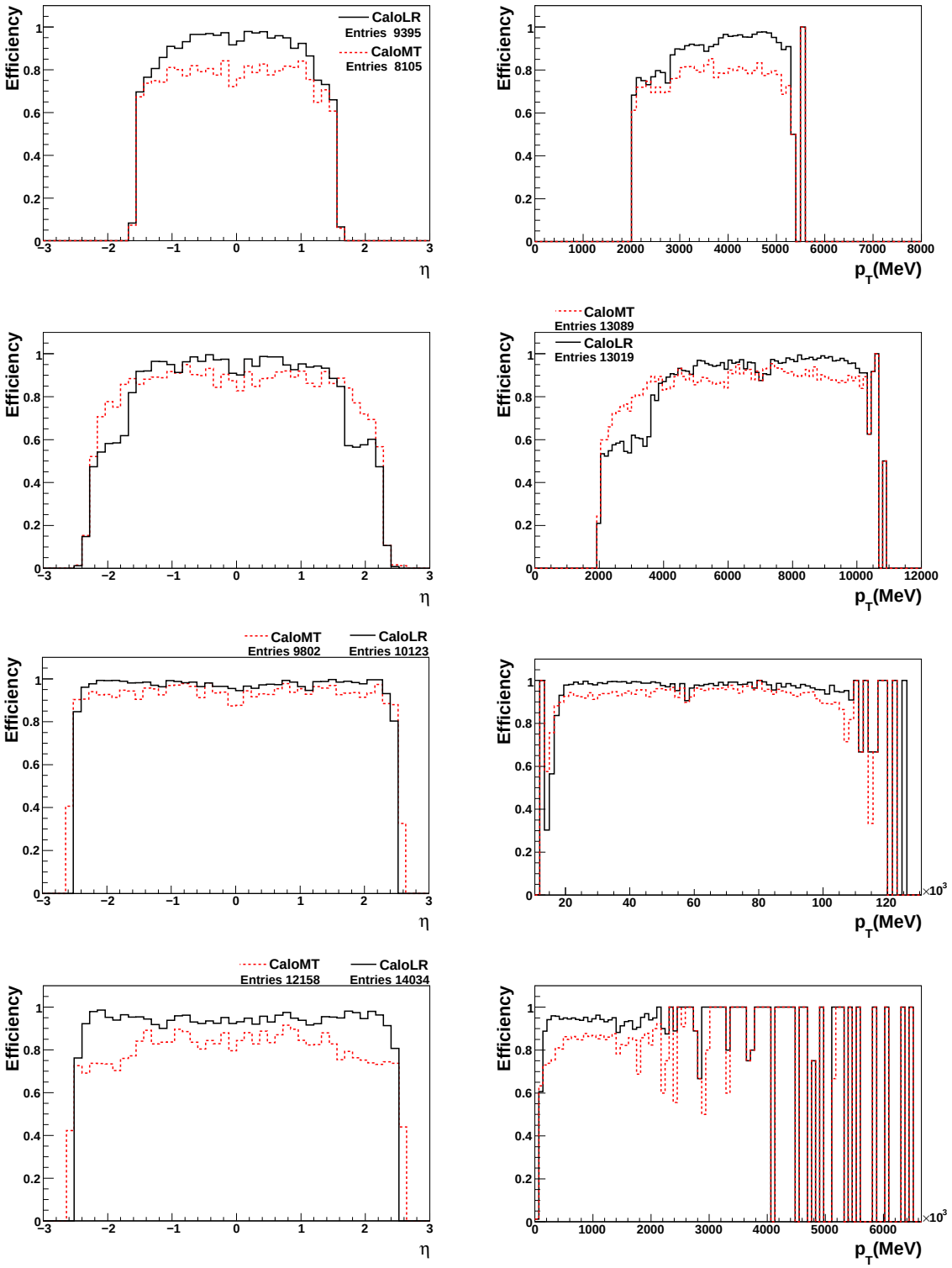

Figure 5.13. Efficiency vs η (right plots) and p_T (left plots) for single-muon samples with fixed-momentum of 5, 10, 100 and 1000 GeV/c (from top to bottom). Solid lines represent the *CaloLR* and dashed lines in red represent the *CaloMT*.

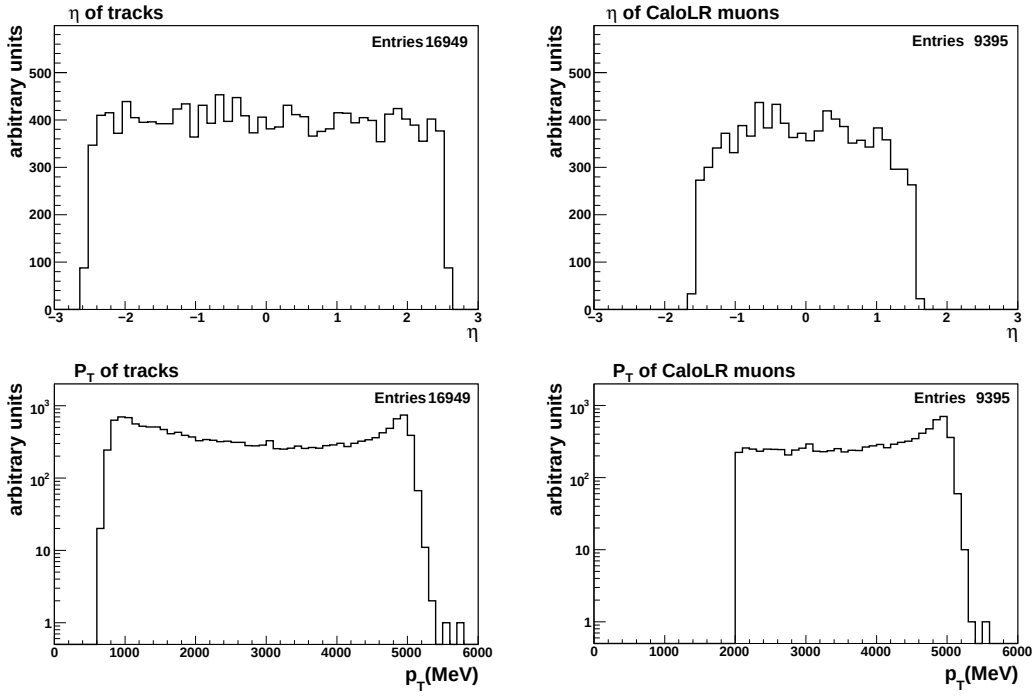

Figure 5.14. Top (bottom) left plot η (p_T) of all tracks, top (bottom) right plot η (p_T) of $CaloLR$ muons for single-muon sample with fixed-momentum of 5 GeV/c.

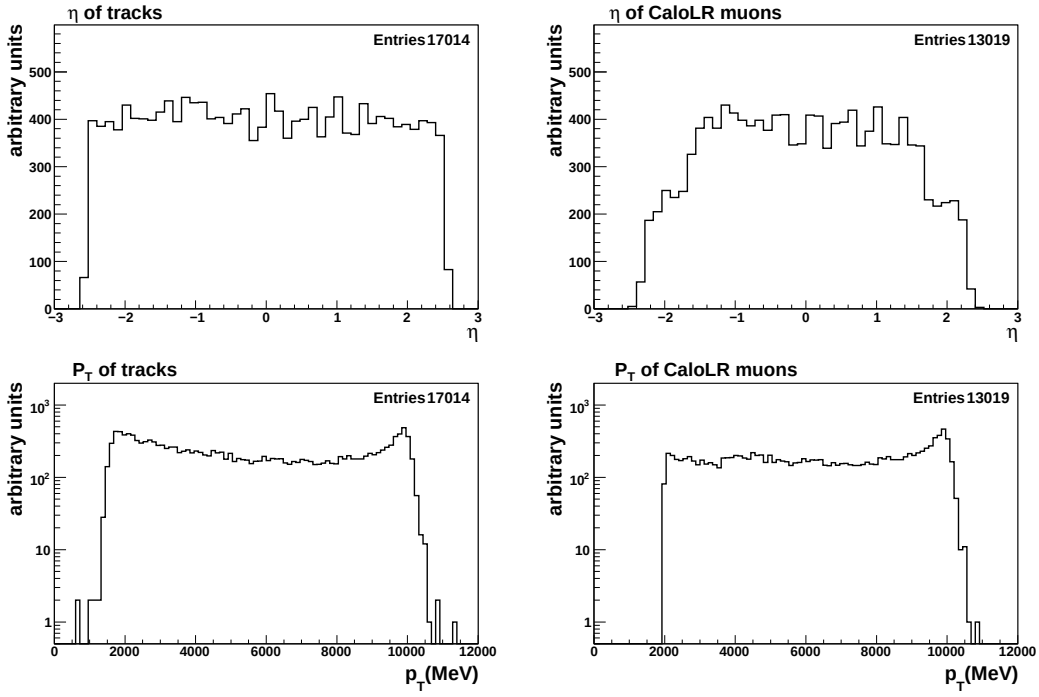

Figure 5.15. Top (bottom) left plot η (p_T) of all tracks, top (bottom) right plot η (p_T) of $CaloLR$ muons for single-muon sample with fixed-momentum of 10 GeV/c.

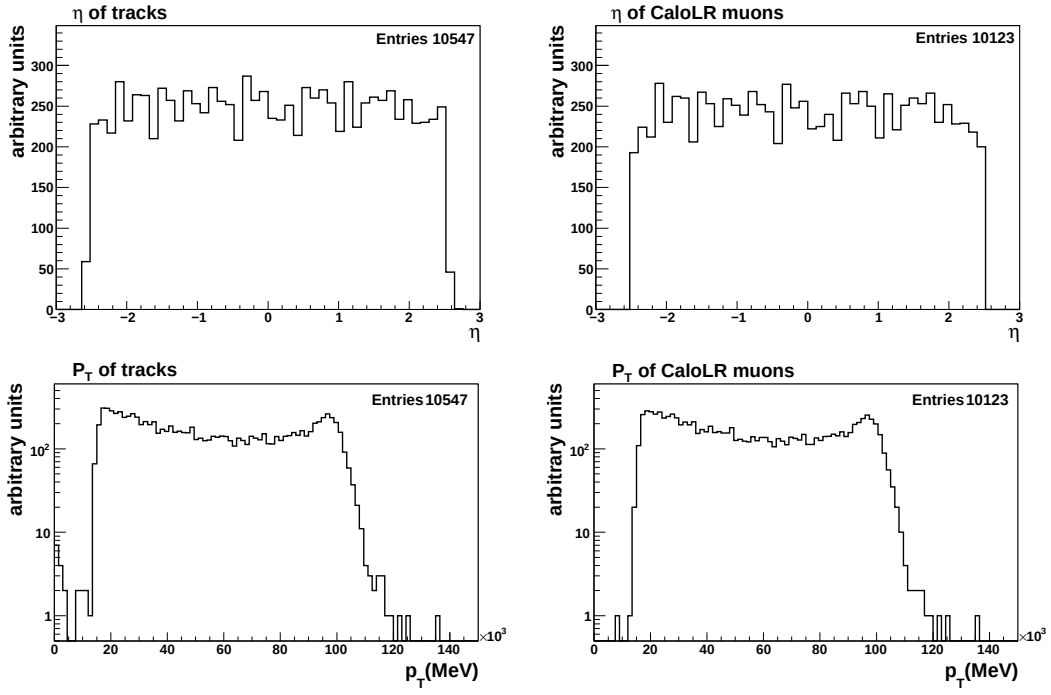

Figure 5.16. Top (bottom) left plot η (p_T) of all tracks, top (bottom) right plot η (p_T) of $CaloLR$ muons for single-muon sample with fixed-momentum of 100 GeV/c.

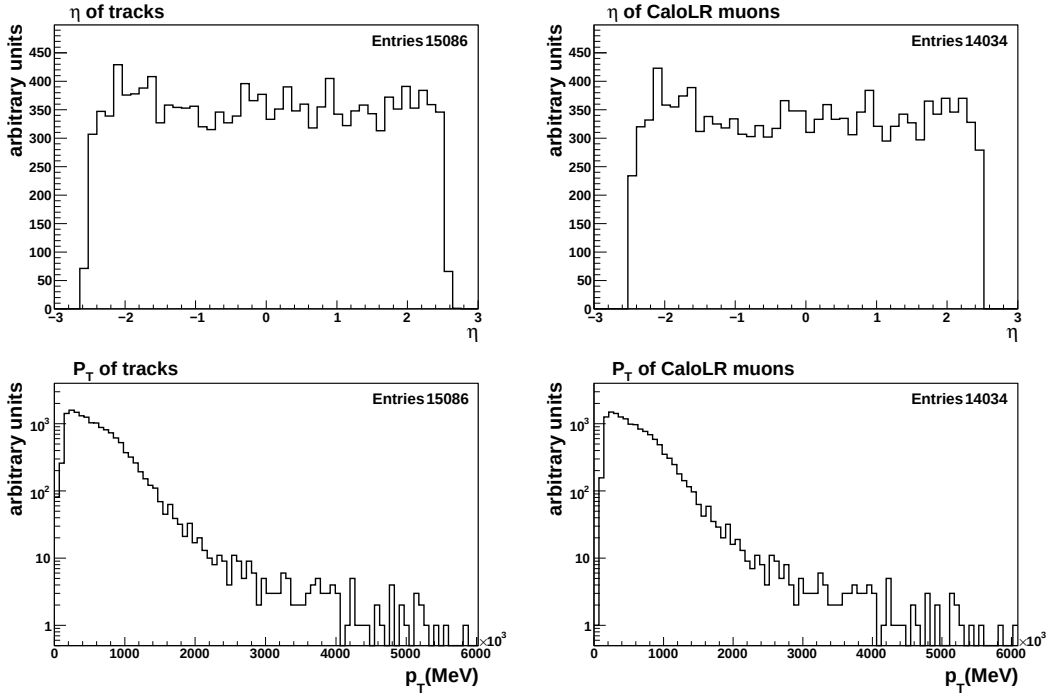

Figure 5.17. Top (bottom) left plot η (p_T) of all tracks, top (bottom) right plot η (p_T) of $CaloLR$ muons for single-muon sample with fixed-momentum of 1000 GeV/c.

5.5.2. Physics processes

In this section, the performance of the *CaloLR* algorithm is evaluated on samples corresponding to several physics processes; in particular, $H \rightarrow ZZ^* \rightarrow 4\ell$, $ZZ \rightarrow 4\ell$, $Zb\bar{b} \rightarrow 4\ell$ and $t\bar{t} \rightarrow 4\ell$ (in Appendix B, Data Samples 2a, 2b, 2c and 2d, respectively) decay channels are chosen because the application of the algorithm to $H \rightarrow ZZ^* \rightarrow 4\ell$ analysis is studied in the next section. All the data samples were simulated and reconstructed within Athena, release 12.0.6. In all cases, a 4-lepton generator-level filter is applied.

- $pp \rightarrow H \rightarrow ZZ^* \rightarrow 4\ell$: generated with Pythia, a Higgs particle with an invariant mass of 130 GeV forced to decay into two Z bosons, one of which is virtual for $M_H < 180$ GeV. The Z bosons are further forced to decay into leptons (electrons and muons).
- $pp \rightarrow ZZ \rightarrow 4\ell$: generated with Pythia, each Z boson forced to decay into lepton pairs.
- $pp \rightarrow Zb\bar{b} \rightarrow 4\ell$: generated with AcerMC, a Z boson produced in association with two b quarks, and forced to decay into two charged leptons.
- $pp \rightarrow t\bar{t} \rightarrow 4\ell$ was generated with MC@NLO, pair produced top quarks with all allowed decay channels.

For a more realistic study of the performance, data samples that include pile-up and cavern background (CB) effects are used. Pile-up effects include hits from interactions other than the one of primary interest. CB consists of thermalized slow neutrons and low energy photons, produced in the interaction of primary hadrons from p-p collisions with the materials of the detector and of the collider. They interact with matter and produce secondaries. All the samples for the above physics processes include pile-up and CB with a safety factor (SF) of 5, i.e., five times the nominal value, where the nominal value is the expected amount of CB for ATLAS at a luminosity of $10^{33} cm^{-2} s^{-1}$.

Figures 5.18 and 5.19 show the efficiency and fake rate vs η for the selected samples, where the vertical axis on the left of the plots shows the efficiency and the vertical axis on the right shows the fake rate, represented by the shaded histograms. As can be seen from Figure 5.18, the efficiency of the algorithms on $H \rightarrow ZZ^* \rightarrow 4\ell$ and $ZZ \rightarrow 4\ell$ samples is similarly high. This shows the algorithms' good performance for identifiying muons originating from Z boson decays, which are mostly isolated and originate from the main interaction point. However, for $Zb\bar{b} \rightarrow 4\ell$ sample the efficiency is ≈ 0.5 as can be seen in Figure 5.19, for half of the muons in the final state of this process are produced by the semileptonic decays of b quarks, where these muons are mostly (if the b quark is highly energetic) inside a jet produced by a c quark, thus non-isolated and also coming from secondary displaced vertices, therefore mostly rejected at the track preselection phase by the cuts on isolation and impact parameter. For the $t\bar{t} \rightarrow 4\ell$ sample, the efficiency falls to ≈ 0.3 as illustrated in Figure 5.19. The poor efficiency for $t\bar{t} \rightarrow 4\ell$ sample can be explained by the fact that, two of the muons in the final state of this process are coming from the semileptonic decay of energetic b quarks and rejected in the track preselection phase, and the other two from W boson decays that are mostly isolated. Therefore, the efficiency on this sample shows the performance of tagging muons coming from W boson decays.

In Figure 5.21 left plots show the p_T of all the tracks that are not muon and right plots show the p_T of the true muon tracks, for $H(130) \rightarrow ZZ^* \rightarrow 4\ell$, $ZZ \rightarrow 4\ell$, $Zb\bar{b} \rightarrow 4\ell$ and $t\bar{t} \rightarrow 4\ell$ samples, respectively. Since CB effects are included in the samples, there is a large number of tracks with $p_T < 5$ GeV/c, which degrades the performance of the algorithms for $p_T < 5$ GeV/c region and most of the fakes of $CaloLR$ come from tracks with $p_T < 5$ GeV/c, as can be seen in Figure 5.20. For $CaloMT$, the peaks in the fake rate in η match the regions where the acceptance of the last calorimeter sampling is limited, and the two previous samplings are used for muon identification. Because of the higher electronic noise, $CaloMT$ presents a higher fake rate in the HEC than in the TileCal [48].

Although the recent efficiency of both algorithms is similar in the studied physics processes, there is a big difference in the number of tracks that are misidentified per

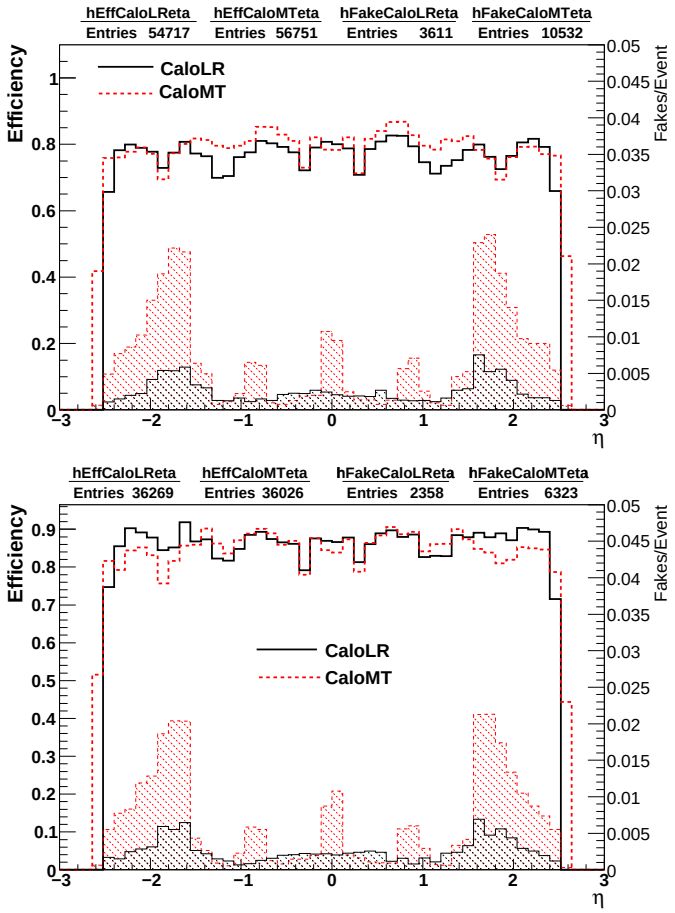

Figure 5.18. Efficiency and fake rate vs η for $H(130) \rightarrow ZZ^* \rightarrow 4\ell$ (top plot) and $ZZ \rightarrow 4\ell$ (bottom plot). Right vertical axis shows the fake rate (represented by shaded histograms) and left vertical axis shows the efficiency. Solid black line: $CaloLR$, dashed red line: $CaloMT$.

event. Since both algorithms are implemented in the same package, using the same external tools and the same track preselection criteria, the big difference in the number of fakes is due to the different strategies they apply. $CaloMT$ has a straightforward method that applies some cuts on the deposited energies to identify muons, where $CaloLR$ makes use of a likelihood ratio built from energy deposition patterns. Furthermore, $CaloMT$ tags muons by using only hadronic calorimeter deposits, where $CaloLR$ tags muons by using energy depositions in all the calorimeter samples. The performance of the two algorithms is summarized in Table 5.2 before and after the improvements for $CaloLR$ and new track preselections. Improved performance of $CaloLR$ algorithm can be observed if compared to the previous performance. Plots showing the

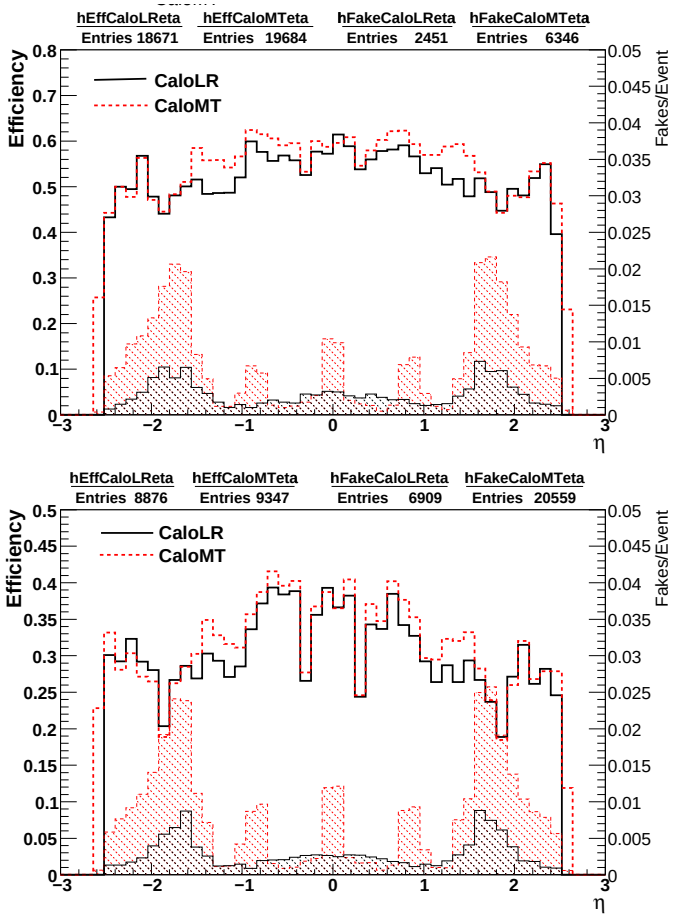

Figure 5.19. Efficiency and fake rate vs η for $Zb\bar{b} \rightarrow 4\ell$ (top plot) and $t\bar{t} \rightarrow 4\ell$ (bottom plot). Right vertical axis shows the fake rate (represented by shaded histograms) and left vertical axis shows the efficiency. Solid black line: $CaloLR$, dashed red line: $CaloMT$.

previous performance (in release 13) of both $CaloLR$ and $CaloMT$ algorithms on the same physics samples considered in this study can be seen in Appendix C.

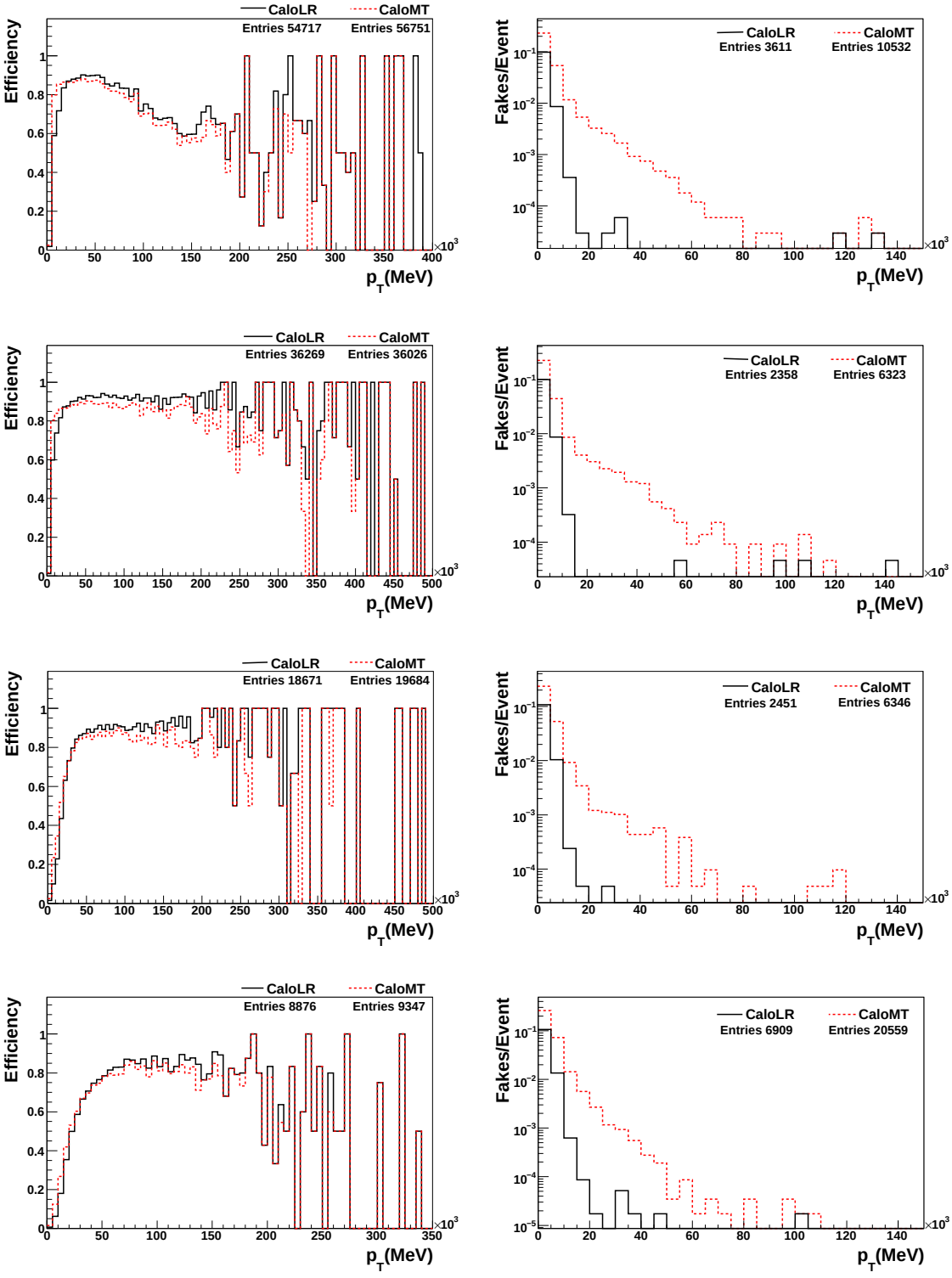

Figure 5.20. Efficiency and fake rate vs. p_T of $CaloLR$ (black solid lines) and $CaloMT$ (dashed red lines) for the physics samples considered: from top to bottom, $H(130) \rightarrow ZZ^* \rightarrow 4\ell$, $ZZ \rightarrow 4\ell$, $Zb\bar{b} \rightarrow 4\ell$, $t\bar{t} \rightarrow 4\ell$.

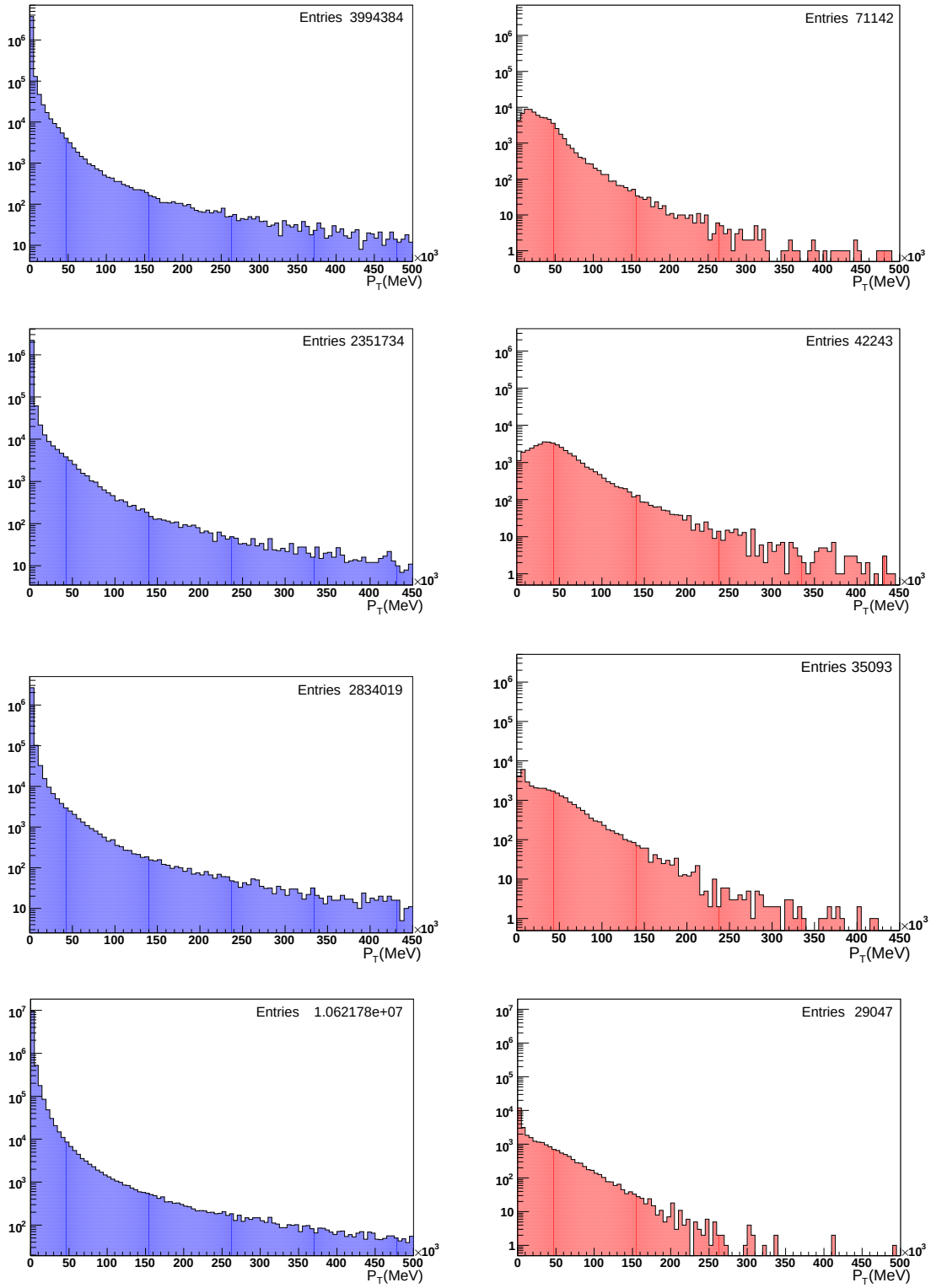

Figure 5.21. p_T of non-muon tracks (left plots) and true muon tracks (right plots) for the physics samples considered: from top to bottom, $H(130) \to ZZ^* \to 4\ell$, $ZZ \to 4\ell$, $Zb\bar{b} \to 4\ell$, $t\bar{t} \to 4\ell$.

Table 5.2. Summary of the efficiencies and fakes per event (f/e) for different physics processes before and after the improvements.

BEFORE THE IMPROVEMENTS ([56])				
	CaloLR		*CaloMT*	
	Efficiency	Fake/e	Efficiency	Fake/e
$H \rightarrow 4\ell$	0.66	1.98	0.86	0.09
$Zb\bar{b} \rightarrow 4\ell$	0.51	2.17	0.69	0.14
$t\bar{t} \rightarrow 4\ell$	0.40	2.8	0.54	0.16
AFTER THE IMPROVEMENTS				
	CaloLR		*CaloMT*	
	Efficiency	Fake/e	Efficiency	Fake/e
$H \rightarrow 4\ell$	0.76	0.05	0.79	0.14
$ZZ \rightarrow 4\ell$	0.85	0.05	0.85	0.14
$Zb\bar{b} \rightarrow 4\ell$	0.53	0.06	0.56	0.18
$t\bar{t} \rightarrow 4\ell$	0.30	0.23	0.32	0.70

5.6. Application to the $H \rightarrow ZZ^{(*)} \rightarrow 4\ell$ analysis

In this study, application of the *CaloLR* algorithm is examined on the analysis of Higgs to four leptons channel for $m_H = 130$ GeV, in the case of four muons in the final state. The aim is to see if the perfomance improves, when muons tagged by the *CaloLR* algorithm are added to the analysis. In order to assess this, the analysis is repeated using four different sets of muons preselected by four different sets of algorithms. The first set of muons is preselected by a combined muon reconstruction algorithm (*STACO*), the second one by including the muons found by a segment tag algorithm (*STACO* + *MuTag*), the third one by adding *CaloLR* muons (*STACO* + *MuTag* + *CaloLR*) and the fourth one by adding *CaloMT* muons (*STACO* + *MuTag* + *CaloLR* + *CaloMT*) to the set. In order to avoid overlaps, i.e., using the same muon found by two or more algorithms, the candidate muons are required to be outside the cone of a radius of $\Delta R = 0.01$ around the muons already found.

The analysis is based on investigation of observability of the signal by reconstructing its invariant mass from the addition of the four-momenta of the four muons in the final state. The observability of a signal depends on its backgrounds, which give the same final state particles. In the case of a 130 GeV Higgs to four lepton channel, the main backgrounds are $ZZ \rightarrow 4\ell$, $Zb\bar{b} \rightarrow 4\ell$ and $t\bar{t} \rightarrow W^+bW^-\bar{b} \rightarrow 4\ell$ decays (see Chapter 2). It is important to reduce their unwanted contribution to invariant mass reconstruction of the signal. For this purpose one needs background specific criteria in the event selection that eliminate the events as much as possible at which the final state muons come from background processes. In this study, similar event selection criteria are used as in the $H \rightarrow ZZ^{(*)} \rightarrow 4\ell$ analysis in [48], where they have been optimized for each Higgs mass considered in the note. Each event is required to have;

- at least 4 muons with $|\eta| < 2.5$ and $p_T > 7$ GeV/c,
- at least 2 of these muons with $p_T > 20$ GeV/c,
- the selected muons grouped in two pairs of opposite charge,
- $\Delta M_Z < 15$ GeV; the on-shell Z invariant mass consistent with the known Z boson mass 91.18 GeV (when more than one muon pair satisfying this criteria is found, the one with a mass closest to the known Z boson mass is chosen),
- $M_{Z^*} > 20$ GeV; the off-shell Z^* invariant mass higher than a threshold value (if more than one muon pair satisfying this criteria is found, the one with the highest p_T muons is chosen),
- $\sum p_T/p_T < 0.15$, inside $0.02 < \Delta R < 0.2$; track isolation cut,
- $d_0/\sigma_{d_0} < 5$; vertexing cut,
- $|m_H - 130 \text{ GeV}| < 5$ GeV; Higgs mass window.

ZZ background gives a four muon final state exactly the same as the signal, therefore its contribution is irreducible. $Zb\bar{b}$ background is an important one since it contains one real Z boson and has a large cross section compared to the SM Higgs cross section. $t\bar{t}$ background is the dominant one due to large numer of top production at LHC. However, further rejection of $Zb\bar{b}$ and $t\bar{t}$ backgrounds is possible due to the presence of b-jets in their final states. Semileptonic decays of b quarks result in the non-isolated muons from displaced vertices, whereas, muons coming from Z and W boson

decays are significantly more isolated and originate from the main interaction point. Since the purpose is to reject these events where the final state muons are non-isolated, the track preselection criteria described in Section 4.2 overlap with the event selection criteria used in this analysis. Non-isolated muons coming from semileptonic b quark decays can be rejected by applying cuts on track-based and calorimeter-based isolation parameters and on transverse impact parameter of the tracks. The selection cut is placed at 0.15, inside an annulus of $0.02 < \Delta R < 0.2$, for the normalized track-based isolation parameter in this analysis. And the cut on the transverse impact parameter significance (d_0/σ_{d_0}, impact parameter normalized to its error) of the tracks is placed at 5. Monte-Carlo samples for signal and background processes used in this analysis are described in the previous section.

In Tables 5.3, 5.4, 5.5 and 5.6 the number of events and the fraction of events (in %) passed after each event selection cuts for signal, ZZ, $Zb\bar{b}$ and $t\bar{t}$ samples are shown respectively. The available MC statistics for the samples used in this study are not sufficient for a detailed analysis, however, we can still have an idea about the improvement achieved by using $CaloLR$ algorithm muons additionally in the analysis. It is observed that the extra muons found by $CaloLR$ make a noteworthy increase in the statistics for invariant mass reconstruction of the Higgs boson. It can be seen from Table 5.3 that there is 17% gain in the number of reconstructed events for signal when the extra muons identified by the $CaloLR$ algorithm are added to those found by $STACO$ and $MuTag$. For the ZZ irreducible background 13% increase and for the $Zb\bar{b}$ and $t\bar{t}$ backgrounds no increase in the number of reconstructed events is observed.

Figure 5.22 shows the distributions of the reconstructed Higgs mass peak, with four different preselected muon sets. The increase in the number of reconstructed events due to $CaloLR$ algorithm can be seen from this figure. Most important features of these extra muons are that they are mainly around the $\eta = 0$ region (left plot in Figure 5.23) and at low p_T (right plot in Figure 5.23), as expected. Figure 5.24 shows the gaussian fitted distributions of reconstructed Higgs mass from four different muon sets. As can be seen from this figure, the addition of $CaloLR$ muons does not affect the resolution of the reconstructed mass and also doesn't induce a shift in the mean of the mass peak.

Table 5.3. Number of events and fraction of events (in %) after each event selection cut for $H(130GeV) \rightarrow ZZ^* \rightarrow 4\ell$.

$H \rightarrow ZZ^* \rightarrow 4\ell$								
	STACO		**+MuTag**		**+CaloLR**		**+CaloMT**	
Selec. Cut	**Events**	**%**	**Events**	**%**	**Events**	**%**	**Events**	**%**
No cuts	33700	100	33700	100	33700	100	33700	100
4 μ	6151	18.25	7523	22.32	8893	26.38	10299	30.56
Good η	6026	17.88	7395	21.94	8763	26.00	10159	30.14
Good p_T	4889	14.50	5415	16.06	6308	18.71	6427	19.07
2 pairs	4875	14.46	5388	15.98	6288	18.65	6394	18.97
Z mass cuts	3478	10.32	3850	11.42	4493	13.33	4580	13.59
Track Iso.	2616	7.76	2878	8.54	3369	9.99	3407	10.10
IP cut	2398	7.11	2638	7.82	3089	9.16	3124	9.27
H Mass win.	2191	6.50	2386	7.08	2795	8.29	2819	8.36

The cross sections (in fb) for signal and backgrounds after the full event selection and expected Poisson significance for 10 fb^{-1} and 30 fb^{-1} are listed in Table 5.7. In this study, for the calculation of the cross sections after the full event selection (σ_{rec}), the effective cross sections (σ_{eff}) for 4μ channel in $H(130) \rightarrow ZZ^* \rightarrow 4\ell$ analysis in [48] are used:

$\sigma_{eff} = 3.95\ fb$ for signal,

$\sigma_{eff} = 52.57\ fb$ for $ZZ \rightarrow 4\ell$ irreducible background and

$\sigma_{eff} = 812.1\ fb$ for $Zb\bar{b} \rightarrow 4\ell$ reducible background

Cross sections after the full event selection is calculated by multiplying the effective cross section with the reconstruction efficiency as the following equation:

$$\sigma_{rec} = \sigma_{eff} \cdot (\frac{\text{number of events passed all the event selection cuts}}{\text{total number of events in the sample}}) \qquad (5.4)$$

Table 5.4. Number of events and fraction of events (in %) after each event selection cut for irreducible background $ZZ \to 4\ell$.

$ZZ \to 4\ell$								
	STACO		**+MuTag**		**+CaloLR**		**+CaloMT**	
Selec. cut	**Events**	**%**	**Events**	**%**	**Events**	**%**	**Events**	**%**
No cuts	21750	100	21750	100	21750	100	21750	100
4 μ	3818	17.55	4675	21.49	5476	25.17	6298	28.95
Good η	3712	17.06	4561	20.97	5356	24.62	6181	28.41
Good p_T	3322	15.27	3701	17.01	4235	19.47	4284	19.69
2 pairs	3299	15.16	3667	16.85	4203	19.32	4240	19.49
Z mass cuts	3049	14.01	3391	15.59	3884	17.85	3913	17.99
Track Iso.	2612	12.00	2904	13.35	3329	15.30	3342	15.36
IP cut	2265	10.41	2526	11.61	2904	13.35	2916	12.02
H Mass win.	26	0.119	30	0.137	34	0.156	36	0.165

Poisson significance is calculated with the equation:

$$ss = \sqrt{2}\sqrt{(s+b)\ln(1+s/b) - s} \tag{5.5}$$

where, s is the number of expected signal events and b is the expected total background events after the full event selection. Since no events passed the event selection for the $t\bar{t}$ sample, 90% C.L. limits on the cross section are set for this sample and it is assumed not to contribute to the significance.

Finally, the mass distribution for signal and background after event selection is presented in Figure 5.25, where the expected signal is clearly seen above the background.

Table 5.5. Number of events and fraction of events (in %) after each event selection cut for reducible background $Zb\bar{b} \rightarrow 4\ell$.

$Zb\bar{b} \rightarrow 4\ell$								
	STACO		**+MuTag**		**+CaloLR**		**+CaloMT**	
Selec. cut	**Events**	**%**	**Events**	**%**	**Events**	**%**	**Events**	**%**
No cuts	24370	100	24370	100	24370	100	24370	100
4 μ	2561	10.50	4510	18.50	5432	22.28	6970	28.60
Good η	2502	10.26	4440	18.21	5349	21.94	6874	28.20
Good p_T	1000	4.10	1243	5.10	1382	5.67	1510	6.19
2 pairs	790	3.24	963	3.95	1081	4.43	1156	4.74
Z mass cuts	294	1.20	358	1.46	398	1.63	440	1.80
Track Iso.	6	0.024	7	0.028	9	0.036	12	0.049
IP cut	0		1	0.004	1	0.004	2	0.008
H Mass win.	0		1	0.004	1	0.004	1	0.004

Table 5.6. Number of events and fraction of events (in %) after each event selection cut for reducible background $t\bar{t} \rightarrow 4\ell$.

$t\bar{t} \rightarrow 4\ell$								
	STACO		**+MuTag**		**+CaloLR**		**+CaloMT**	
Selec. cut	**Events**	**%**	**Events**	**%**	**Events**	**%**	**Events**	**%**
No cuts	57728	100	57728	100	57728	100	57728	100
4 μ	131	0.226	1458	2.525	1982	3.433	3845	6.660
Good η	129	0.223	1444	2.501	1963	3.400	3787	6.560
Good p_T	20	0.034	37	0.064	40	0.069	53	0.091
2 pairs	15	0.025	22	0.038	23	0.039	29	0.050
Z mass cuts	5	0.008	6	0.010	6	0.010	8	0.013
Track Iso.	0		0		0		0	

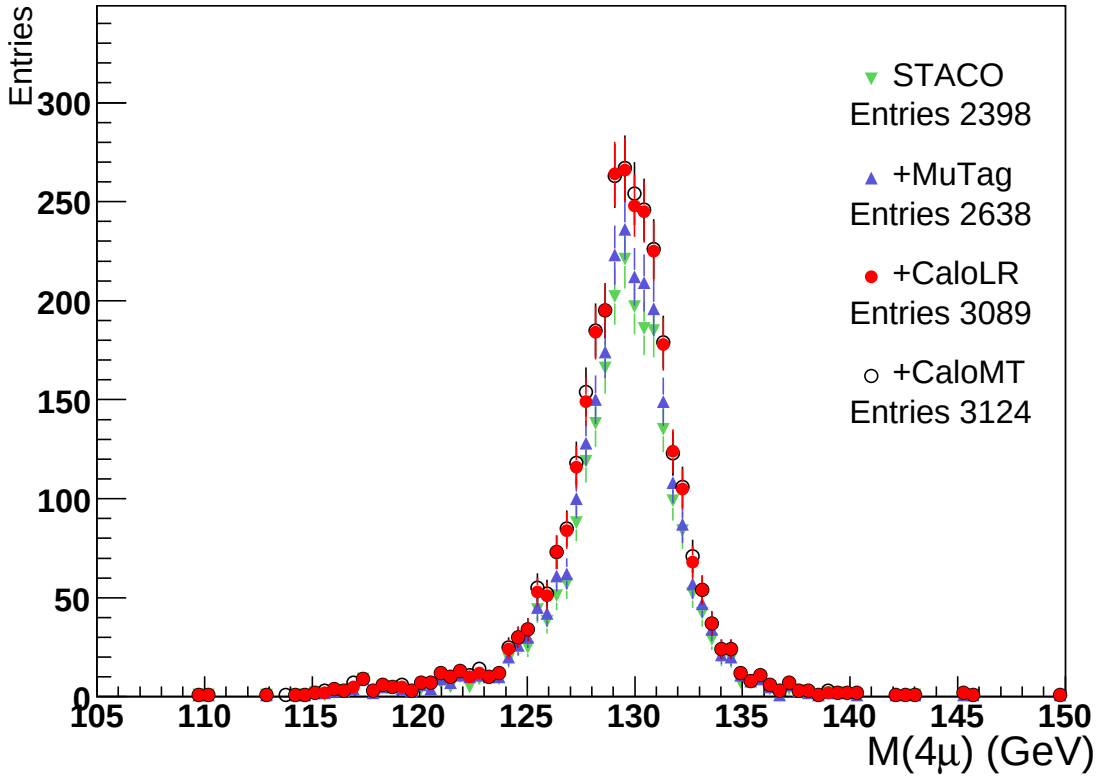

Figure 5.22. Higgs mass peak reconstructed with four different set of muons.

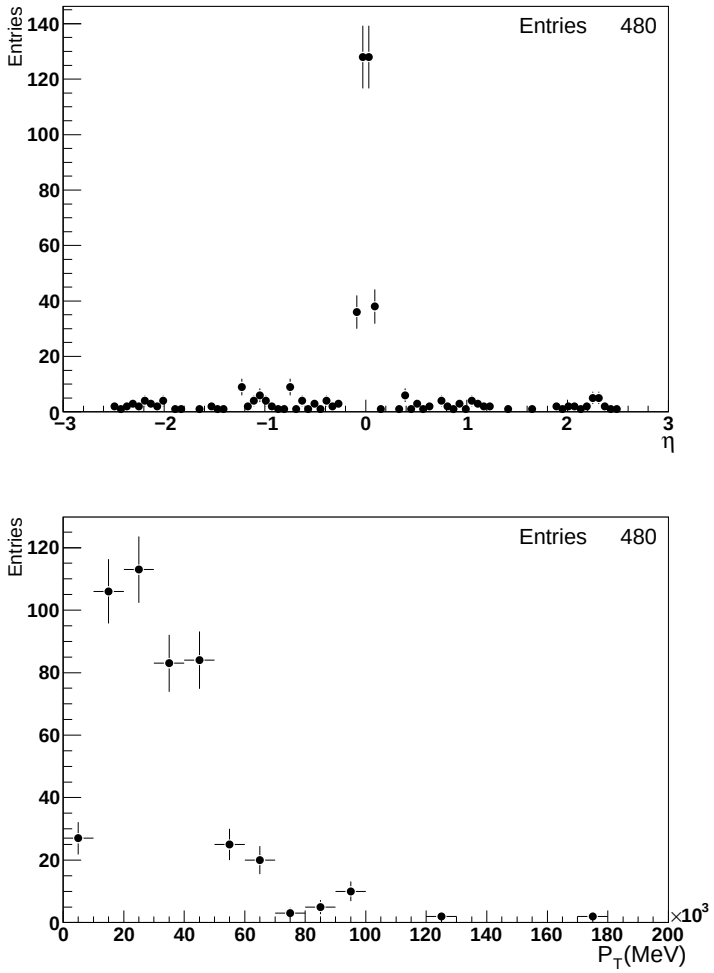

Figure 5.23. η (top plot) and p_T (bottom plot) of the extra muons found by *CaloLR* algorithm.

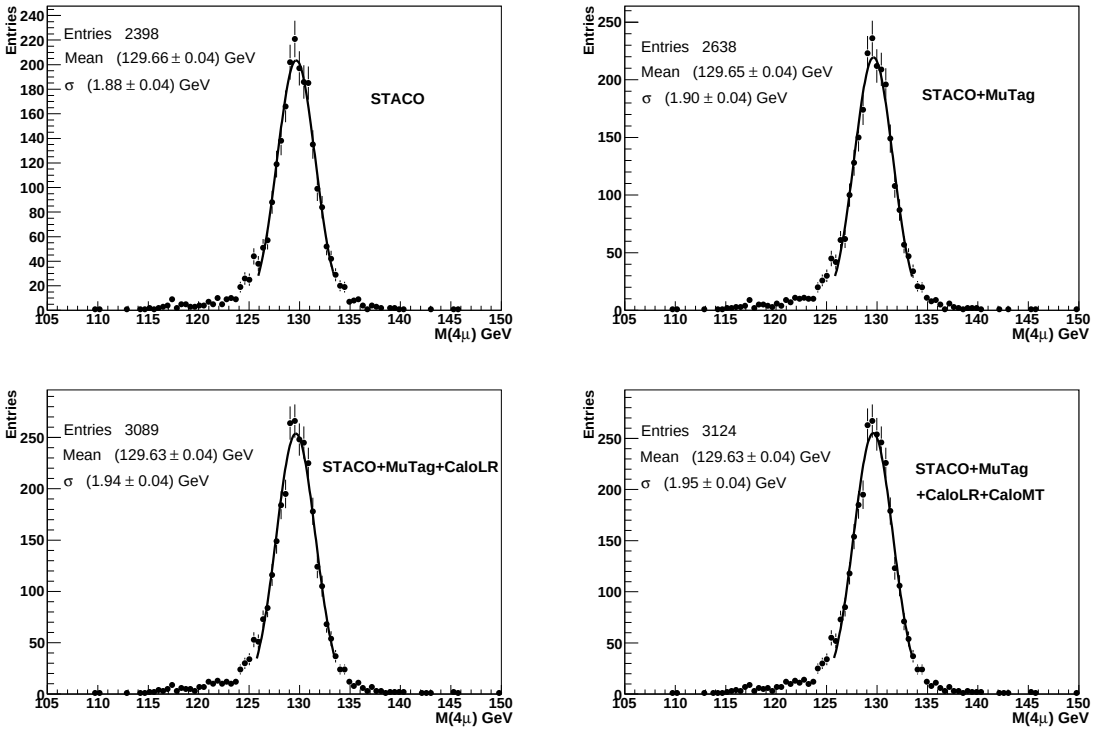

Figure 5.24. Reconstructed Higgs boson mass distribution in the $H \to ZZ^* \to 4\ell$ channel for $m_H = 130$ GeV with different set of muons.

Table 5.7. Cross sections (in fb) after the full event selection for the signal and backgrounds. When no event is passing the event selection, 90% C.L. limits on the cross section are set. The expected significance is given for 10 fb^{-1} and 30 fb^{-1}. The $t\bar{t}$ is assumed not to contribute to the significance.

		STACO+MuTag	**+CaloLR**	**+CaloMT**
Cross Section (in fb)	Signal	$0.280 \pm 1.5{\cdot}10^{-3}$	$0.328 \pm 1.7{\cdot}10^{-3}$	$0.330 \pm 1.7{\cdot}10^{-3}$
	ZZ	$0.072 \pm 4.8{\cdot}10^{-4}$	$0.082 \pm 5.5{\cdot}10^{-4}$	$0.086 \pm 5.8{\cdot}10^{-4}$
	$Zb\bar{b}$	$0.033 \pm 2.1{\cdot}10^{-4}$	$0.033 \pm 2.1{\cdot}10^{-4}$	$0.033 \pm 2.1{\cdot}10^{-4}$
	$t\bar{t}$	< 0.04	< 0.04	< 0.04
Significance (10 fb $^{-1}$)		2.1	2.3	2.3
Significance (30 fb $^{-1}$)		3.6	4.0	4.0

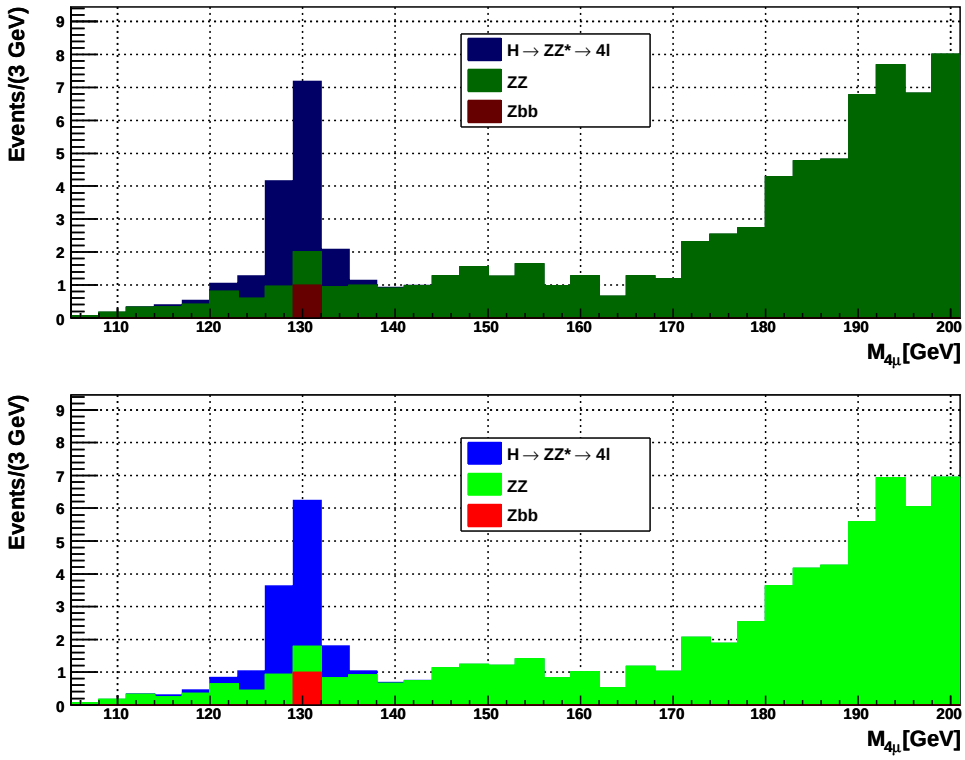

Figure 5.25. Four-muon reconstructed mass distributions for the signal and background processess after the event selection for $m_H = 130$ GeV. Distributions are normalized to a luminosity of 30 fb^{-1}. Bottom plot shows the result obtained with using STACO and MuTag muons, whereas top plot shows the result when *CaloLR* muons are additionally used in the analysis.

5.7. Possible extensions

The performance of the *CaloLR* algorithm can be further improved in several ways. New variables describing the characteristics of muons in the calorimeter can be used in the construction of the likelihood ratio. The discrimination power of some new variables depending on the characteristic shower shape properties of muons have been explored in this thesis work, however, their effects on the performance of the algorithm is still under study. Another implementation for a better performance can be the usage of multivariate techniques, since the variables that *CaloLR* uses to construct the likelihood discriminant are all based on energy loss of muons and thus correlated. Extrapolation of the muon candidate tracks to the muon spectrometer would also be interesting to implement in the algorithm. Although it wouldn't be used as an identification criterion, the information of the tracks matching with a muon spectrometer segment can be used to evaluate the performance of the algorithm with real data.

5.7.1. New variables

In order to achieve a better discrimination of muons from other particles, new identification variables that are based on the characteristic shower shape properties [57], are investigated to be used for the likelihood method that *CaloLR* algorithm applies. Among these, the most promising variables for discrimination are found to be the ones describing the width and the length of the shower, $\langle r^2 \rangle$ and $\langle \lambda^2 \rangle$, respectively. These variables are defined as the second degree cluster moments over the quantities λ and r:

$$\langle \lambda^2 \rangle = \frac{1}{E_{\text{norm}}} \times \sum_{\{i|E_i>0\}} E_i \, \lambda_i^2 \tag{5.6}$$

$$\langle r^2 \rangle = \frac{1}{E_{\text{norm}}} \times \sum_{\{i|E_i>0\}} E_i \, r_i^2 \tag{5.7}$$

with

$$E_{\text{norm}} = \sum_{\{i|E_i>0\}} E_i \tag{5.8}$$

where the index i runs over the cell members only with positive energy in the cluster. λ and r are defined for each cell member of a calorimeter cluster as the following equations:

$$\lambda_i = (\,\vec{x}_i - \vec{c}\,) \cdot \vec{s} \tag{5.9}$$

is the distance of the cell i from the shower center ($\vec{c}$) along the shower axis ($\vec{s}$) and

$$r_i = |\,(\,\vec{x}_i - \vec{c}\,) \times \vec{s}\,| \tag{5.10}$$

is the distance of the cell i from the shower axis.

To study the behavior of these new variables, distributions are obtained from single muon and single pion samples with energies ranging from 1-500 GeV, where these samples are generated and simulated within the Athena framework, release 14.2.10, for this purpose (in Appendix B, Data Samples 3a and 3b, respectively). The distributions are obtained for the nine pseudorapidity-energy bins defined in the description of the *CaloLR* algorithm, that are; three bins in pseudorapidity: barrel ($0 < \eta < 1.4$), crack ($1.4 <= \eta <= 1.6$), endcap ($1.6 < \eta < 2.5$) and three bins in energy: low (E_{truth} <11 GeV), medium (10 GeV< E_{truth} <51 GeV), high (E_{truth} >50 GeV). Normalized distributions of the $\langle\lambda^2\rangle$ variable are shown for single muons (solid red lines) and single pions (dashed blue lines) in Figures 5.26, 5.27 and 5.28 for low, medium and high energy bins, respectively. In the same way, Figures 5.29, 5.30 and 5.31 show the distributions for the $\langle r^2\rangle$ variable. In each of these figures, plots are for barrel, crack and endcap bins from top to bottom.

One can see from these figures that the variable describes the length of the shower has a better discrimination power, according to the fact that, the less distributions of a variable for signal and background overlap, the higher is the discrimination power of this variable. Nevertheless, distributions of both variables can be used as new probability density functions in the calculation of the likelihood ratio and their effects on the performance can be studied.

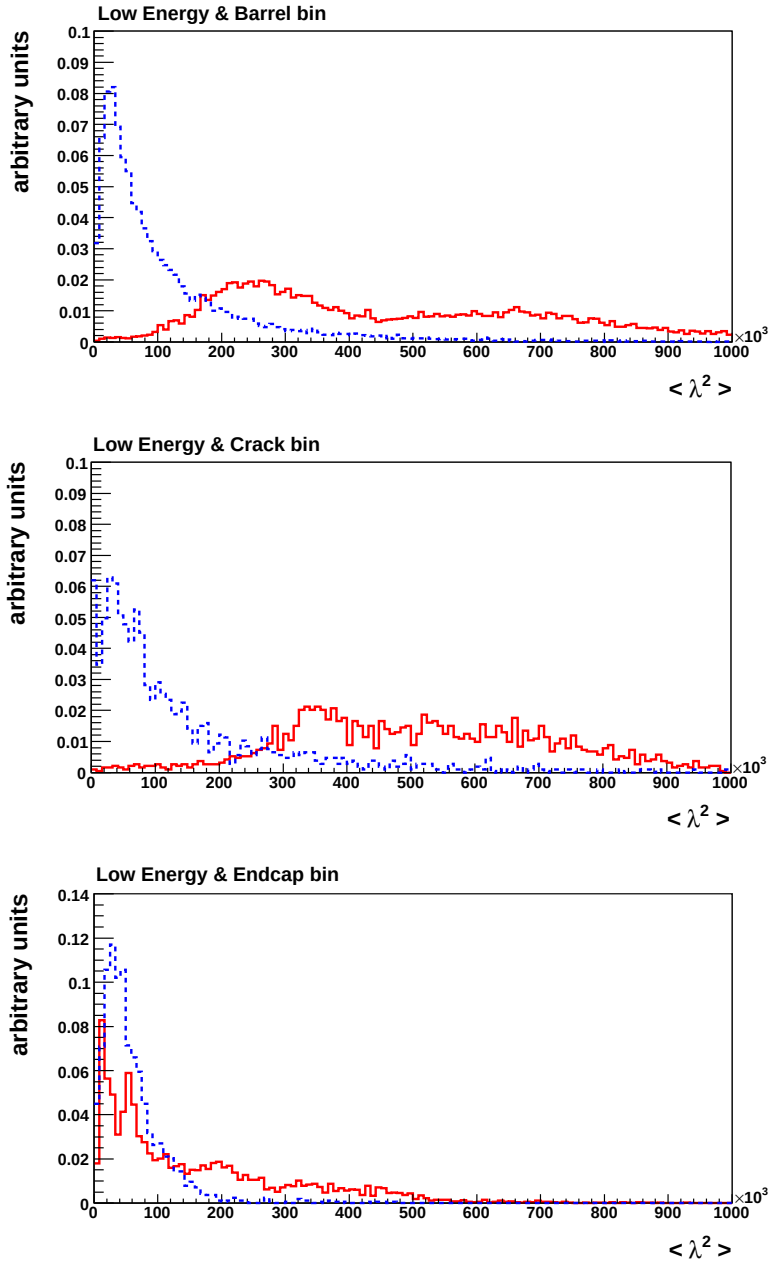

Figure 5.26. Normalized distributions of the $\langle\lambda^2\rangle$ variable for low energy single muons (solid red lines) and single pions (dashed blue lines) in barrel, crack and endcap bin.

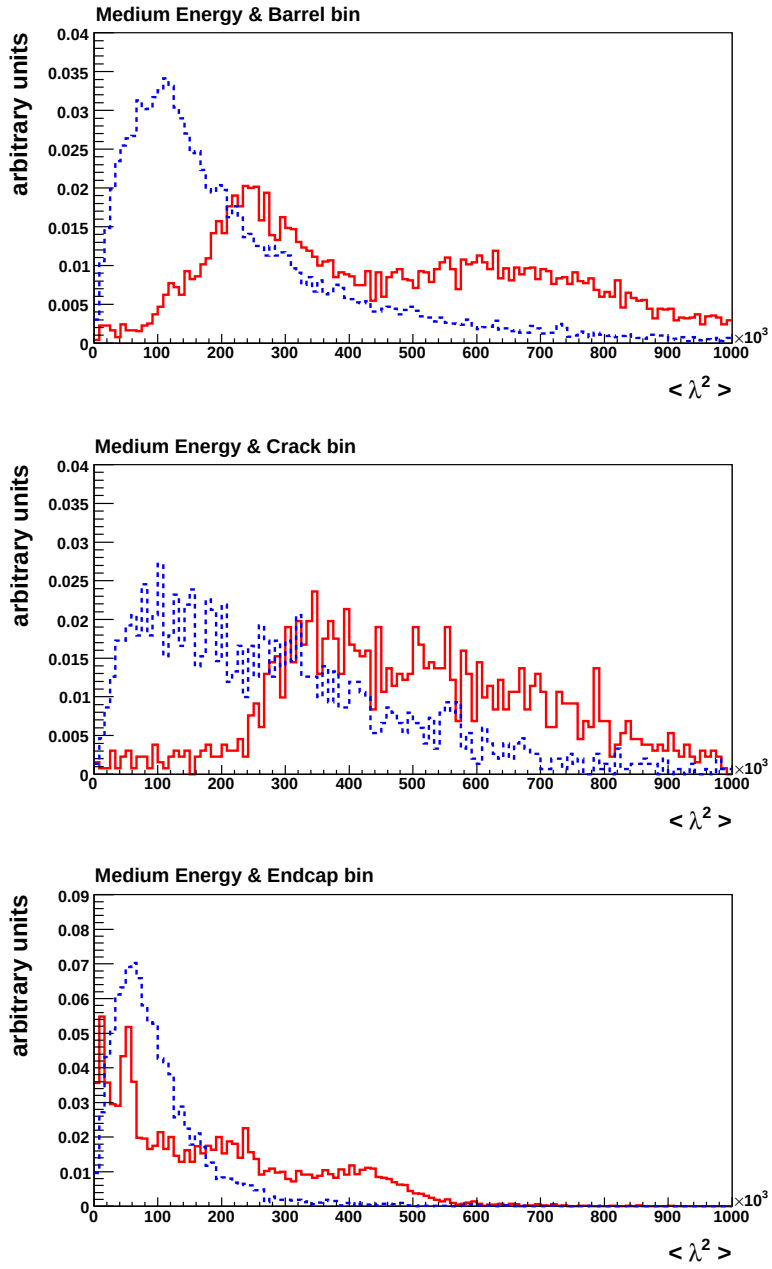

Figure 5.27. Normalized distributions of the $\langle\lambda^2\rangle$ variable for medium energy single muons (solid red lines) and single pions (dashed blue lines) in barrel, crack and endcap bin.

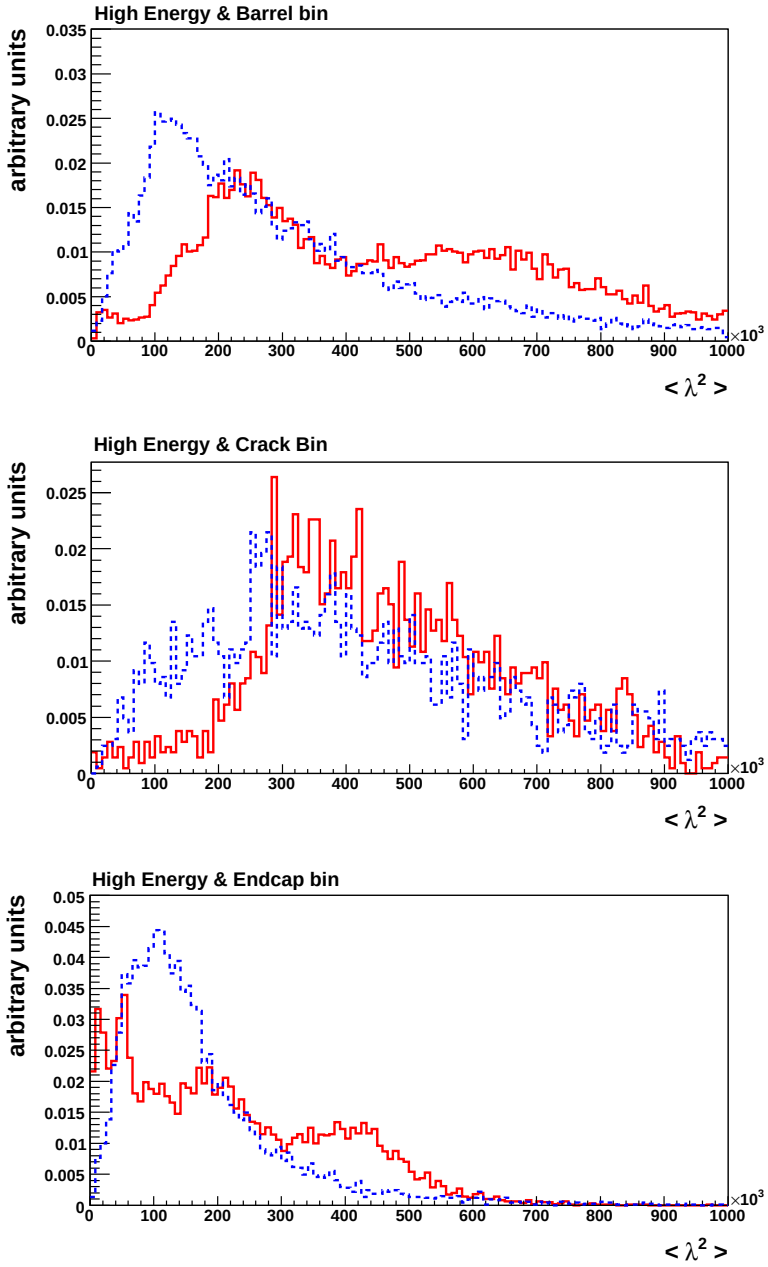

Figure 5.28. Normalized distributions of the $\langle\lambda^2\rangle$ variable for high energy single muons (solid red lines) and single pions (dashed blue lines) in barrel, crack and endcap bin.

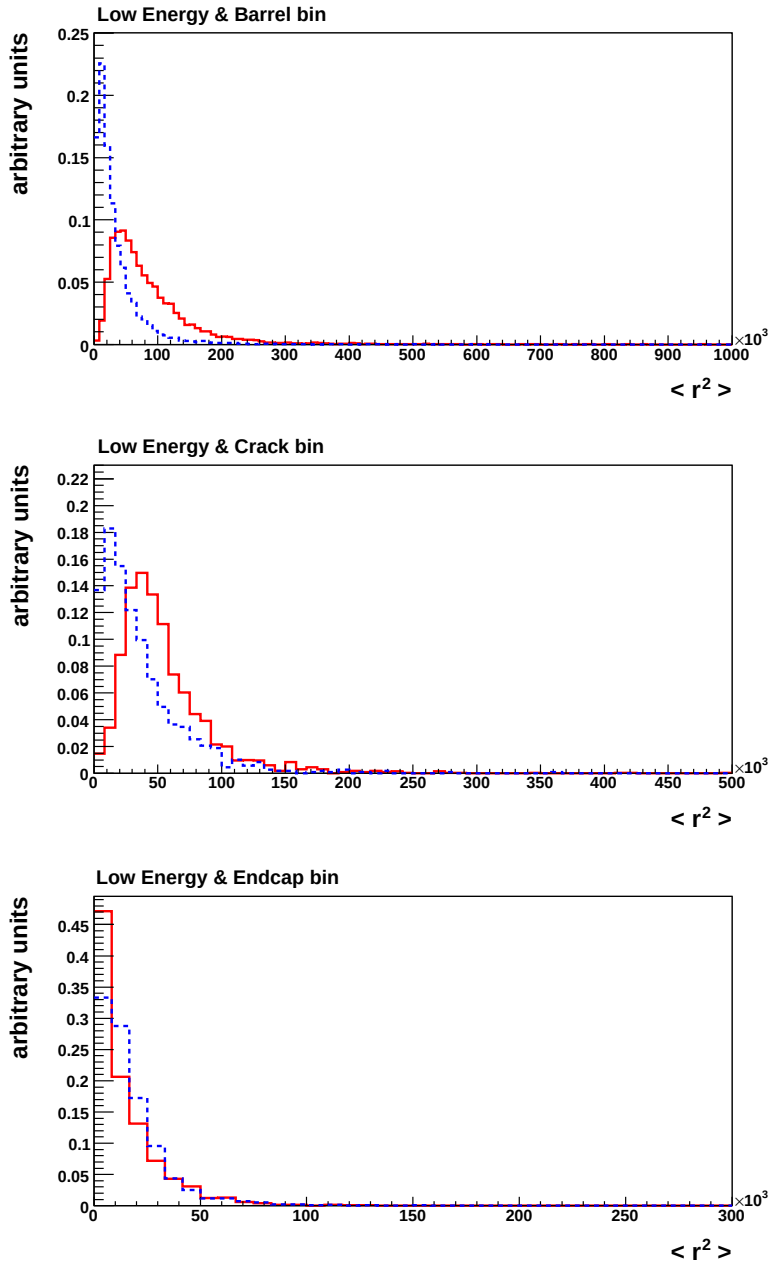

Figure 5.29. Normalized distributions of the $\langle r^2 \rangle$ variable for low energy single muons (solid red lines) and single pions (dashed blue lines) in barrel, crack and endcap bin.

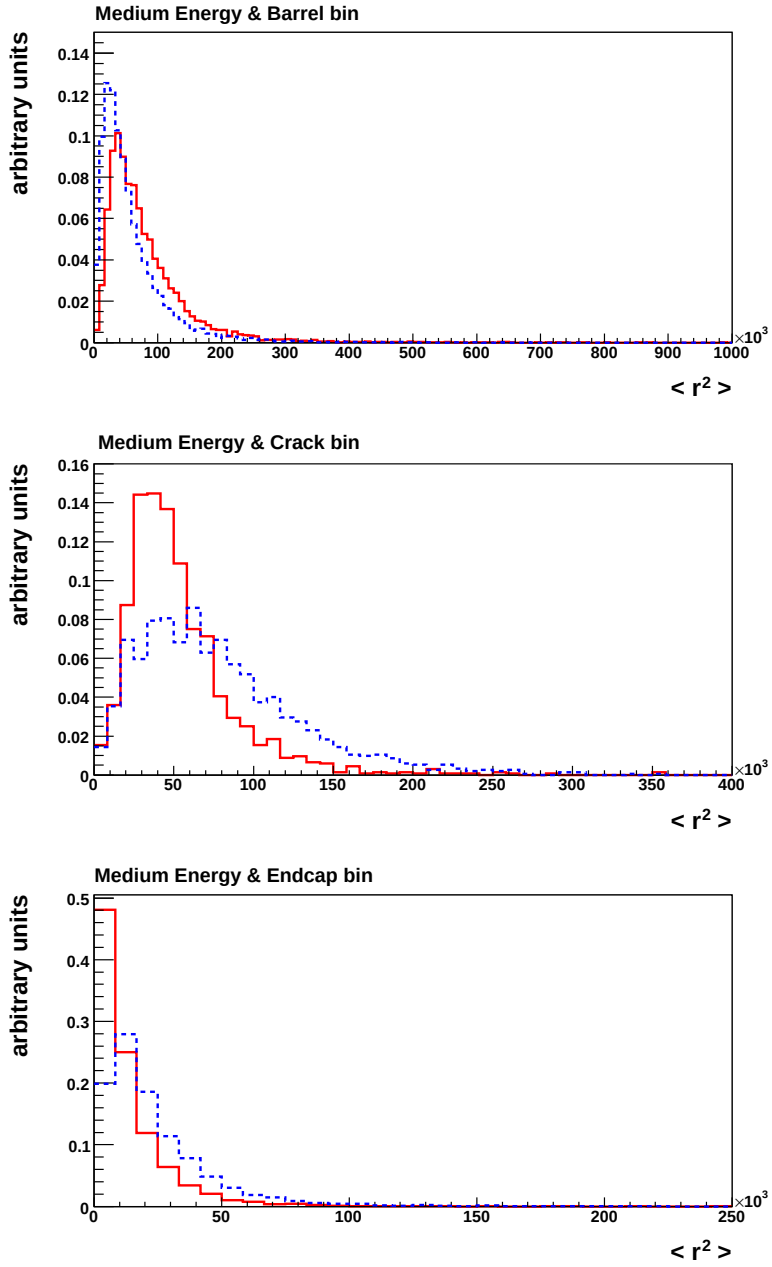

Figure 5.30. Normalized distributions of the $\langle r^2 \rangle$ variable for medium energy single muons (solid red lines) and single pions (dashed blue lines) in barrel, crack and endcap bin.

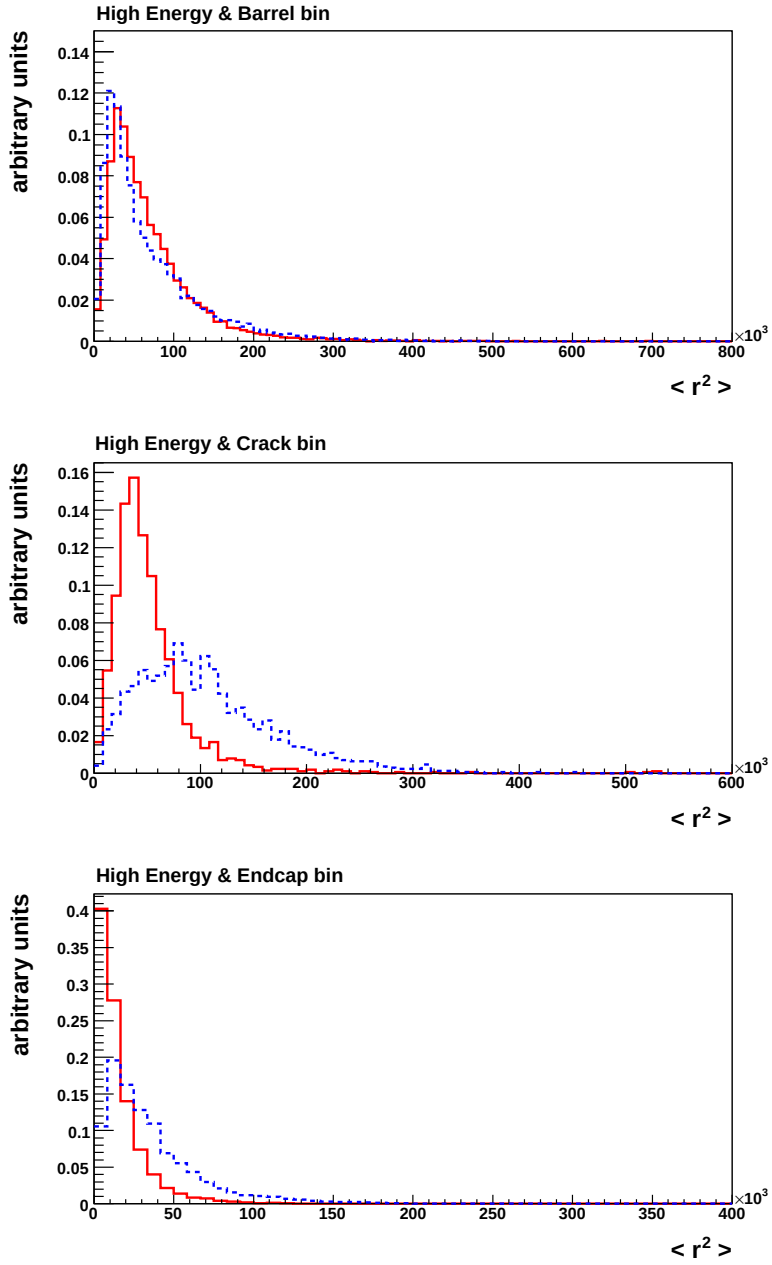

Figure 5.31. Normalized distributions of the $\langle r^2 \rangle$ variable for high energy single muons (solid red lines) and single pions (dashed blue lines) in barrel, crack and endcap bin.

6. CONCLUSIONS

Muon identification algorithms that use inner detector tracks and based on calorimeter measurements are complementary to the muon reconstruction and identification algorithms that are based on the muon spectrometer measurements. In this thesis we show that their benefits are not negligible for recovering muons with low-p_T and muons in the low-acceptance spectrometer regions (especially $|\eta| \approx 0$).

With the improvements that are presented in this thesis, the CaloLR algorithm shows a good performance and a fake rate that is within acceptable limits with the simulation data studies. Of course the algorithm needs further tuning with real data once it is available.

Application to the analysis of $H(130) \rightarrow ZZ^* \rightarrow 4\ell$ channel shows that, $CaloLR$ muons additionally used in the analysis make a noteworthy increase in the statistical significance of this channel. The gain of 17% in the number of reconstructed signal events and about a similar increase in the number of irreducible background ZZ events is observed, whereas, no increase in the number of reconstructed events for the reducible backgrounds $Zb\bar{b}$ and $t\bar{t}$ is observed due to optimized event preselection cuts. The statistical significance for a luminosity of 30 fb^{-1} has increased from 3.6 to 4.0, when $CaloLR$ muons are added to the analysis. The extra muons found by the $CaloLR$ algorithm that led to an increase in the number of events are observed to be mainly with low-p_T or coming from low-acceptance spectrometer region at $|\eta| \approx 0$, which indicate the specific advantage it brings to use $CaloLR$ algorithm.

The two strategies for calorimeter-based muon tagging are worth pursuing because one ($CaloMT$) is very simple and robust, which may be better suited for early data, while the other ($CaloLR$) needs a better understanding of shower shapes, which will most likely be in good shape for the period in which Higgs searches become feasible (after having accumulated a few fb^{-1}).

APPENDIX A: 4 SM FAMILY CASE

The number of fundamental fermion families (generations) is not fixed by the Standard Model. The flavor democracy hypothesis favors the existence of the fourth SM family [58, 59]. If it exists, the LHC will copiously produce its multi-hundreds GeV quarks, u_4 and d_4 [27, 60]. In that case, the dominant production mechanism of the Higgs boson, $gg \to H$ gluon-fusion process will get enhanced by having two additional diagrams, where the t quark is replaced by u_4 and d_4 quarks [61–64]. This enhancement will improve the signal of Higgs boson in all decay modes.

In Table A.1, the production cross sections for $H \to ZZ^{(*)} \to 4\ell$ events in the cases of three and four SM families at LHC with $\sqrt{s} = 14$ TeV are given. The enhancement is due to the increase in the cross section of the Higgs boson production via gluon-fusion, led by the fourth SM family [62–64].

The results of the analysis of $H \to ZZ^* \to 4\ell$ channel for $m_H = 130$ GeV (see Table 5.7), obtained in Section 5.6, are re-calculated for the case of 4 SM family and shown in Table A.2. Here, the enhancement in Table A.1 for signal with $m_H = 130$ GeV is considered. The existence of the fourth SM family, which provides an increase in Higgs boson production, improves the signal cross section and does not affect the background, therefore improves the significance.

Table A.1. The production cross section in fb for $H \to ZZ^{(*)} \to 4\ell$ events at LHC [62]. Enhancement is due to the increase in the cross section of Higgs boson production via gluon-fusion, led by the fourth SM family.

$m_H(GeV)$	SM-3	SM-4	Enhancement
100	0.19	1.09	5.736
110	0.64	3.48	5.437
120	1.93	10.13	5.248
130	4.55	24.74	5.437
140	6.57	38.60	5.875
150	7.16	47.77	6.671
160	3.31	26.10	7.885
170	1.61	13.10	8.136
180	3.58	29.02	8.106
190	12.80	102.82	8.032
200	14.40	114.45	7.947
220	13.30	102.70	7.721
240	12.40	93.60	7.548
260	11.10	80.85	7.283
300	9.60	64.09	6.676
350	9.88	53.42	5.406
400	8.30	36.30	4.373
450	6.04	25.26	4.182
500	4.23	17.64	4.170

Table A.2. Cross sections (in fb) after the full event selection for the signal and backgrounds, expected significance for 10 fb^{-1} and 30 fb^{-1}, and luminosity (in fb^{-1}) needed for 3σ and 5σ obtained in the analysis of $H \to ZZ^* \to 4\ell$ channel ($m_H = 130$ GeV) in Section 5.6. Here, the results are shown for 3-SM and 4-SM family cases.

		In case of 3 SM Familiy		**In case of 4 SM Familiy**	
		STACO+MuTag	+CaloLR	STACO+MuTag	+CaloLR
Cross Section (in fb)	Signal	0.280	0.328	1.522	1.783
	ZZ	0.072	0.082	0.072	0.082
	$Zb\bar{b}$	0.033	0.033	0.033	0.033
	$t\bar{t}$	< 0.04	< 0.04	< 0.04	< 0.04
Significance	10 fb $^{-1}$	2.1	2.3	7.6	8.4
	30 fb $^{-1}$	3.6	4.0	13.2	14.5
Luminosity (in fb^{-1})	3σ	20.4	16.7	1.53	1.27
	5σ	56.7	46.3	4.25	3.53

APPENDIX B: DATA SAMPLES

1. Single-muon samples at fixed momentum
   (available at /castor/cern.ch/user/m/muonprod/1206/digit.RDO/):
   (a) mc12.007206.digit_atlas-csc-100.mu_p5GeV
   (b) mc12.007211.digit_atlas-csc-100.mu_p10GeV
   (c) mc12.007233.digit_atlas-csc-100.mu_p100GeV
   (d) mc12.007268.digit_atlas-csc-100.mu_p1000GeV
2. Physics samples
   (available at /castor/cern.ch/user/b/becerici/MCdatafiles/):
   (a) pile1sf05_misal1_csc11.005300.PythiaH130zz4l.digit.RDO.v12000605
   (b) pile1sf05_misal1_csc11.005980.Pythiazz4l.digit.RDO.v12000605
   (c) pile1sf05_misal1_mc12.005177.AcerMC_Zbb_4l.digit.RDO.v12000605
   (d) pile1sf05_misal1_mc12.005200.T1_McAtNlo_Jimmy.digit.RDO.v12000605
3. Single muon and single pion samples with energies ranging from 1 - 500 GeV availabe at:
   (a) /castor/cern.ch/user/b/becerici/Nesli_forCaloLR_MC_SingleMuonAndPion_rdo/SingleMuon_14.2.10
   (b) /castor/cern.ch/user/b/becerici/Nesli_forCaloLR_MC_SingleMuonAndPion_rdo/SinglePion_14.2.10

APPENDIX C: PREVIOUS PERFORMANCE OF *CaloLR* AND *CaloMT*

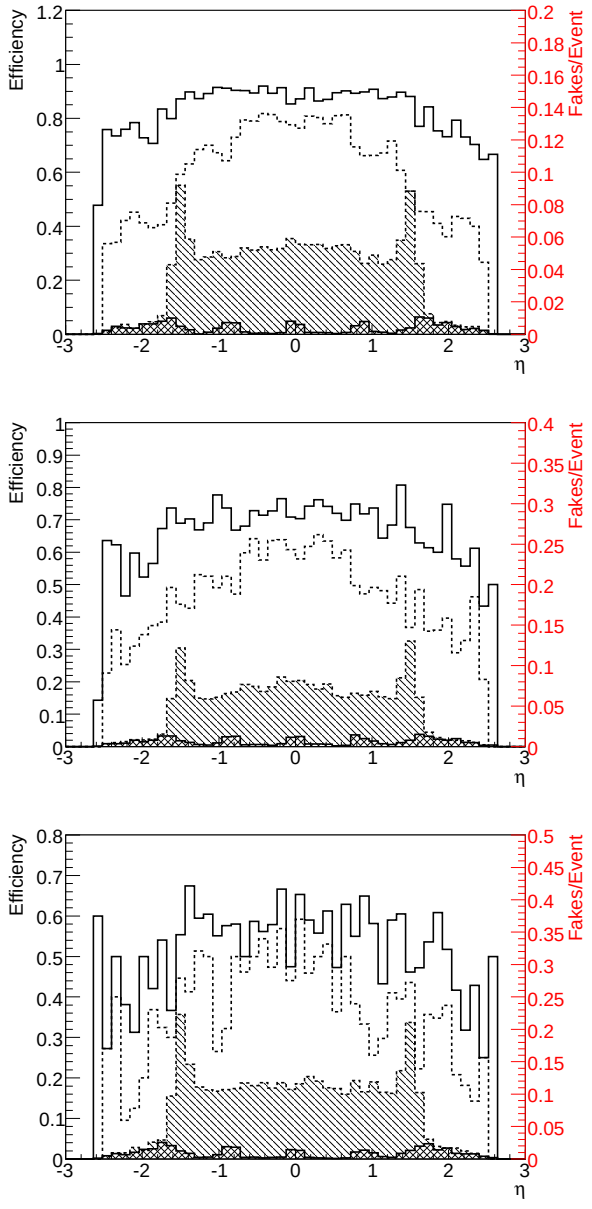

Figure C.1. Efficiency and fake rate vs η for $H(130) \rightarrow ZZ^* \rightarrow 4\ell$, $Zb\bar{b} \rightarrow 4\ell$ and $t\bar{t} \rightarrow 4\ell$ from top to bottom. Right vertical axis in red shows the fake rate (represented by shaded histograms) and left vertical axis shows the efficiency. Solid line: *CaloMT*, dashed line: *CaloLR*.

REFERENCES

1. Anderson, C. D., "The Positive Electron", *Physical Review*, Vol. 43, pp. 491-494, 1933.

2. Anderson, C. D. and S. H. Neddermeyer, "Note on the Nature of Cosmic-Ray Particles", *Physical Review*, Vol. 51, pp. 884-886, 1937.

3. Dirac, P. A. M., "The Quantum Theory of the Electron", *Proceedings of the Royal Society of London*, Series A, Vol. 117, pp. 610-624, 1928; Part II, Vol. 118, pp. 351-361, 1928.

4. Lattes, C. M. G., G. P. S. Occhialini and C. F. Powell, "Observations on the Tracks of Slow Mesons in Photographic Emulsions", *Nature*, Vol. 160, pp. 453-456 and 486-492, 1947.

5. Yukawa, H., "On the Interaction of Elementary Particles I", *Proceedings of the Physical - Mathematical Society of Japan*, Vol. 17, pp. 48-57, 1935.

6. Greenberg, O. W., "Quarks: Resource Letter Q-1", *American Journal of Physics*, Vol. 50, pp. 1074-1089, 1982.

7. Lichtenberg, D. B. and S. P. Rosen, *Developments in the Quark Theory of Hadrons*, Nonantum: Hadronic Press, 1980.

8. Gell-Mann, M. and Y. Ne'eman, *The Eightfold Way*, New York: W. A. Benjamin, 1964.

9. Amsler, C. et al., "Review of Particle Physics", *Physics Letters B*, Vol. 667, http://pdg.web.cern.ch/pdg/2008/listings/contents_listings.html, 2008.

10. Schott, M., *Study of the Z Boson Production at the ATLAS Experiment with First Data*, Ph.D. Thesis, Ludwig-Maximilians University, 2007.

11. Feynman, R. P., "Mathematical Formulation of the Quantum Theory of Electromagnetic Interaction", *Physical Review Letters*, Vol. 80, pp. 440-457, 1950.

12. Glashow, S. L., "Partial Symmetries of Weak Interactions", *Nuclear Physics*, Vol. 22, pp. 579-588, 1961.

13. Weinberg, S., "A Model of Leptons", *Physical Review Letters*, Vol. 19, pp. 1264-1266, 1967.

14. Salam, A., "Weak and Electromagnetic Interactions", *Proceedings Of The Nobel Symposium Held 1968 At Lerum*, Sweden, Stockholm, pp. 367-377, 1968.

15. Higgs, P. W., "Broken Symmetries, Massless Particles and Gauge Fields", *Physical Review Letters*, Vol. 12, pp. 132-133, 1964.

16. Higgs, P. W., "Broken Symmetries and the Masses of Gauge Bosons", *Physical Review Letters*, Vol. 13, pp. 508-509, 1964.

17. Englert, F. and R. Brout, "Broken Symmetry and the Mass of Gauge Vector Mesons", *Physical Review Letters*, Vol. 13, pp. 321-323, 1964.

18. Dawson, S., *Introduction to the Physics of Higgs Boson*, Brookhaven National Laboratory, BNL-61012, October 1994.

19. Barate, R. et al., "Search for the Standard Model Higgs Boson at LEP", *Physics Letters B*, Vol. 565, pp. 61-75, 2003.

20. *The LEP Electroweak Working Group*, http://lepewwg.web.cern.ch/LEPEWWG/.

21. Bolognesi S., G. Bozzi and A. Di Simone, "Higgs at LHC", *Nuovo Cimento B*, Vol. 123, pp. 499-508, 2008.

22. *First Beam and First Events in ATLAS*, http://www.atlas.ch/news/2008/first-beam-and-event.html, 10 September 2008.

23. *Follow up of the Incident of 19 September 2008 at the LHC*, https://edms.cern.ch/file/973073/1/Report_on_080919_incident_at_LHC__2_.pdf, 2008.

24. Brning, O.S. et al., "The LHC Main Ring", *The LHC Design Report*, Vol. 1, CERN-2004-003-V-1, 2004; "The LHC Infrastructure and General Services", *The LHC Design Report*, Vol. 2, CERN-2004-003-V-2, 2004; Benedikt, M. et al., "The LHC Injector Chain", *The LHC Design Report*, Vol. 3, CERN-2004-003-V-3, 2004.

25. Evans, L. and P. Bryant, "LHC Machine", *Journal of Instrumentation*, Vol. 3, S08001, 2008.

26. The ATLAS Collaboration, *ATLAS : Technical Proposal for a General-Purpose pp Experiment at the Large Hadron Collider at CERN*, CERN-LHCC-94-43, 1994.

27. The ATLAS Collaboration, *ATLAS Detector and Physics Performance : Technical Design Report*, Vol. 1, CERN-LHCC-99-014, 1999; Vol. 2, CERN-LHCC-99-015, 1999.

28. The ATLAS Collaboration, "The ATLAS Experiment at the CERN Large Hadron Collider", *Journal of Instrumentation*, Vol. 3, S08003, 2008.

29. The CMS Collaboration, "The CMS Experiment at the CERN LHC", *Journal of Instrumentation*, Vol. 3, S08004, 2008.

30. The LHCb Collaboration, "The LHCb Detector at the LHC", *Journal of Instrumentation*, Vol. 3, S08005, 2008.

31. The TOTEM Collaboration, "The TOTEM Experiment at the CERN Large Hadron Collider", *Journal of Instrumentation*, Vol. 3, S08007, 2008.

32. The ALICE Collaboration, "The ALICE Experiment at the CERN LHC", *Journal of Instrumentation*, Vol. 3, S08002, 2008.

33. The ATLAS Collaboration, *ATLAS Inner Detector : Technical Design Report*, Vol. 1, CERN-LHCC-97-16, 1997; Vol. 2, CERN-LHCC-97-17, 1997.

34. The ATLAS Collaboration, *ATLAS Magnet System : Technical Design Report*, CERN-LHCC-97-018, 1997.

35. Cwetanski, P., *Straw Performance Studies and Quality Assurance for the ATLAS Transition Radiation Tracker*, Ph.D. Thesis, University of Helsinki, 2006.

36. The ATLAS Collaboration, *ATLAS Liquid-Argon Calorimeter : Technical Design Report*, CERN-LHCC-96-041, 1996.

37. The ATLAS Collaboration, *ATLAS Tile Calorimeter : Technical Design Report*, CERN-LHCC-96-042, 1996.

38. Artamonov, A. et al., "The ATLAS Forward Calorimeter", *Journal of Instrumentation*, Vol. 3, P02010, 2008.

39. Aubert, B. et al., "Development and Construction of Large Size Signal Electrodes for the ATLAS Electromagnetic Calorimeter", *Nuclear Instruments and Methods in Physics Research A*, Vol. 539, pp. 558-594, 2005.

40. Speckmayer, P., *Energy Measurement of Hadrons with the CERN ATLAS Calorimeter*, Ph.D. Thesis, Vienna University of Technology, 2008.

41. The ATLAS Collaboration, *ATLAS Muon Spectrometer : Technical Design Report*, CERN-LHCC-97-022, 1997.

42. The ATLAS Collaboration, *ATLAS Barrel Toroid : Technical Design Report*, CERN-LHCC-97-019, 1997.

43. The ATLAS Collaboration, *ATLAS End-cap Toroid : Technical Design Report*, CERN-LHCC-97-020, 1997.

44. The ATLAS Collaboration, *ATLAS High-Level Trigger, Data Acquisition and Controls : Technical Design Report*, CERN-LHCC-2003-022, 2003.

45. The ATLAS Collaboration, *ATLAS Computing : Technical Design Report*, CERN-LHCC-2005-022, 2005.

46. The GEANT4 Collaboration, "GEANT4 : A Simulation Toolkit", *Nuclear Instruments and Methods in Physics Research A*, Vol. 506, pp. 250-303, 2003.

47. Bird, I. et al., *LHC Computing Grid : Technical Design Report*, CERN-LHCC-2005-024, 2005.

48. The ATLAS Collaboration, *Expected Performance of the ATLAS Experiment, Detector, Trigger and Physics*, CERN-OPEN-2008-020, 2008.

49. Hassani, S. et al., "A Muon Identification and Combined Reconstruction Procedure for the ATLAS Detector at the LHC Using the (Muonboy, STACO, Mutag) Reconstruction Packages", *Nuclear Instruments and Methods in Physics Research A*, Vol. 572, pp. 77-79, 2007.

50. Lagouri, T. et al., "A Muon Identification and Combined Reconstruction Procedure for the ATLAS Detector at the LHC at CERN", *IEEE Nuclear Science Symposium Conference Record*, Vol. 3, pp. 1545-1548, 19-25 October 2003.

51. Tarem, S., Z. Tarem, N. Panikashvili and O. Belkind, "MuGirl - Muon Identification in ATLAS from the inside out", *IEEE Nuclear Science Symposium Conference Record*, Vol. 1, pp. 617-621, 2007.

52. Nikolopoulos, K. et al., *Muon Energy Loss Upstream of the Muon Spectrometer*, ATL-MUON-PUB-2007-002; ATL-COM-MUON-2006-019, 2006.

53. Usai, G., "Trigger of Low-p_T Muons with the ATLAS Hadronic Calorimeter", *Nuclear Instruments and Methods in Physics Research*, Vol. 518, pp. 36-38, 2004.

54. The ATLAS Collaboration, *Performance of the ATLAS Muon Trigger Slice with Simulated Data*, ATLAS Note, ATL-PHYS-PUB-2006-000, 2008.

55. Friedman, J., "353QH Twice Smoothing Algorithm", *Proceedings of the CERN School of Computing*, Norway, 11-24 August 1974.

56. Assamagan, K. A. et al., *Muons in the ATLAS Calorimeters: Energy Loss Corrections and Muon Tagging*, ATLAS CSC Note, 2008.

57. *Cluster Moments*, https://twiki.cern.ch/twiki/bin/view/Atlas/ClusterMoments.

58. Sultansoy, S., "Why the Four SM Families", *High Energy Physics - Phenomenology*, hep-ph/0004271, 2000.

59. Sultansoy, S., "Flavor Democracy in Particle Physics", *AIP Conference Proceedings*, Vol. 899, pp. 49-52, hep-ph/0610279v1, 2007.

60. Arik, E. et al., "Search for the fourth family up quarks at CERN LHC", *Physical Review D*, Vol. 58, 117701, 1998.

61. Cakir, O. and S. Sultansoy, "The Fourth SM Family Enhancement to the Golden Mode at the Upgraded Tevatron", *Physical Review D*, Vol. 65, 013009, 2002; Arik, E. et al., "Observability of the Higgs Boson in the presence of Extra SM Families at the Tevatron", *Acta Physica Polonica B*, Vol. 37, No. 10, page 2839, 2006.

62. Arik, E., O. Cakir, S. A. Cetin and S. Sultansoy, "Consequences of the Extra SM Families on the Higgs Boson Production at the Tevatron and LHC", *Physical Review D*, Vol. 66, 033003, 2002.

63. Arik, E. et al., "Enhancement of the Standard Model Higgs Boson Production Cross-Section with the Fourth Standard Model Family Quarks", *ATLAS Internal Note*, ATL-PHYS-98-125, 1998.

64. Arik, E. et al., "With four Standard Model families, the LHC could discover the Higgs boson with a few fb^{-1}", *European Physical Journal C*, Vol. 26, Issue 1, pp. 9-11, 2002.